

**EVALUATION OF RARE-EARTH ELEMENT DOPANTS (SM AND ER)  
EFFECT ON THE ABLATION RESISTANCE AND EMITTANCE  
TAILORING OF ZRB<sub>2</sub>/SIC SINTERED BILLETS**

by

**Angel Antonio Peña**

**A Dissertation**

*Submitted to the Faculty of Purdue University*

*In Partial Fulfillment of the Requirements for the degree of*

Doctor of Philosophy



Materials Engineering, Purdue University

West Lafayette, Indiana

May 2019

**THE PURDUE UNIVERSITY GRADUATE SCHOOL**  
**STATEMENT OF COMMITTEE APPROVAL**

Dr. Rodney W. Trice, Chair

Department of Materials Science and Engineering

Dr. Kevin Trumble

Department of Materials Science and Engineering

Dr. John Blendell

Department of Materials Science and Engineering

Dr. David Johnson

Department of Materials Science and Engineering

**Approved by:**

Dr. David Bahr

Head of the Graduate Program

To mom, dad, Angélica, Alejandra and Vanessa

## ACKNOWLEDGMENTS

I gratefully acknowledge the financial support of Dr. Ali Sayir of the Air Force Office of Scientific Research (AFOSR Grant # FA9550-16-1-0039) for the study of high emittance ceramics for hypersonic applications. I would like to thank to my advisor, Prof. Rodney Trice for guiding and trusting in my capacity which helped me to achieve all my accomplishments during the last four years. Prof. Trice has been one of the most important persons in my development as an engineer, providing me the necessary tools to be successful in my professional career. I would also like to give thanks to my dissertation committee: Prof. Kevin Trumble, Prof. Elliott Slamovich, Prof. David Johnson and Prof. John Blendell for their time, advices, and knowledge.

Also, I would like to thank Dr. Jonathan Vernon, Dr. Jeremy Pitz and Dr. Eric Moro of the Air Force Research Lab for the help they provided during the emittance testing at the RHINO Lab and their general advices through these four years. In addition, I would like to thank Dr. Christopher Petorak and Brian Thompson of Praxair Surface Technology for the help they provided in preparing thermal spray coatings.

I am grateful for the Materials Science and Engineering professors and staff for treating me as far more than just a student, but also a family member. Also, I would like to thank for all the support of my research group colleagues, specially to Annelise Brenner, Jorge Ramirez, Willie Costakis and Andrew Schlup.

Also, I want to acknowledge Anneliese E. Brenner for providing the SEM electron micrograph of the undoped spray-dried  $\text{ZrB}_2$ -20 vol% SiC particles showed in the Figure 9. Thanks also to Andrew P. Schlup for helping with the sintering process.

## TABLE OF CONTENTS

LIST OF TABLES .....	7
LIST OF FIGURES .....	8
EXTRA HEADINGS .....	10
ABSTRACT .....	12
1. INTRODUCTION AND BACKGROUND .....	14
1.1 Importance of Ultra-High Temperature Ceramics (UHTC) Studies .....	14
1.2 Approach to Produce a Tailorable Emittance System .....	15
1.3 Factors That Affect the UHTC During Ablation .....	17
1.3.1 Oxyacetylene Ablation Rig .....	17
1.3.2 Oxidation Effect During Ablation .....	20
1.4 Ablation Process of UHTC .....	22
2. EXPERIMENTAL PROCEDURES .....	27
2.1 Materials and Powder Preparation .....	27
2.2 Oxyacetylene Ablation Testing .....	29
2.3 Microstructural and Phase Analysis .....	30
2.4 Laser Heating Testing .....	31
3. EVALUATION OF RARE-EARTH ELEMENT DOPANTS (SAMARIUM AND ERBIUM) ON THE ABLATION RESISTANCE OF ZIRCONIUM DIBORIDE/SILICON CARBIDE SINTERED BILLETS .....	32
3.1 Results .....	32
3.1.1 Pre-ablated Sintered Samples Results .....	32
3.1.2 Ablation Results After 60s .....	37
3.1.3 Ablation Results After 300 s .....	42
3.2 Discussion .....	47
3.2.1 First observation: The beneficial samarium/erbium zirconium oxide scale noted after ablation for 60 s and 300 s is formed by a convection cells mechanism .....	47
3.2.2 Second observation: Changes in the surface Sm and Er dopant concentration affects surface temperature measured .....	52
3.3 Conclusions .....	54

4. EVALUATION OF RARE-EARTH ELEMENT DOPANTS (SAMARIUM AND ERBIUM) ON THE EMITTANCE TAILORING OF ZIRCONIUM DIBORIDE/SILICON CARBIDE SINTERED BILLETS.....	55
4.1 Data Conversion Process: Spectral Radiance to Emittance .....	55
4.2 Results.....	59
4.2.1 Microstructural and Phase Analysis Results after Laser Heating.....	59
4.2.2 Emittance Profiles after Laser Heating .....	67
4.3 Discussion .....	84
4.3.1 Factors Influencing the Emittance .....	84
4.3.2 Sm and Er Dopant Concentration Effect on the Emittance of ZBS Systems .....	85
4.3.3 Temperature and Wavelength Effect on the Emittance of ZBS Systems .....	88
4.4 Conclusions.....	90
5. BENEFICIAL CUBIC SAMARIUM/ERBIUM ZIRCONIUM OXIDE SCALE DEVELOPMENT .....	92
5.1 Beneficial $c_1\text{-(Sm/Er)}_{0.2}\text{Zr}_{0.9}\text{O}_{1.8}$ Scale Preparation Using an Oxygen Furnace .....	92
APPENDIX A: POWDER CALCULATION FOR CHEMICAL DOPANT CONCENTRATION .....	95
APPENDIX B: MATLAB ALGORITHM TO CONVERT SPECTRAL RADIANCE TO EMITTANCE .....	100
REFERENCES .....	114
VITA.....	119
PUBLICATIONS.....	120

## LIST OF TABLES

<b>Table 1</b> Samarium and erbium dopant concentration and properties after sintering.....	33
---	----

## LIST OF FIGURES

Figure 1. Emittance versus wavelength profiles for $\text{Sm}_2\text{O}_3$ .....	16
Figure 2. Emittance versus wavelength profiles for $\text{Er}_2\text{O}_3$ .....	16
Figure 3. Flame length variation with the VFR ratio.....	19
Figure 4. Position effect on local heat flux and partial oxygen pressure.....	20
Figure 5. Partial oxygen pressure and heat flux effect on the oxidation rate.....	21
Figure 6. ZBS dense oxide scale after ablation up to 1500 °C .....	24
Figure 7. Emittance results for different UHTCs at 1727°C for different factors .....	25
Figure 8. ZBS samarium doped coating cross section microstructure.....	26
Figure 9. SEM micrograph of undoped spray dried 80 vol.% $\text{ZrB}_2$ - 20 vol% SiC particles showing the particle size of the granules .....	27
Figure 10. X-ray diffraction patterns of the surface of the pre-ablated sintered samples.....	35
Figure 11. SEM micrographs of the surface of the pre-ablated sintered billets for: a) 1Sm:0Er, b) 2Sm:1Er, c) 1Sm:1Er, d) 1Sm:2Er, and e) 0Sm:1Er .....	36
Figure 12. Front surface temperature during ablation testing for 60 s.....	38
Figure 13. Optical images of the ablated billets: a) 1Sm:0Er, b) 2Sm:1Er, c) 1Sm:1Er, d) 1Sm:2Er, and e) 0Sm:1Er after 60 s, and f) 1Sm:0Er, g) 2Sm:1Er, h) 1Sm:1Er, i) 1Sm:2Er, and j) 0Sm:1Er after 300 s .....	39
Figure 14. SEM micrographs of the following billets: a) 1Sm:0Er, b) 2Sm:1Er, c) 1Sm:1Er, d) 1Sm:2Er, and e) 0Sm:1Er after 60 s, and f) 1Sm:0Er, g) 2Sm:1Er, h) 1Sm:1Er, i) 1Sm:2Er, and j) 0Sm:1Er after 300 s .....	41
Figure 15. X-ray diffraction patterns of the surface after 60 s.....	42
Figure 16. Front surface temperature during ablation testing for 300 s.....	43
Figure 17. X-ray diffraction patterns of the surface after 300 s ablation cycle .....	45
Figure 18. EDS line-scan for the 2Sm:1Er sample after 300 s ablation cycle and the wt.% concentration of major elements across the ablated billet thickness .....	46
Figure 19. SEM-EDS for: a) micrograph of the flower-like microstructure on the 1Sm:0Er billet after the 60 s ablation cycle, b) micrograph of the 0Sm:1Er billet after the 60 s ablation cycle..	49
Figure 20. Blackbody calibration at the four chosen temperatures of interest using the Planckian form of the Sakuma-Hattori equation. ....	57
Figure 21. Coefficients B and C versus wavelength from 1500-5000 nm.....	58



Figure 22. Optical images of the back-side of the billets (laser-side) for the following billets: a) 1Sm:0Er, b) 2Sm:1Er, c) 1Sm:1Er, d) 1Sm:2Er, and e) 0Sm:1Er at 700 Watts; f) 1Sm:0Er, g) 2Sm:1Er, h) 1Sm:1Er, i) 1Sm:2Er, and j) 0Sm:1Er at 800 Watts; and k) 1Sm:0Er, l) 2Sm:1Er, m) 1Sm:1Er, n) 1Sm:2Er, and o) 0Sm:1Er at 900 Watts ..... 60

Figure 23. Optical images of the front side of the billets (spectrometer-side where the data was collected) for the following billets: a) 1Sm:0Er, b) 2Sm:1Er, c) 1Sm:1Er, d) 1Sm:2Er, and e) 0Sm:1Er at 700 Watts; f) 1Sm:0Er, g) 2Sm:1Er, h) 1Sm:1Er, i) 1Sm:2Er, and j) 0Sm:1Er at 800 Watts; and k) 1Sm:0Er, l) 2Sm:1Er, m) 1Sm:1Er, n) 1Sm:2Er, and o) 0Sm:1Er at 900 Watts ... 61

Figure 24. XRD patterns of the surface on the spectrometer side ..... 62

Figure 25. SEM micrographs after the laser heating for 120 s for the following billets: a) 1Sm:0Er, b) 2Sm:1Er, c) 1Sm:1Er, d) 1Sm:2Er, and e) 0Sm:1Er at 700 W; f) 1Sm:0Er, g) 2Sm:1Er, h) 1Sm:1Er, i) 1Sm:2Er, and j) 0Sm:1Er at 800 W; and k) 1Sm:0Er, l) 2Sm:1Er, m) 1Sm:1Er, n) 1Sm:2Er, and o) 0Sm:1Er at 900 W ..... 64

Figure 26. EDS line-scan after 80 s of laser heating at 800 Watts for the following billets: (a) 2Sm:1Er, (b) 1Sm:1Er, and (c) 0Sm:1Er ..... 66

Figure 27. Temperature versus time comparison for the five different Sm:Er ratios tested at 800 W for 80 s ..... 68

Figure 28. Emittance versus wavelength profiles at 1600 °C, 1700 °C and 1800 °C, 1900 °C, 2000 °C, and 2100 °C from 1500-3000 nm for the following billets: (a) 1Sm:0Er, and (b) 0Sm:1Er ..... 70

Figure 29. Emittance versus wavelength profiles at 1600 °C, 1700 °C and 1800 °C, 1900 °C, 2000 °C, and 2100 °C from 1500-3000 nm for the following billets: a) 2Sm:1Er, b) 1Sm:1Er, and c) 1Sm:2Er ..... 73

Figure 30. Emittance versus wavelength profiles at 1600 °C, 1700 °C and 1800 °C, 1900 °C, 2000 °C and 2100 °C from 3000-4500 nm for the following billets: (a) 1Sm:0Er, and (b) 0Sm:1Er ..... 74

Figure 31. Emittance versus wavelength profiles at 1600 °C, 1700 °C and 1800 °C, 1900 °C, 2000 °C, 2100 °C and 2200 °C from 3000-4500 nm for the following billets: a) 2Sm:1Er, b) 1Sm:1Er, and c) 1Sm:2Er ..... 77

Figure 32. Emittance versus laser heating time profiles as a function of wavelength for the following billets: a) 1Sm:0Er, b) 2Sm:1Er, and c) 1Sm:1Er, d) 1Sm:2Er, and e) 0Sm:1Er ..... 78

Figure 33. Emittance versus wavelength profiles as a function of dopant molar ratios at the following temperatures: (a) 1600 °C, (b) 1700 °C, (c) 1800 °C, (d) 1900 °C, (e) 2000 °C, (f) 2100 °C, and (g) 2200 °C ..... 80

Figure 34 Emittance difference from 1500-4500 nm for the 2Sm:1Er, 1Sm:1Er, 1Sm:2Er, and 0Sm:1Er samples in comparison with the 1Sm:0Er sample ..... 82

Figure 35. XRD patterns of the surface after the preparation in the oxygen furnace for the 2Sm:1Er, 1Sm:1Er, and 1Sm:2Er samples ..... 93

Figure 36. Optical images of the surface after the preparation in the oxygen furnace for the 2Sm:1Er, 1Sm:1Er, and 1Sm:2Er samples. .... 94

Figure 37. SEM micrographs of the surface after the preparation in the oxygen furnace for the 2Sm:1Er, 1Sm:1Er, and 1Sm:2Er samples ..... 94

## NOMENCLATURE

### Acronyms

HEC	high emittance ceramics
UHTC	ultra-high temperature ceramics
VFR	volumetric flow rate
ZBS	ZrB <sub>2</sub> -SiC

### Variables

$\varepsilon$	emittance	$t_i$	thickness before ablation
$T_s$	surface temperature	$t_f$	thickness after ablation
$q_{\text{chem}}$	chemical heating	$R_m$	mass ablation rate
$q_{\text{conv}}$	convection heating	$m_i$	sample weight before ablation
$\sigma$	Stefan-Boltzmann constant	$m_f$	sample weight after ablation
$T_f$	front face temperature	$J_{\text{O}_2}$	flux of oxygen
$T_b$	back face temperature	$p_{\text{O}_2}$	partial oxygen pressure
$L_\lambda$	spectral radiance	$D$	diffusion coefficient
$\lambda$	wavelength	$R$	gas constant
$h$	Planck constant	$\mu$	viscosity of air
$k$	Boltzmann constant	$l$	sample length
$c_o$	speed of the light in vacuum	$\rho$	density
$T_{\text{blackbody}}$	temperature of the blackbody	$V$	velocity of the specimen
$Q_{\text{in}}$	initial heat transfer	$\&$	drag coefficient
$q_{\text{conduction, c}}$	pure conduction		
$q_{\text{flame}}$	heat flux of the flame		
$q_{\text{radiation}}$	radiation heat transfer		
$q_{\text{convection}}$	convection heat transfer		
$R_l$	linear ablation rate		

## ABSTRACT

Author: Pena, Angel, A. PhD

Institution: Purdue University

Degree Received: May 2019

Title: Evaluation of Rare-Earth Element Dopants (Sm and Er) Effect on the Ablation Resistance and Emittance Tailoring of ZrB<sub>2</sub>/SiC Sintered Billets

Committee Chair: Rodney Trice

Hypersonic flight causes ultra-high surface temperatures which are most intense on sharp leading edges. One way of reducing the surface temperature is to apply a high emittance ceramic (HEC) on the leading edge, increasing the radiation component of heat transfer. An ideal HEC must have a high emittance, while also possessing a strong ablation resistance. From a scientific standpoint, it would be helpful if emittance could be tailored at different wavelengths. For example, materials with tailorable emittance could be used to improve the efficiency of engines, thermophotovoltaic cells, and other applications. The approach used to create a ceramic with tailorable emittance was to use two different rare-earth elements, adding them to an ultra-high temperature ceramic (UHTC) in small quantities. The samarium element was added to increase the emittance of the UHTC over a large wavelength range (visible to near infrared wavelengths, consistent with the temperature range expected for hypersonic flight), and the erbium element was added to decrease the emittance at specific wavelength ranges. The goal of this study was to create an UHTC with tailorable emittance while maintaining the required ablation resistance. Therefore, ZrB<sub>2</sub>/SiC billets with five different Sm to Er ratios and with a nominal total amount of 3 mol.% dopant incorporated were prepared by sintering in vacuum to 2000 °C. The ablation resistance was evaluated by using an oxyacetylene torch and observing at exposure times of 60 s and 300 s, whereas the emittance was evaluated at the Air Force Research Lab facilities via a laser heating testing. The results for

the ablation testing showed that ZrB<sub>2</sub>-SiC (ZBS) billets co-doped with Sm and Er formed a beneficial  $c1-(\text{Sm/Er})_{0.2}\text{Zr}_{0.8}\text{O}_{1.9}$  oxide scale as the majority phase, which is more thermally stable than the  $m\text{-ZrO}_2$  oxide scale typically formed in oxidized ZBS systems, resulting in a more adherent oxide scale to the unreacted material. The crystalline oxide scale and the amorphous phase were formed by a convection cell mechanism where the  $c1-(\text{Sm/Er})_{0.2}\text{Zr}_{0.8}\text{O}_{1.9}$  crystalline islands precipitate, grow, and coalesce. Moreover, differences in surface temperatures between ZBS samples with different dopant ratios suggest differences in spectral absorptance/emittance between each of the five compositions evaluated. Despite that the emittance profiles with varying Sm:Er molar ratios were similar because  $m\text{-ZrO}_2$  was formed as the major oxide phase, the emittance study showed that the erbium oxide influences the emittance profile, as can be noted by the maximum and minimum emittance peaks. Furthermore, results showed that the emittance varies as a function of dopant(s) molar ratios and temperature at shorter wavelength ranges. These changes in the emittance are caused by the different Sm and Er concentration on the surface. Future work should be focused on producing the beneficial  $c1-(\text{Sm/Er})_{0.2}\text{Zr}_{0.9}\text{O}_{1.8}$  phase directly from the manufacturing process, and therefore, maximize the effect of varying the Sm:Er molar ratios to tailor the emittance. Nonetheless, this study represents the first generation and reported emittance data of UHTC doping ZBS systems with both Sm and Er elements.

# 1. INTRODUCTION AND BACKGROUND

## 1.1 Importance of Ultra-High Temperature Ceramics (UHTC) Studies

Hypersonic vehicle design involves the use of sharp leading edges to improve performance and reduce aerodynamic drag.<sup>1,2</sup> During hypersonic flights, a substantial amount of energy is transferred to the vehicle leading edge by convection and chemical heating.<sup>1,3</sup> Convective heating, caused by the high enthalpy bow shock layer, can result in strong thermal shock on the vehicle's sharp leading edges.<sup>1</sup> The atmospheric friction during the reentry process causes the diatoms in the air, such as O<sub>2</sub> molecules, to separate into ions which, in turn, recombine on the hot surface to release energy that results in chemical heating.<sup>4</sup> Both processes can heat the leading edge greater than or equal to 2000 °C.

Among the UHTC being considered for leading edges, studies have shown that ZrB<sub>2</sub>-SiC (ZBS) is a promising material for hypersonic applications due to its high melting point and strength at 1500°C and above, as well as its ablation and thermal shock resistance.<sup>3-6</sup> Despite all of these benefits, ZBS becomes less effective at temperatures above 1600 °C due to the evaporation of the protective glassy oxide layers formed by oxidation of the SiC.<sup>4,7,8</sup> Because of this, finding a means to reduce the surface temperature during hypersonic flight is an urgent issue. Leading edge surface temperatures can be reduced by two ways: increasing the conduction heat transfer and increasing the radiation heat transfer. An UHTC with a high thermal conductivity is beneficial because it reduces the thermal gradient and the undesirable effects of local hot spots.<sup>4</sup> An UHTC can also reduce surface temperature via radiation.<sup>1,4</sup> The relevant material property is emittance, with a value approaching that of a desired black body. Studies performed by Tan et al.<sup>3,4,9</sup> have shown that adding Sm dopant to ZBS increases its emittance compared to ceramics comprised of only ZBS. Specifically, a total emittance of 0.9 at 1600 °C was measured for a coating with 5 mol.%

Sm dopant and a balance of  $\text{ZrB}_2/\text{SiC}$ .<sup>9</sup> Furthermore, the Sm dopant improved ablation performance by forming a stable oxide scale of  $\text{c}_1\text{-Sm}_{0.2}\text{Zr}_{0.9}\text{O}_{1.9}$ , which has a melting point of 2700 °C, and thus can withstand extreme temperatures expected during hypersonic flight.<sup>9</sup>

## 1.2 Approach to Produce a Tailorable Emittance System

From a scientific standpoint, it would be helpful if emittance could be tailored at different wavelengths. For example, materials with tailorable emittance could be used to improve the efficiency of engines, thermo-photo voltaic cells, and other applications.<sup>9-11</sup> One approach to creating a ceramic with tailorable emittance would be to use two different rare-earth elements, adding them to an UHTC in small quantities. In this approach, one rare-earth element is added to increase the emittance of the UHTC over a large wavelength range (visible to near infrared wavelengths consistent with the temperature range expected for hypersonic flight) and another is added to decrease the emittance at a specific wavelength range. The end result is an UHTC, in bulk or coating form, with selective emittance. Samarium oxide has been shown to have a high emittance from visible to near IR wavelengths.<sup>12,13</sup> Erbium oxide has a demonstrated low emittance in several wavelength ranges, specifically in the 0.7-0.8  $\mu\text{m}$ , 1–1.1  $\mu\text{m}$ , and 1.7-1.8  $\mu\text{m}$  ranges.<sup>13</sup> Figures 1-2 show the emittance profiles as a function on wavelength for both  $\text{Sm}_2\text{O}_3$  and  $\text{Er}_2\text{O}_3$ .

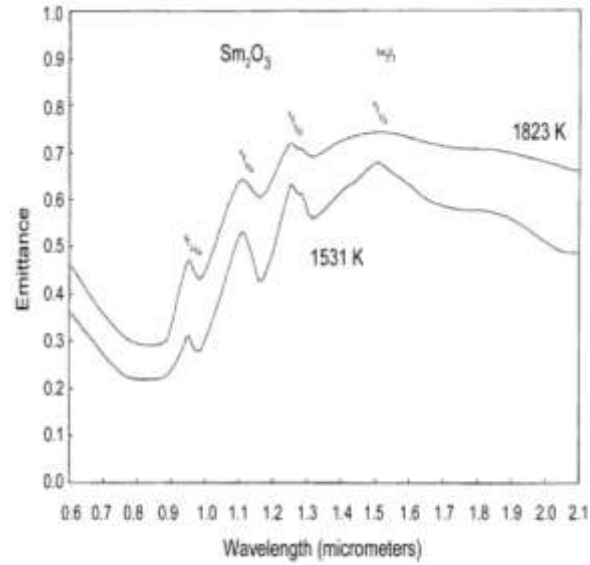


Figure 1. Emittance versus wavelength profiles for  $\text{Sm}_2\text{O}_3$ . This figure shows that  $\text{Sm}_2\text{O}_3$  has a high emittance from 1.1  $\mu\text{m}$ .<sup>13</sup>

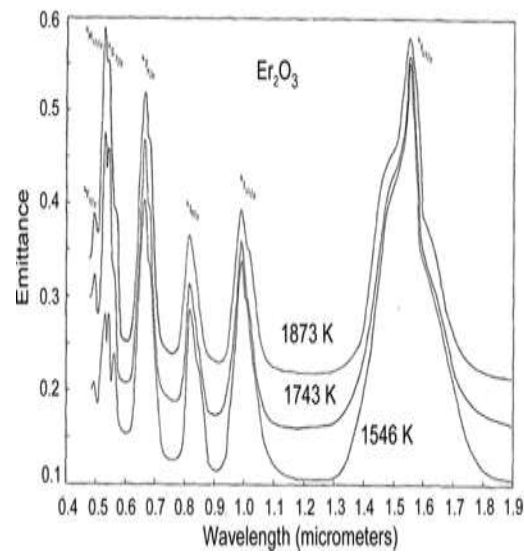


Figure 2. Emittance versus wavelength profiles for  $\text{Er}_2\text{O}_3$ . This figure shows that  $\text{Er}_2\text{O}_3$  has a low emittance in the wavelength ranges from 0.7-0.8  $\mu\text{m}$ , 1-1.1  $\mu\text{m}$ , and 1.7-1.8  $\mu\text{m}$ .<sup>13</sup>

The goal of this study is to dope an UHTC with two rare-earth elements, samarium (Sm) and erbium (Er), to evaluate the effects of Sm and Er atoms on the ablation resistance and emittance tailoring of ZBS systems in dynamic environments. Thus, for the studies presented in this



document, ZBS billets co-doped with Sm and Er in five different molar ratios were prepared with the nominal total dopant concentration constant at 3 mol.%, as showed on the Tan et al.<sup>9</sup> study. These samples were evaluated via ablation testing at 60s and 300s using an oxyacetylene torch to assess how the Sm and Er dopants affect the oxidation process, and the final oxide phase(s) stability and development. Also, the samples were tested via laser heating testing at the Air Force Research Lab facilities to evaluate the emittance tailoring as a function of dopant composition, wavelength, and temperature. Hence, the overall objective of these two studies is to produce an UHTC that possesses a tailorable emittance, strong thermal shock and ablation properties, and a high melting point.

### **1.3 Factors That Affect the UHTC During Ablation**

#### **1.3.1 Oxyacetylene Ablation Rig**

Ablation is an erosive process that implicates removal of material from a surface by a combination of chemical and mechanical reactions involving high temperature, pressure, and velocity, which cause oxidation and vaporization of the reacting materials.<sup>14</sup> Therefore, a controlled system that simulates these extreme conditions is needed to properly characterize an UHTC. Oxyacetylene ablation torch emerged as an integral part of UHTC testing for radiative cooling and solar thermal conversion applications. In this fashion, one of the best ways to simulate the hypersonic vehicle conditions and analyze the ablation phenomenon is by using an oxyacetylene combustion flame. This system will provide a more accurate and cost effective test method for investigating the candidate hypersonic aerospace materials needed to conduct fundamental research of ablation under extreme environments.<sup>15</sup>

The ablation process is affected by two main effects: heat flux and oxidation. These effects are going to determine the UHTCs temperature, phase changes, and protective oxide scales formed.

Thus, oxyacetylene torch ablation systems need to be capable of measuring heat fluxes, partial oxygen pressures, temperature, and gas flow rates. By doing that, the ablation resistance of the UHTCs in dynamic heating environments can be studied. Moreover, the oxidation scales formed can be analyzed with techniques such as SEM, EDS, AFM and XRD after ablation.

Typically, the specific oxyacetylene torch used for this type of experiment is based on the test standard ASTM E 285-80. An oxyacetylene torch can be distinguished by function of a heat flux range between 100 to 900 Watts/cm<sup>2</sup>, partial oxygen pressure range between 1 to 12 kPa, flow velocity lower than 200 meters per seconds, and gas enthalpy higher than 40 MJ/kg.<sup>14,16</sup> The effect of chemical reactions from solids on the potential enthalpic cooling effect of the flame can be determined for UHTC during ablation testing. The flame consists of combustion products H<sub>2</sub>O, H<sub>2</sub>, CO, CO<sub>2</sub>, and O<sub>2</sub>. An enthalpic cooling effect occurs in the flame, leading to a decrease in the sample surface temperature by raising the enthalpy of formation net reactions.<sup>14,16</sup> The storing of CO and CO<sub>2</sub> gases within the surface between the sample and the flame protects UHTC from rapid heating by absorbing energy from the flame.<sup>14,16</sup>

The oxygen and acetylene gases are controlled by two mass flow meters that measure the volumetric flow rate (VFR), which is defined as the ratio of oxygen to acetylene gas. To produce an oxidizing flame, the VFR should be higher than 1. As the VFR ratio rises parallel to rising oxygen content, the local heat flux is reduced while partial oxygen pressure is increased. This behavior is due to a greater amount of oxygen in combustion, which absorbs energy from the flame and results in a lower heat flux.<sup>14</sup> Another factor that affects the flame behavior is the angle between the torch and the sample. The gases will flow at a higher velocity if the flame is not perpendicular to the sample.<sup>14,16</sup> Figure 2 shows the flame length variation with the VFR ratio.

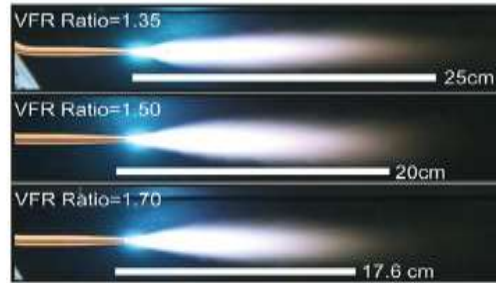


Figure 3. Flame length variation with the VFR ratio. This figure shows that the length of the flame increases by decreasing the VFR ratio.<sup>16</sup>

The oxyacetylene torch can be divided into two zones: the interior cone and the outer envelope region. The interior cone has a temperature of approximately 3500 °C.<sup>17</sup> The outer envelope has a temperature around 2100 °C in the middle part of the flame and a temperature near 1260 °C on the sharp part of the flame.<sup>18</sup> Furthermore, an oxidizing flame can be identified by three main characteristics: a sibilate noise, a light-purplish hue, and a pointed shape in the interior cone. If the oxygen content is increased, three effects will become evident: a larger interior cone, a blue flame, and an intense burning or searing sound.<sup>19</sup>

In addition to the aforementioned features, the ablation system includes an oxygen sensor that outputs the partial oxygen pressure information. The heat flux is measured with a thermogage circular foil heat flux gauge that calculates the temperature difference between the center and the circumference of the foil disk. The UHTC are placed on a sample holder that can be adjusted at different distances. The distance is measured from the torch tip to the sample. If the distance increases, the heat flux decreases exponentially due to increased amounts of atmospheric oxygen in the flame, and the partial oxygen pressure increases due to more oxygen being present. The opposite effect occurs if the distance is decreased. Figure 4 shows the local heat flux and the partial oxygen pressure as a function of the distance from the torch tip.

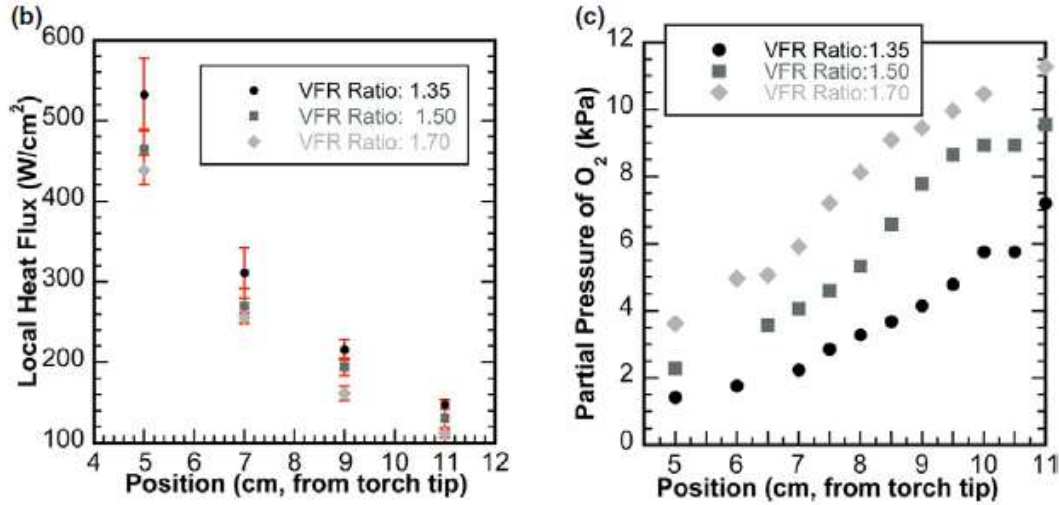


Figure 4. Position effect on local heat flux and partial oxygen pressure. This figure shows that the local heat flux decreases by increasing the distance from the torch tip, whereas the partial oxygen pressure increases by increasing the distance.<sup>16</sup>

### 1.3.2 Oxidation Effect During Ablation

During the re-entry process of hypersonic vehicles to the atmosphere, a large quantity of oxygen molecules is uncoupled into atoms, causing diffusion to the surface.<sup>1</sup> These oxygen atoms in the surface recombine into molecules which cause oxidation of the UHTC.<sup>1</sup> If the heat flux and the ablation time are increased, both the linear and mass ablation rates will increase.<sup>16</sup> Also, ablation rates increase if the partial oxygen pressure is augmented. The same effect occurs with the increase of the heat flux. The linear and mass ablation rates generated by the oxyacetylene torch flame can be calculated by the following equations:

$$R_l = \frac{t_i - t_f}{time} \quad (1)$$

$$R_m = \frac{m_i - m_f}{time} \quad (2)$$

where  $R_l$  is the linear ablation rate;  $t_i$  and  $t_f$  are the thickness before and after ablation;  $R_m$  is the mass ablation rate; and  $m_i$  and  $m_f$  are the sample weight before and after ablation. Figure 5 shows the partial oxygen pressure and heat flux effect on the oxidation rate.

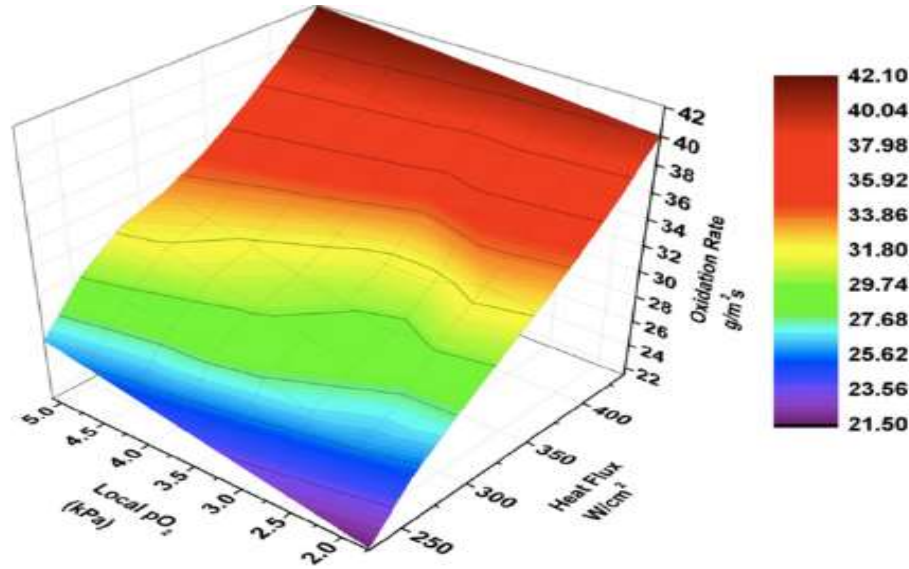


Figure 5. Partial oxygen pressure and heat flux effect on the oxidation rate. This figure shows that the oxidation rate increases by increasing both the heat flux and the partial oxygen pressure.<sup>16</sup>

The ablation rates can be computed and compared with the experimental values obtained with the ablation rig by using Fick's first law and an equation from Walker.<sup>20,21</sup> The flux of oxygen  $J_{O_2}$  can be calculated by combining both the Walker and Fick equations [equation 3] as a function of the partial oxygen pressure ( $p_{O_2}$ ), the diffusion coefficient ( $D$ ), the gas constant ( $R$ ), the temperature ( $T$ ), the viscosity of air as function of temperature ( $\mu$ ), the sample length ( $l$ ), the density ( $\rho$ ), the velocity of the specimen ( $V$ ), and the drag coefficient ( $\&$ ).

$$J_{O_2} = \frac{D \cdot p_{O_2}}{RT \& \left( \frac{\mu l}{\rho V} \right)^{0.5}} \quad (3)$$

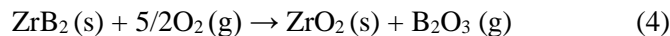
The oxidation reaction kinetics of the torch depend on the length of oxygen diffusion path through the oxide scales. Likewise, the partial oxygen pressure and oxidation temperature affect the oxidation reactions and the evaporation of oxidation products. The partial oxygen below the oxidation scales is much lower than on the surface due to the oxygen concentration gradient produced by the diffusion profile.<sup>20,21</sup> As the oxide scale thickness increase with time, the oxygen concentration gradient also decreases.

During ablation testing, the oxidizing UHTC experience multiple phase changes (melting and gaseous production) that consume energy from the flame.<sup>17</sup> ZBS samples develop an oxide layer by endothermic reactions that lower the front face temperature. The cooling effect can be obtained by detecting the enthalpy of formation reactions for gaseous oxides. Increasing the SiC content will aid in achieving the enthalpic cooling effect due to having more SiC available to react with oxygen, which results in a bigger cooling effect by SiO<sub>2</sub> evaporation.<sup>14</sup>

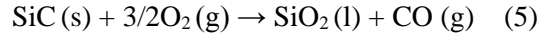
#### 1.4 Ablation Process of UHTC

The extremely high convection heating during hypersonic flights caused by the sharp leading edges requires the use of UHTC with a high melting point, high strength at temperatures above 2000 °C, and good oxidation resistance. Both ZrB<sub>2</sub> and HfB<sub>2</sub> combined with UHTC composites meet all these requirements.<sup>4,5,7,9,14,22–26</sup> Unfortunately, their poor oxidation resistance and high density can cause those UHTC to experience thermal shock failure.<sup>18</sup> Because a high thermal conductivity is needed to avoid thermal shock failure, oxidation is one of the biggest problems affecting UHTC performance.<sup>19</sup> For this reason, dense coatings are needed to avoid oxidation and increase thermal conductivity.<sup>16</sup> As SiC promotes densification with a good oxidation resistance reaching up to 1600 °C, while also improving both strength and fracture toughness, it is commonly used for hypersonic applications.<sup>5,26</sup> Studies have demonstrated that oxidation resistance improves until the percent of SiC is increased up to 20 vol.%.<sup>26</sup>

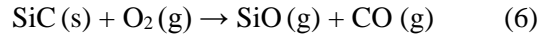
The different gases produced and the melting that occurs during the ablation process depends on the temperature. For ZBS, three main oxide scales are formed: B<sub>2</sub>O<sub>3</sub>, SiO<sub>2</sub>, and ZrO<sub>2</sub>. As B<sub>2</sub>O<sub>3</sub> glassy oxide scale forms before the SiO<sub>2</sub>, the SiC effect on ZBS coating does not show up at temperatures below 1200 °C.<sup>7,26</sup> Equation 4 defines the oxidation reaction for ZrB<sub>2</sub>.



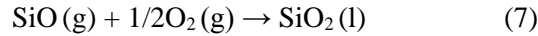
The oxidation of SiC has three main phases. During the first phase, liquid SiO<sub>2</sub> is formed to prevent oxygen diffusion.<sup>8,14</sup> Equation 5 defines the first oxidation reaction for SiC.



The second phase is governed by the active oxidation of SiC. It happens because as the thickness of the oxide scale continues to increase with time, the partial oxygen pressure between the oxide glassy layer and the bulk material decreases until it reaches a value at which the active oxidation of SiC occurs. Equation 6 defines the active oxidation for SiC.



The third phase occurs when the formed gaseous SiO diffuses to the surface and reacts with the oxygen. Equation 7 defines the oxidation of the gaseous SiO. This is caused by the gas flow at the surface due to the strong convection.



This reaction results in amorphous silica which clogs the pores on the bulk and the surface causing densification on the oxide layer.<sup>8</sup> When the temperature increases to 1500 °C, the B<sub>2</sub>O<sub>3</sub> glassy layer evaporates, leaving the surface protected just by the SiO<sub>2</sub> scale.<sup>19,23,28</sup> The dense oxide scale developed for ZBS material after oxidation up to 1500 °C is composed of a SiO<sub>2</sub> outer oxide scale and crystalline ZrB<sub>2</sub> mixed with amorphous silicate.<sup>8</sup> Figure 6 shows the ZBS dense oxide scale that is formed after ablation up to 1500 °C.

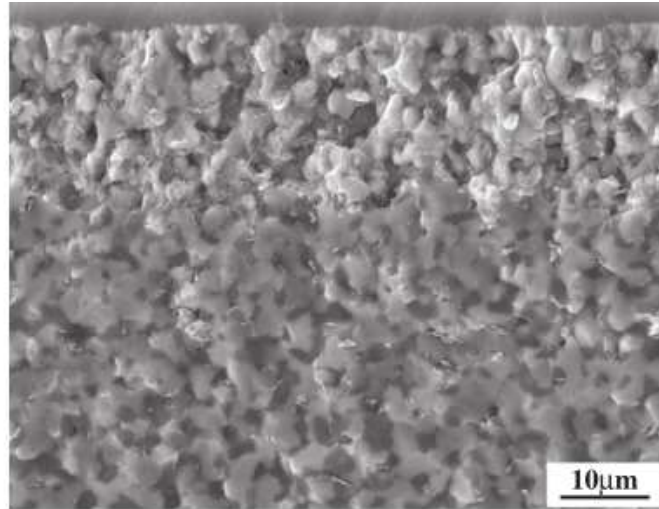


Figure 6. ZBS dense oxide scale after ablation up to 1500 °C. This figure shows that at 1500 °C the microstructure is composed of an outer protective  $\text{SiO}_2$  layer and crystalline  $\text{ZrB}_2$  mixed with amorphous silicate.<sup>14</sup>

The oxygen diffusion produced by the  $\text{SiO}_2$  oxide layer protects the UHTC from mechanical denudation. If the temperature is further increased, the  $\text{SiO}_2$  scale will evaporate if it reaches temperatures above 1600°C.<sup>5,25,29</sup> The delamination of the oxide scale is more likely to occur when the temperature is increased due to the vaporization of  $\text{SiO}_2$ ,  $\text{B}_2\text{O}_3$ , and the other gaseous products.<sup>14</sup> In addition, the vaporization of the gases below the oxide scales formed during ablation testing causes pores. The pores are formed when the gas pressure inside the bubbles is high enough to break the bubbles.

Unfortunately, the rapid evaporation rate of the oxide scale products prevents these composites from operating at temperatures above 1800 °C.<sup>30</sup> Despite all the benefits of those materials, the requirements of hypersonic applications are still not being met due to their operative temperature ranges. Therefore, increasing the radiation away from the surface emerges as the most attractive option to meet all the hypersonic application goals.

Avdoshenko and Strachan showed that the emittance of UHTC at temperatures above 2000 °C depends on three factors: the UHTC thickness, the point defects and the robustly localized



f-shell states.<sup>31</sup> First, Kirchhoff's law states that at equilibrium, the total energy absorbed is to be emitted at the same wavelength. Hence, if the thickness of the UHTC is increased, the emittance will also increase because you can absorb more energy. Second, point defects are going to affect the emittance by introducing localized electronic states within the band gap energy.<sup>9,32</sup> As the main point defect occurring in the UHTC during hypersonic flights are oxygen vacancies, they act as donors. These mid-gap locations (electronic states) promote transitions at energies within the band gap, and consequently, increase the emittance.<sup>9,31</sup> Finally, the localized *f*-shell states of the rare-earth oxides also increase the emittance by transitions of energies within the band gap.<sup>9,31</sup>

The effect of these factors on the emittance will be different depending on the material. Studies have demonstrated that the point defects effect on SiO<sub>2</sub> is negligible, the oxygen vacancies cause a huge increase in the emittance of ZrO<sub>2</sub>, and the *f*-shell electrons strongly increase the emittance of Sm<sub>2</sub>O<sub>3</sub>.<sup>31</sup> Figure 7 summarizes the effect of all these effects on the emittance.

System	Defect free	Oxygen vacancy	f-shell
SiO <sub>2</sub>	0.03(0.10)	0.04(0.08)	—
ZrO <sub>2</sub>	0.30(0.63)	0.60(0.78)	—
Sm <sub>2</sub> O <sub>3</sub>	0.15(0.58)	0.23(0.67)	0.72(0.88)

Figure 7. Emittance results for different UHTCs at 1727°C for different factors. ZrO<sub>2</sub> showed that the oxygen vacancy was the dominating factor increasing its emittance, whereas the Sm<sub>2</sub>O<sub>3</sub> showed that f-shell was the cause of the increment in the emittance values.<sup>31</sup>

Tan et al.<sup>9</sup> studies of ZBS Sm-doped coating have shown that after ablation there are three main oxide scales formed, depending on the samarium percent: *m*-ZrO<sub>2</sub>, *CI*-Sm<sub>0.2</sub>Zr<sub>0.9</sub>O<sub>1.9</sub>, and Sm<sub>2</sub>Zr<sub>2</sub>O<sub>7</sub>. Some beneficial qualities of the *CI*-Sm<sub>0.2</sub>Zr<sub>0.9</sub>O<sub>1.9</sub> oxide outer scale are that its melting point is between 2500°C and 2700°C depending on the samarium amount, has demonstrated a high

emittance, and forms a dense oxide scale.<sup>9</sup> The  $CI-Sm_{0.2}Zr_{0.9}O_{1.9}$  compound is preferred over  $Sm_2Zr_2O_7$  because the melting point of  $Sm_2Zr_2O_7$  is lower (ranges from 2190°C to 2500°C, depending on the samarium concentration). Figure 8 shows the ZBS samarium doped coating cross section micrograph for 3 mol.% Sm content (left), and 8 mol.% Sm content (right).

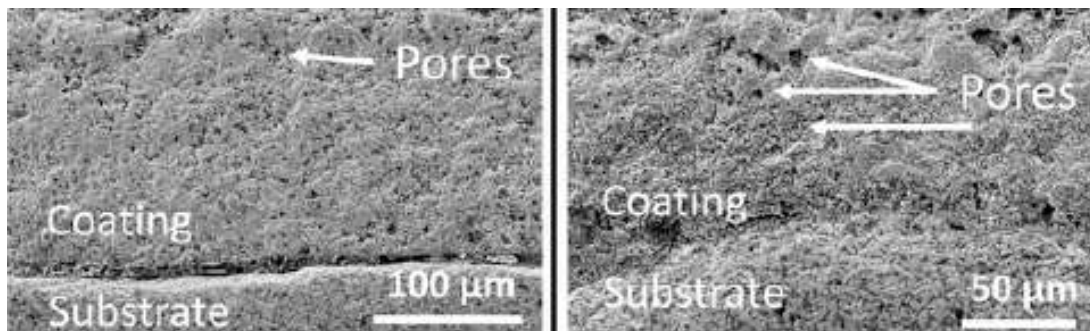


Figure 8. ZBS samarium doped coating cross section microstructure. This figure show the porosity on the oxide scale for 3 mol.% Sm content (left), and 8 mol.% Sm content (right).<sup>9</sup>

Studies demonstrated that the emittance of ZBS samples with Sm-doped will rise linearly with increasing concentration up to 5 mol% (showed a value of 0.9 at 1600 °C).<sup>9</sup> When the Sm-dopant amount is 5 mol% the oxidation products after ablation is mainly  $CI-Sm_{0.2}Zr_{0.9}O_{1.9}$  with small portions of  $Sm_2Zr_2O_7$  and  $m-ZrO_2$ . The ablated regions have a higher samarium concentration than areas under the oxide scale. Based on the discussion above, the 5 mol% Sm doped ZBS coating could be an effective approach to satisfy requirements for hypersonic applications because it provides an emittance of 0.9 at temperatures up to 1600 °C whilst providing an excellent ablation resistance up to 2200 °C.<sup>3,9</sup>

## 2. EXPERIMENTAL PROCEDURES

### 2.1 Materials and Powder Preparation

Spray-dried powders were prepared using the same method employed by Tan et al.<sup>4,9</sup> and the Brenner et al.<sup>24</sup> studies. Briefly, a lab spray dryer (APV Anhydro Model S1, Anhydro Inc, Soeborg, Denmark) was used to produce powder agglomerate from a liquid suspension feed (Aero-Instant Spraying Service, Brunswick, USA) that consisted of 80 vol.% ZrB<sub>2</sub> (3–5  $\mu$ m, Grade A, HC Starck, Munich, Germany), 20 vol.%  $\alpha$ -SiC (1.4  $\mu$ m, Grade UF-05, HC Starck, Munich, Germany), 0.4 wt.% dispersant (Darvan 821A, R.T. Vanderbilt Company, Inc., Norwalk, USA), 2 wt.% PVA binder (Celvol 203, Celanese Corporation, Dallas, USA) and deionized water. The suspension was fed into the drying chamber by using a spraying nozzle, where the air was heated to 200 °C. Then, a rotary atomizer spun at ~30,000 rpm was used to atomize the suspension into controlled-size droplets. The temperature at the outlet was ~105 °C. The average particle size of the spray-dried granules, which was obtained by using a Malvern Mastersizer 2000 (Malvern Instrument Ltd., Worcestershire, UK), was approximately 38  $\mu$ m. Figure 9 shows a SEM micrograph of the undoped spray dried ZrB<sub>2</sub>-20 vol% SiC particles.

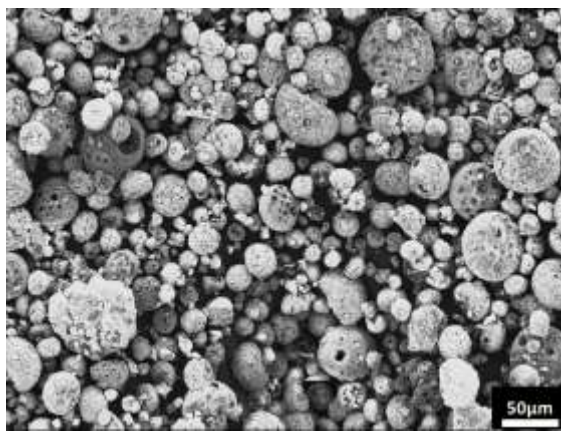


Figure 9. SEM micrograph of undoped spray dried 80 vol.% ZrB<sub>2</sub> - 20 vol% SiC particles showing the particle size of the granules. The vol.% calculations for the ZrB<sub>2</sub> and SiC were based on a total volume of 10 cm.<sup>3</sup>

Samarium and/or erbium dopants were added to the spray dried  $\text{ZrB}_2/\text{SiC}$  powders via a chemical infiltration method. In this process, for every 55.10 g of spray dried granules (6.42g of  $\text{SiC}$  + 48.68 g of  $\text{ZrB}_2$ ), samarium nitrate hexahydrate (99.9% pure  $\text{Sm}(\text{NO}_3)_3 \cdot 6\text{H}_2\text{O}$ , MSE Supplies, Arizona, USA) and/or erbium nitrate hexahydrate (99.9% pure  $\text{Er}(\text{NO}_3)_3 \cdot 6\text{H}_2\text{O}$ , MSE Supplies, Arizona, USA) were dissolved into 99.9% pure isopropyl alcohol, and the resulting solution was then infiltrated into the porous spray-dried  $\text{ZrB}_2/\text{SiC}$  powder. Solutions mixed in five different molar ratios (1Sm:0Er, 2Sm:1Er, 1Sm:1Er, 1Sm:2Er and 0Sm:1Er) were prepared; the total rare-earth nitrate hexahydrate compound was added at an initial combined concentration of 10 mol.% of  $\text{Sm}(\text{NO}_3)_3 \cdot 6\text{H}_2\text{O}$  and  $\text{Er}(\text{NO}_3)_3 \cdot 6\text{H}_2\text{O}$ . For example, the 2Sm:1Er billet was to contain 6.66 mol.%  $\text{Sm}(\text{NO}_3)_3 \cdot 6\text{H}_2\text{O}$  and 3.33 mol.%  $\text{Er}(\text{NO}_3)_3 \cdot 6\text{H}_2\text{O}$  in the  $\text{ZrB}_2/\text{SiC}$  matrix. To do that 18.9 g of  $\text{Sm}(\text{NO}_3)_3 \cdot 6\text{H}_2\text{O}$  and 9.3 g of  $\text{Er}(\text{NO}_3)_3 \cdot 6\text{H}_2\text{O}$  were infiltrated on every 55.1 g of spray-dried granules. Afterwards, the alcohol and likely some of the water was removed via a rotary evaporator (BM 200, Yamato Scientific America Inc., Santa Clara, USA) at 100°C. This powder was heated at 500 °C in air for an hour to remove residual moisture, water, and nitrates. Tan et al.<sup>4</sup> performed a study of the normalized weight gain as a function of temperature from 200-1300°C, demonstrating that below 600 °C both the ZBS and the Sm-doped coatings exhibit no weight gain that would be associated with oxidation of  $\text{ZrB}_2$  to form  $m\text{-ZrO}_2$  and  $\text{B}_2\text{O}_3$  glass. These results are consistent with temperature transitions reported by Bartuli et al.<sup>33</sup> for  $\text{ZrB}_2/\text{SiC}$  coatings, providing further evidence that the ZBS did not have any weight gain below 600 °C. The first weight gain inflections start near 600°C, due to the oxidation of  $\text{ZrB}_2$ , to form  $m\text{-ZrO}_2$  and  $\text{B}_2\text{O}_3$  glass.<sup>4</sup> However, the combined 10 mol.% of  $\text{Sm}(\text{NO}_3)_3 \cdot 6\text{H}_2\text{O}$  and  $\text{Er}(\text{NO}_3)_3 \cdot 6\text{H}_2\text{O}$  was reduced to 5 mol% of combined  $\text{Sm}_2\text{O}_3$  and  $\text{Er}_2\text{O}_3$ , assuming the Sm and Er all oxidizes to  $\text{Sm}_2\text{O}_3$  and  $\text{Er}_2\text{O}_3$  in air at 500 °C. After nitrate, water and moisture removal at 500 °C, the dried mixture was sieved using

a 60-mesh (250  $\mu\text{m}$  aperture) to eliminate large agglomerates. For ZBS powders/dopant ratios, ~20% by weight was lost during the 500  $^{\circ}\text{C}$  heat treatment. These losses are owed to the evaporation of the nitrates and water. ZBS powders with different ratios of Sm and/or Er dopants were die pressed at 82 MPa. The pressed billets were heated to 1650  $^{\circ}\text{C}$ , held for 1 hr, heated to 2000  $^{\circ}\text{C}$ , held for 15 min, and then cooled to room temperature. Sintering occurred in an argon atmosphere with graphite heating elements at a partial oxygen pressure of 15 MPa. Samples were cut into 25.4 mm x 25.4 mm squares.

The billets were polished to ~0.1  $\mu\text{m}$  using an auto polisher, where the billets were polished first to 6  $\mu\text{m}$ , then to 3  $\mu\text{m}$ , and finally to 0.1  $\mu\text{m}$ . The bulk density of each billet for each ratio of Sm:Er was measured by the Archimedes methodology, as described in the ASTM C373-88 standard. Surface roughness ( $R_a$ ) was measured using an AFM (AS0200 AlphaStep, Tencor Corporation, Milpitas, USA). To help simplify discussion, the naming convention is on the intended molar ratios. For instance, the 2Sm:1Er billet was to contain 6.66 mol.%  $\text{Sm}(\text{NO}_3)_3 \cdot 6\text{H}_2\text{O}$  and 3.33 mol.%  $\text{Er}(\text{NO}_3)_3 \cdot 6\text{H}_2\text{O}$  in the  $\text{ZrB}_2/\text{SiC}$  matrix. The amount of Sm and Er incorporated into the samples was measured by mass spectroscopy with fusion preparation on pulverized billets (NSL Analytical Services Inc., Cleveland, USA).

## 2.2 Oxyacetylene Ablation Testing

Heat flux conditions and ablation resistance were assessed using an oxyacetylene ablative torch rig. The test rig was constructed using ASTM E285-082 as a standard. The ablation torch (Victor Technologies, St. Louis, USA) used a 5 mm orifice, and a separation distance of 20 mm between the sample and the torch tip was held constant. An oxygen rich environment was simulated using an oxygen:acetylene ratio of 12:10 slpm. The heat flux was measured to be  $452 \pm 6.8 \text{ W/cm}^2$  using a thermogage circular foil heat flux gauge (TG1000-4, Vatel Corp.,

Christiansburg, VA). The circular-foil heat flux gauge has a water-cooler system which continuously provides an active heat sink that removes the absorbed heat, especially for applications with longer measurement times or high heat flux levels. Also, the thermogage sensor is coated with colloidal graphite. Front surface temperatures as a function of time were measured using a single-color pyrometer (OS3750, Omega Engineering Inc., Stamford, CT, USA) which was connected to a data logger. The single-color pyrometer had a target size for temperature measurements of 20 mm diameter which was positioned on the sample where the flame was the hottest. The maximum temperature values from the target size area were measured at a spectral band of 1.55  $\mu\text{m}$  and reported with an accuracy rating of  $\pm 1.2\%$  from the measured value. The emittance setting for the pyrometer was set to be 0.9. Five test specimens were exposed to 60 s intervals of flame and other five test specimens to 300 s intervals of flame. Samples were cooled to room temperature and characterized.

### **2.3 Microstructural and Phase Analysis**

Before performing the microstructural analysis, the samples were coated with a thin layer of Au/Pd. A scanning electron microscope (SEM) (Phillips XL-40, FEI Co., Hillsboro, USA) was used to characterize billet topography in the pre-ablated and post-ablated conditions. X-ray diffraction (XRD) (D8 Focus, Bruker Corporation, Billerica, USA) was used to identify the phases present using Cu  $K_{\alpha}$  radiation for  $2\theta$  values of  $20^{\circ}$ - $80^{\circ}$  on the billets before ablation, and for  $2\theta$  values of  $15^{\circ}$ - $80$  after ablation. A step size of  $0.02^{\circ}$  and a scan rate of  $5^{\circ}/\text{minute}$  was used for all samples. Samples were positioned in the XRD to analyze the regions where the ablation flame was most intense.

An Energy Dispersive X-Ray Spectroscopy (EDS) analyze technique was used on the samples before and after the ablation and emittance studies to know the elements concentrations. The system uses a silicon drift detector (SDD), has a maximum energy resolution of 127 eV, has a resolution stability higher than 90%, uses a silicon nitrate window with honeycomb grid for element detection down to Al L (73eV), uses a 1:1 Al K $\alpha$  peak ratio at 2.5 kV, and operates with a sensor area of 70 mm<sup>2</sup>. The working distance was set to 10 mm, the spot size was to set to 6, an acceleration voltage of 25 kV, and an aperture of 50  $\mu$ m. The EDS detector settings used for the EDS-line scans were the following: a dead time (DT) between 20-40 DT%, and a detector counts per second (CPS) of 150,000 CPS.

## **2.4 Laser Heating Testing**

Emittance testing was performed in the RHINO lab at the Airforce Research Laboratory (AFRL) in Dayton, Ohio. The samples were placed in a graphite holder where both the front face and back face of the sample were exposed. The back face of the sample was then heated with a laser powered at 700 W, 800 W, or 900 W and held for a total time of 80 s. During the laser heating testing, spectral radiance data was collected by a spectrometer from the front side of the samples, with intervals of 1 s, across the wavelength range. The sensor collected spectral radiance measurements from 1500-5000 nm with intervals of 14.2 nm (246 wavelength points).

### 3. EVALUATION OF RARE-EARTH ELEMENT DOPANTS (SAMARIUM AND ERBIUM) ON THE ABLATION RESISTANCE OF ZIRCONIUM DIBORIDE/SILICON CARBIDE SINTERED BILLETS

A version of this chapter has been published in the Journal of American Ceramic Society.<sup>23</sup>

The way in which rare-earth dopant elements (samarium and erbium) affect the scale development of sintered  $\text{ZrB}_2/\text{SiC}$  (ZBS) samples during ablation testing is investigated at present. ZBS billets with five different Sm to Er ratios and with a nominal total amount of 3 mol.% dopant incorporated, were prepared by sintering in vacuum to 2000 °C and subjected to 60s and 300s ablation cycles. Differences in surface temperatures between ZBS samples with different dopant ratios suggest dissimilarities in spectral absorptance/emittance between each of the five compositions investigated. ZBS billets co-doped with Sm and Er form a beneficial  $c_I$ - $(\text{Sm/Er})_{0.2}\text{Zr}_{0.8}\text{O}_{1.9}$  oxide scale as the majority phase, with some glassy phase observed. The crystalline  $c_I$ - $(\text{Sm/Er})_{0.2}\text{Zr}_{0.8}\text{O}_{1.9}$  oxide scale is more crystallographically stable than the  $m$ - $\text{ZrO}_2$  oxide scale typically formed in oxidized ZBS systems, resulting in a more adherent oxide scale to the unreacted material. The crystalline oxide scale and the amorphous phase are formed by a convection cell mechanism where the  $c_I$ - $(\text{Sm/Er})_{0.2}\text{Zr}_{0.8}\text{O}_{1.9}$  crystalline islands precipitate, grow, and coalesce.

## 3.1 Results

### 3.1.1 Pre-ablated Sintered Samples Results

The actual concentrations of Sm (mol.%) and Er (mol.%) incorporated into each billet are listed in Table 1, along with the measured bulk density, theoretical density, total porosity (%), and surface roughness.



Table 1. Samarium and erbium dopant concentration and properties after sintering. All sintered billets nominally contained 80 vol% ZrB<sub>2</sub> - 20 vol% SiC. The bulk density calculation is based on final density after the sintering process.

	Sm(NO <sub>3</sub> ) <sub>3</sub> ·6H <sub>2</sub> O Added (mol%)	Er(NO <sub>3</sub> ) <sub>3</sub> ·6H <sub>2</sub> O Added (mol%)	Actual Sm Incorporated (mol%)	Actual Er Incorporated (mol%)	Bulk Density (g/cm <sup>3</sup> )	Theoretical Density (g/cm <sup>3</sup> )	Total Porosity (%)	Surface Roughness, Ra (nm)
1Sm:0Er	10	0	2.94	0	3.91	5.67	31.0	102 ± 12
2Sm:1Er	6.6	3.3	1.85	1.23	4.74	5.83	18.7	95 ± 15
1Sm:1Er	5	5	0.97	1.80	4.77	5.86	18.0	105 ± 14
1Sm:2Er	3.3	6.7	0.95	2.33	4.82	6.00	19.7	108 ± 8
0Sm:1Er	0	10	0	3.11	4.97	6.02	17.4	104 ± 11

It was observed that ~3 mol.% rare-earth element(s) were incorporated into the sintered billets, ~1/3 of the 10 mol.% rare-earth nitrate hexahydrate compounds during the chemical doping process. It should be noted that most of this reduction in the dopant concentration was caused by the heat treatment at 500°C where the water and nitrates were removed, and not because the Sm and Er were lost. It must be recalled that the 10 mol.% added during the chemical doping process is referring to the combined Sm(NO<sub>3</sub>)<sub>3</sub>·6H<sub>2</sub>O and Er(NO<sub>3</sub>)<sub>3</sub>·6H<sub>2</sub>O. Therefore, the combined concentrations of Sm (mol.%) and Er (mol.%) represents ~35% (~3.5 mol.%) of 10 mol.% added during the chemical doping process. Because ~3 mol.% dopant(s) were incorporated into the sintered billets, it can be concluded that the remaining ~0.5 mol.% was lost during powder handling or during sintering. These results are different than the ones presented in Tan et al.<sup>4,9</sup> studies and Brenner et al.<sup>24</sup> study where 5 mol.% Sm dopant was incorporated into plasma-sprayed coatings. The decrease of ~2 mol.% of the dopant(s) incorporated into the sintered billets of the present study were caused by the different method used to prepare the samples, as the samples used in Tan et al.<sup>4,9</sup> studies and Brenner et al.<sup>24</sup> study were prepared using a plasma spray process.

Table 1 displays that more Er dopant was integrated into the sample than Sm dopant. This is apparent by comparing the 1Sm:0Er and 0Sm:1Er billets, where 2.94 mol.% of Sm and 3.11 mol.% of Er were incorporated respectively. This difference is explained by the variation in their

molar mass, where Sm represents the 33.8% of the 10 mol.%  $\text{Sm}(\text{NO}_3)_3 \cdot 6\text{H}_2\text{O}$  added during the chemical doping process for the 1Sm:0Er billet, whereas Er represents 36.3% of the 10 mol.%  $\text{Er}(\text{NO}_3)_3 \cdot 6\text{H}_2\text{O}$  added for the 0Sm:1Er billet. Surface roughness ( $R_a \sim 100$  nm) was all similar, consistent with using the same polishing procedures for each billet investigated. Samples ranged from 17 to 31% in total porosity.

XRD results on the billets before ablation testing, presented in Figure 10, were an indication that  $\text{ZrB}_2$  is the majority phase with a small peak at  $35.5^\circ$  identified as  $\alpha\text{-SiC}$ . For the 1Sm:0Er and 0Sm:1Er samples, the small intensity peaks between  $2\theta$  of  $23\text{-}35.5^\circ$  correspond to  $\text{Sm}_2\text{O}_3$  and  $\text{Er}_2\text{O}_3$  respectively. For the 2Sm:1Er, 1Sm:1Er, and 1Sm:2Er pre-ablated samples, the XRD results show a similar  $(\text{Sm/Er})_2\text{O}_3$  phase due to the Sm and Er atoms exchanging positions because of their similar ionic size ( $242$  pm for Sm and  $236$  pm for Er). The peaks were shifted to larger  $2\theta$  due to the smaller interplanar spacing caused by the slightly smaller erbium atoms. As was noted in the XRD results, the Sm and Er compounds and the alloys oxidized to some extent in the high purity Ar atmosphere during the sintering process.

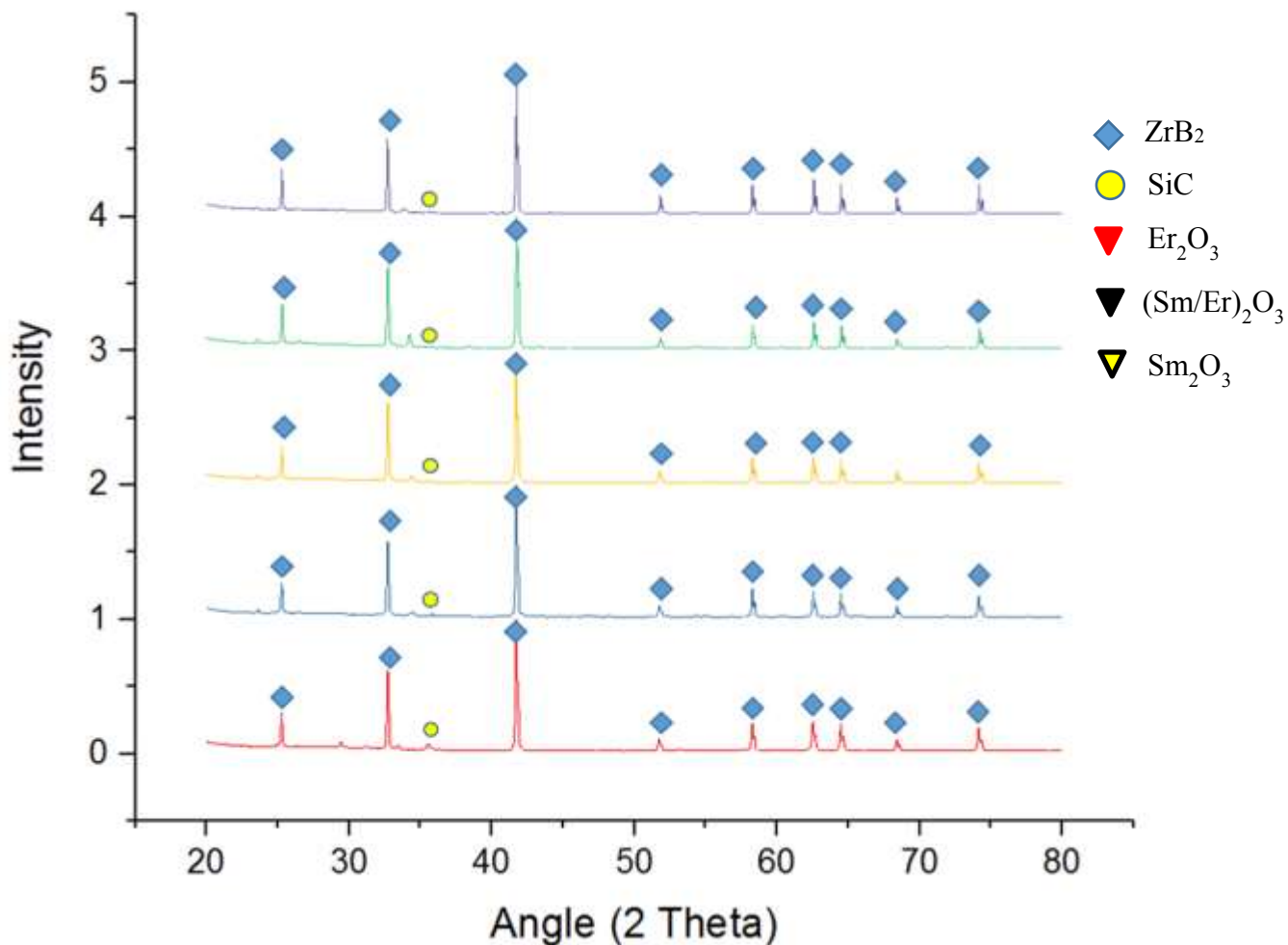


Figure 10. X-ray diffraction patterns of the surface of the pre-ablated sintered samples. This figure shows that  $\text{ZrB}_2$  was the major phase with small portions of  $\text{SiC}$  and  $(\text{Sm/Er})_2\text{O}_3$ .

Figures 11a-e compare the SEM micrographs of the surface of the billets before the ablation testing. The XRD results in Figure 10, indicating the primary phase to be  $\text{ZrB}_2$ , were further verified by EDS results for each sample, which showed  $\text{ZrB}_2$  grains of approximately a 1:2 ratio of Zr to B atoms. The grains were surrounded by a matrix composed mainly of Sm and Er with small portions of O, Si, and C. The small portion of Si and C in the EDS results also matches with the small  $\alpha$ - $\text{SiC}$  peak identified at  $35.5^\circ$  in the XRD plot in Figure 10.

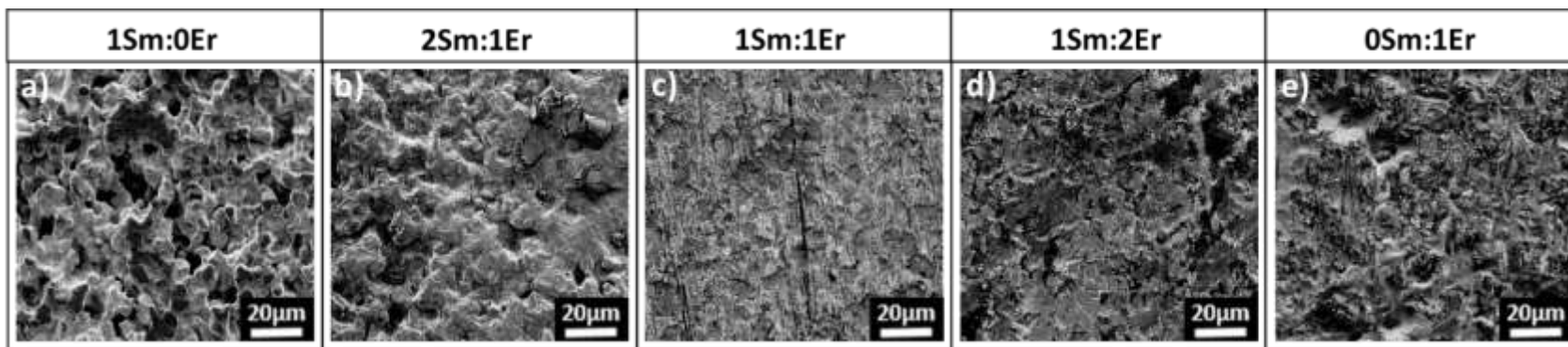


Figure 11. SEM micrographs of the surface of the pre-ablated sintered billets for: a) 1Sm:0Er, b) 2Sm:1Er, c) 1Sm:1Er, d) 1Sm:2Er, and e) 0Sm:1Er. EDS results on his figure show that the pre-ablated microstructure of the sintered billets was composed of  $\text{ZrB}_2$  grains surrounded by a matrix composed mainly of Sm and Er with small portions of O, Si, and C.

### 3.1.2 Ablation Results After 60s

Figure 12 shows a plot of front surface temperature as a function of time during the 60 s ablation cycle for each of the five billets tested. All the samples displayed a continuous temperature increase through the 60 s of heating, with a rapid increase in temperature followed by a much slower increase in temperature. The maximum temperatures during the ablation cycle were the highest for the 0Sm:1Er and 1Sm:2Er samples at  $1717 \pm 21$  °C and  $1715 \pm 21$  °C, respectively, and the lowest for the 2Sm:1Er sample at  $1612 \pm 19$  °C. The maximum temperatures for the 1Sm:0Er and 1Sm:1Er samples were  $1690 \pm 20$  °C and  $1672 \pm 20$  °C, respectively. The temperature at which the rate of heating slows down is different for all the samples. The inflection point temperature was the highest for the 0Sm:1Er sample at  $1600 \pm 19$  °C after ablating for 12 s, and the lowest for the 2Sm:1Er sample  $1300 \pm 16$  °C after ablating for 9 s.

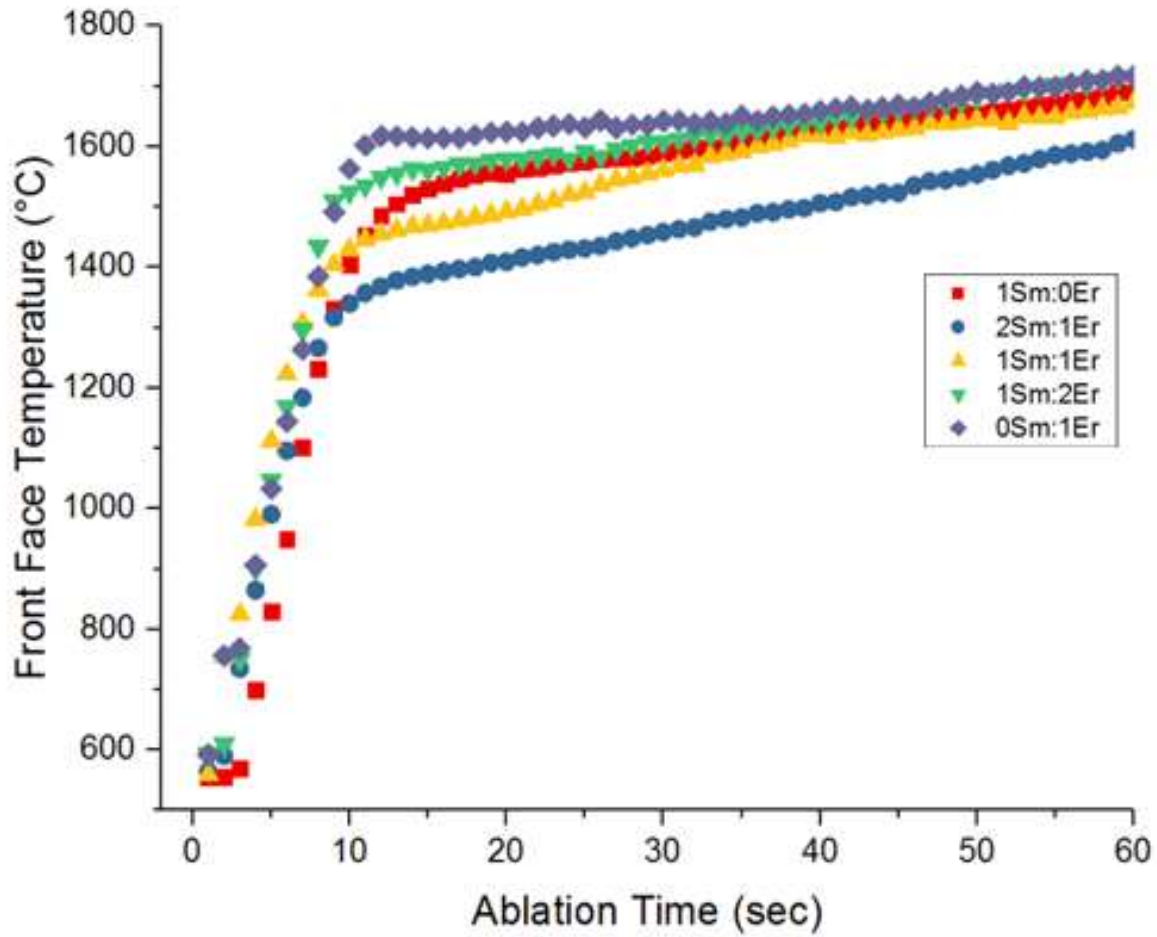


Figure 12. Front surface temperature during ablation testing for 60 s. This figure shows that the samples reached temperatures above 1700 °C with the 2Sm:1Er sample showing the lowest front-face temperatures.

Figures 13a-e compare the ablated surfaces after the 60 s ablation cycle. Each of the Sm:Er billets developed an adherent oxide scale. The oxide scale color changes relative to the amount of Sm and Er dopant from yellow in the 1Sm:0Er sample to pink in the 0Sm:1Er sample.

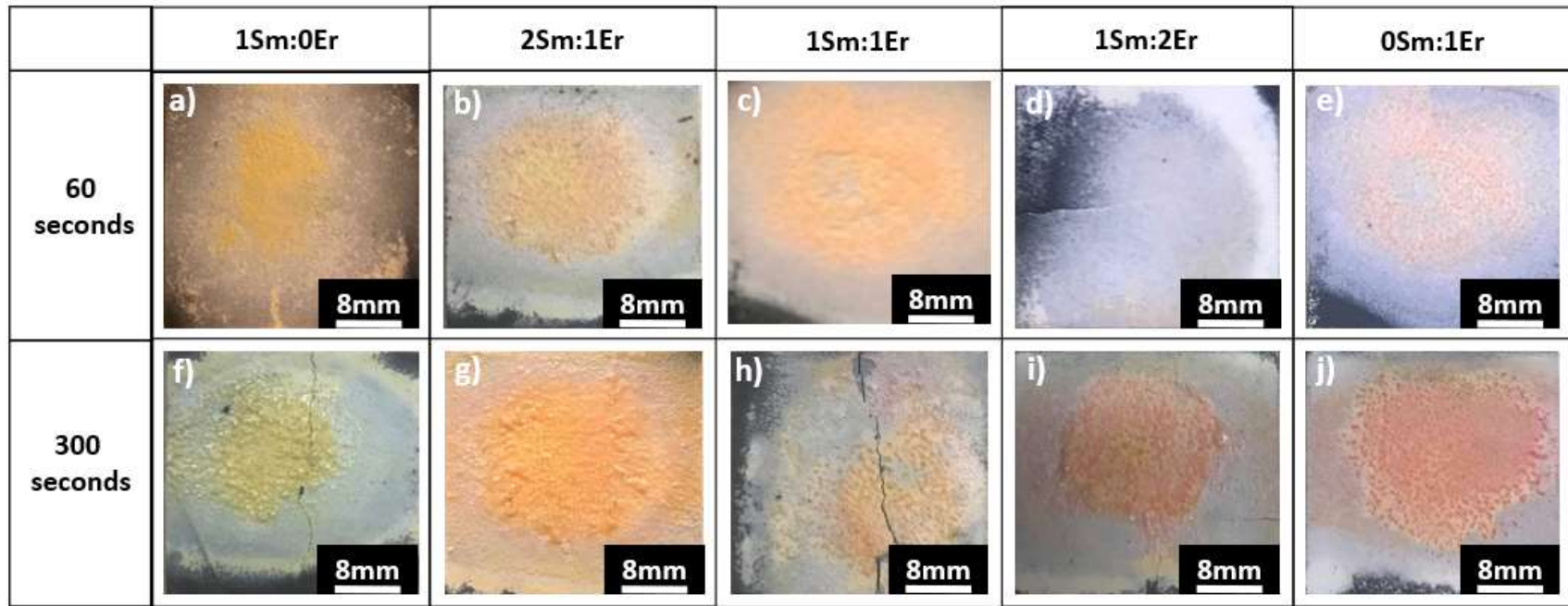


Figure 13. Optical images of the ablated billets: a) 1Sm:0Er, b) 2Sm:1Er, c) 1Sm:1Er, d) 1Sm:2Er, and e) 0Sm:1Er after 60 s, and f) 1Sm:0Er, g) 2Sm:1Er, h) 1Sm:1Er, i) 1Sm:2Er, and j) 0Sm:1Er after 300 s. This figure shows that the amount of glassy phase increases as the ablation time increases from 60 s to 300 s.

Figures 14a-e compare SEM micrographs of the surface of the billets after ablating for 60 s. For all the Sm:Er samples, the surface appears to have clusters of crystalline islands surrounded by an amorphous phase. Figures 14a-c show that the crystalline islands become larger as the Sm concentration is increased from 0.97 mol.% in the 1Sm:1Er sample to 2.94 mol.% in the 1Sm:0Er sample. Additionally, the 1Sm:1Er billet shows the presence of pores and dendrites, whilst the 1Sm:0Er billet shows a “flower-like” microstructure.

The post-ablation XRD results from the 1Sm:0Er sample, presented in Figure 15, match with previous studies<sup>9</sup> where the major phase formed was the cubic samarium zirconium oxide scale ( $cI$ -Sm<sub>0.2</sub>Zr<sub>0.8</sub>O<sub>1.9</sub>, JCPDS-01-78-1302). For the ablated 2Sm:1Er, 1Sm:1Er, and 1Sm:2Er billet samples, the XRD results show a similar cubic structure ( $cI$ -(Sm/Er)<sub>0.2</sub>Zr<sub>0.8</sub>O<sub>1.9</sub>) as the major phase due to the Sm and Er atoms exchanging positions because of their similar ionic size (242 pm for Sm and 236 pm for Er). The primary peaks were shifted to larger  $2\theta$  because of the smaller interplanar spacing caused by the slightly smaller erbium atoms. Lattice parameters of 0.517 nm, 0.513 nm, 0.511 nm, 0.510 nm, and 0.507 nm were measured for  $cI$ -(Sm/Er)<sub>0.2</sub>Zr<sub>0.8</sub>O<sub>1.9</sub> from the 1Sm:0Er, 2Sm:1Er, 1Sm:1Er, 1Sm:2Er and 0Sm:1Er samples, respectively. These results follow the Vegard's law in view of the interplanar spacing decreasing almost linearly as the Sm dopant concentration is increased. Small portions of monoclinic zirconia ( $m$ -ZrO<sub>2</sub>, JCPDS-00-37-1484) were also observed. Finally, the ablated 0Sm:1Er sample was primarily cubic erbium zirconium oxide scale ( $cI$ -Er<sub>0.2</sub>Zr<sub>0.8</sub>O<sub>1.9</sub>) with small amounts of  $m$ -ZrO<sub>2</sub>.



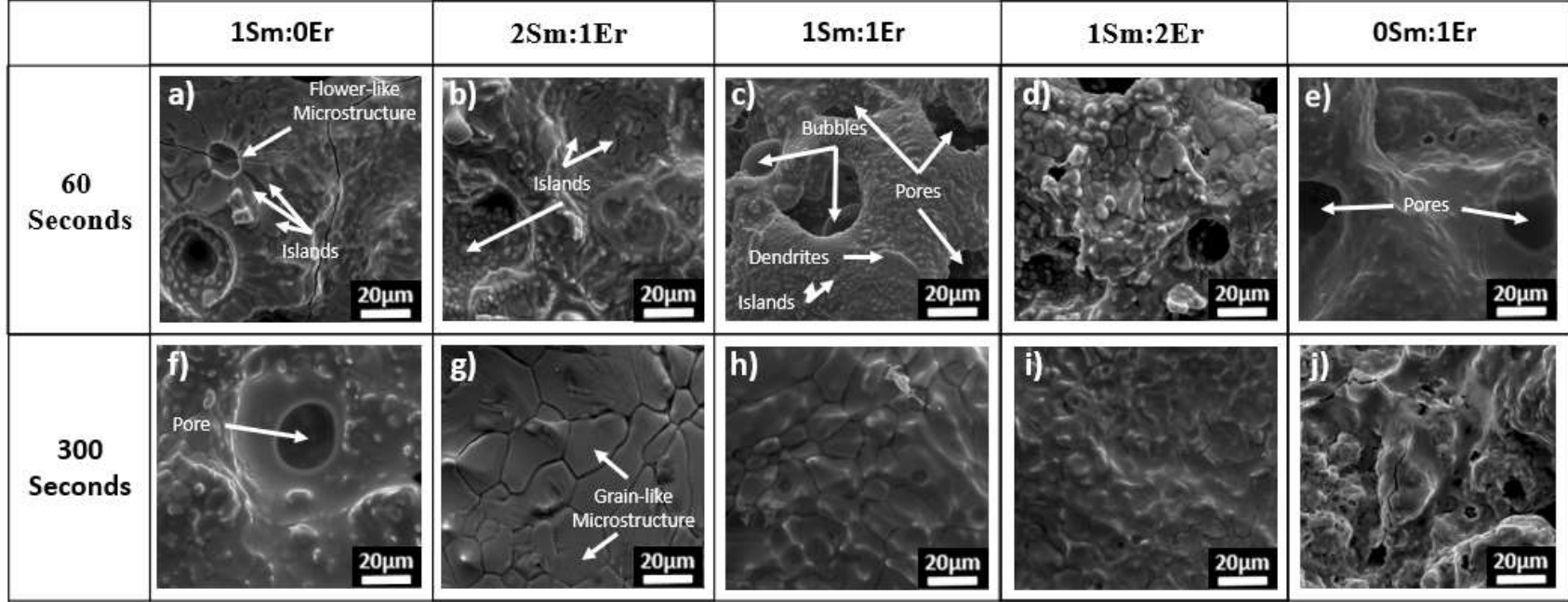


Figure 14. SEM micrographs of the following billets: a) 1Sm:0Er, b) 2Sm:1Er, c) 1Sm:1Er, d) 1Sm:2Er, and e) 0Sm:1Er after 60 s, and f) 1Sm:0Er, g) 2Sm:1Er, h) 1Sm:1Er, i) 1Sm:2Er, and j) 0Sm:1Er after 300 s. The results after ablation for 60 s show the  $c_{I-(\text{Sm/Er})_{0.2}\text{Zr}_{0.8}\text{O}_{1.9}}$  crystalline islands that form by a convection cell mechanism. The results after ablation for 300 s show that as the ablation time is increased, the  $c_{I-(\text{Sm/Er})_{0.2}\text{Zr}_{0.8}\text{O}_{1.9}}$  crystalline islands will grow, coalescence and form a grain-like structure as shown by the Figures 14g-i.

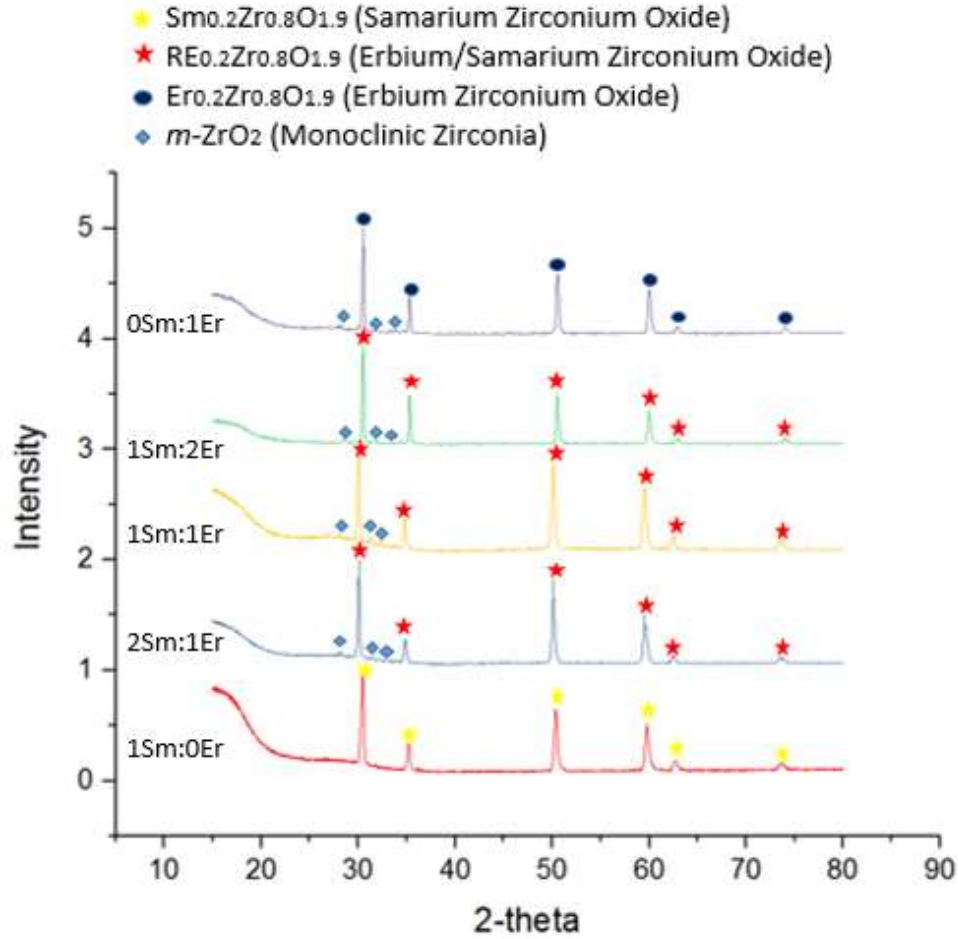


Figure 15. X-ray diffraction patterns of the surface after 60 s. This figure shows that  $c_I\text{-(Sm/Er)}_{0.2}\text{Zr}_{0.8}\text{O}_{1.9}$  was the major phase with minor portions of  $m\text{-ZrO}_2$ .

### 3.1.3 Ablation Results After 300 s

The ablation results from the samples evaluated for 60 s were compared with the first 60 s of the samples ablated for 300 s to test the variation of the temperature measurements with time. The standard deviation of each time point was calculated, and then, these 60 standard deviation values were used to calculate their 95% confidence interval. The variations of the temperature measurements were small, varying from  $37 \pm 4.2$  °C,  $8.8 \pm 4.3$  °C,  $8.3 \pm 4.1$  °C,  $5.9 \pm 3.2$  °C, and  $8.1 \pm 4.2$  °C for the compositions 1Sm:0Er, 2Sm:1Er, 1Sm:1Er, 1Sm:2Er, and 0Sm:1Er, respectively.

Figure 16 displays the front surface temperature during the 300 s ablation cycle. The maximum temperature during the ablation cycle was the highest for the 1Sm:2Er sample at  $2037 \pm 24$  °C. Maximum temperatures of  $1968 \pm 24$  °C,  $1946 \pm 23$  °C,  $1947 \pm 23$  °C and  $1947 \pm 23$  °C were measured for the 1Sm:0Er, 2Sm:1Er, 1Sm:1Er, and 0Sm:1Er samples, respectively. During the first 100 s of ablation, the 2Sm:1Er sample showed the lowest front face temperature. Excluding the 1Sm:2Er sample, the temperature difference between the other 4 compositions studied after ablation for 100 s seem to be very similar. All the samples displayed a continuous temperature increase through the 300 s of heating but were significantly hotter ( $\sim 300$  °C) than the samples ablated for 60 s. As the ablation time is increased from 60 s to 300 s, a second inflection point, in addition to the first one previously described, can be seen for all the five Sm:Er molar ratios. The inflection point occurs at approximately  $1700 \pm 20$  °C after ablation for 75 s.

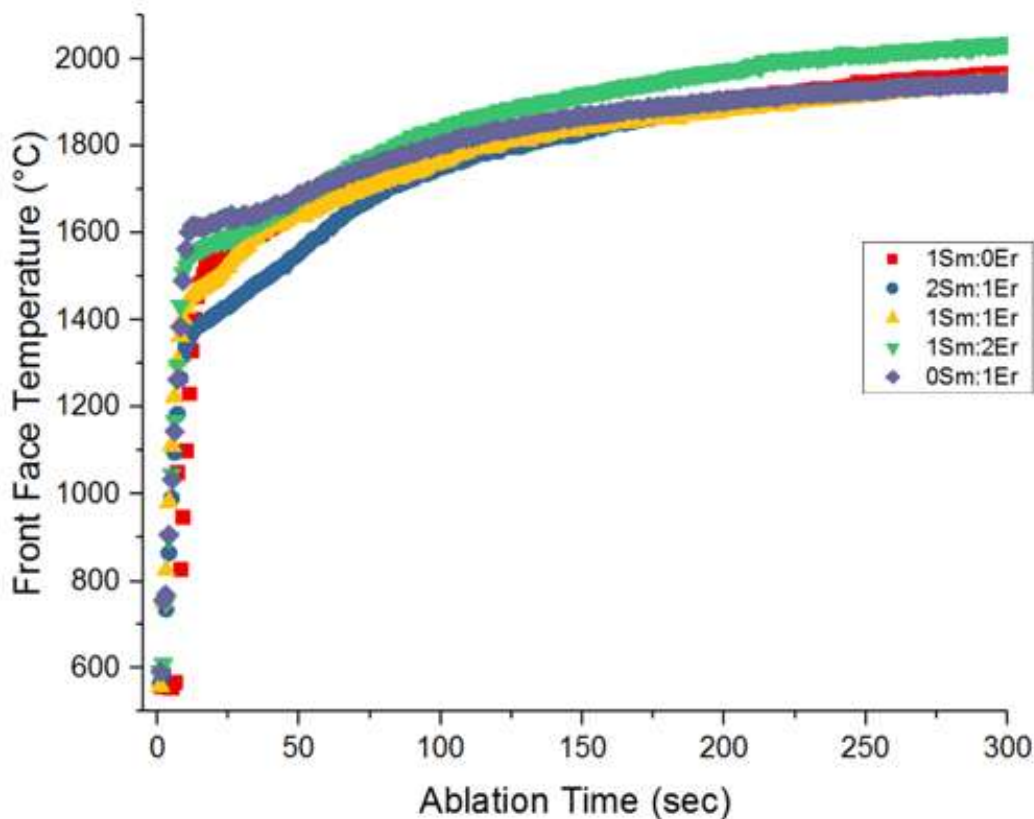


Figure 16. Front surface temperature during ablation testing for 300 s. This figure shows that the samples reached temperatures above 2000 °C after 300 s of ablation.

Figures 13f-j show the ablation surface micrograph comparison of the samples after the 300 s ablation cycle. Each of the Sm:Er billets developed an adherent oxide scale. The oxide scale color changed relative to the amount of Sm and Er dopant, just as in the 60 s ablation cycle, from yellow in 1Sm:0Er to pink in 0Sm:1Er. It was observed that more amorphous phase was present when the ablation time was increased from 60 s to 300 s. It should be noted that the cracks shown on the 1Sm:0Er and 1Sm:1Er samples were caused by removing the samples from the ablation rig.

Figures 14f-j present the surface topography of the ablated samples after 300 s. The crystalline islands observed in the first 60 s of ablation from the 2Sm:1Er, 1Sm:1Er, and 1Sm:2Er samples have increased in size and coalesced. Therefore, a grain like-structure is evident in the three samples containing both Sm and Er dopants (Figures 14g-i), whereas a glassy phase is covering the crystalline grain-like structure. The amount of glassy phase on these three samples appears to increase as the Er concentration increases. On the contrary, the 1Sm:0Er and 0Sm:1Er samples did not show the grain-like structure. Figure 14f shows that in the 1Sm:0Er sample the crystalline islands formed after 60 s have increased in size but maintained the amorphous lagoon surrounding them. Figure 14j shows that the 0Sm:1Er sample has a similar microstructure to the 1Sm:0Er.

Figure 17 displays the XRD results obtained from the surface of the samples after the 300 s ablation cycle. The XRD of the samples after ablation for 300 s remained unchanged, being primarily composed of  $c\text{-}I\text{-(Sm/Er)}_{0.2}\text{Zr}_{0.8}\text{O}_{1.9}$  as the major phase with small amounts of  $m\text{-ZrO}_2$  observed. More amorphous phase, as evidenced by the humps in the Figure 17 XRD data, is apparent after 300 s of ablation.

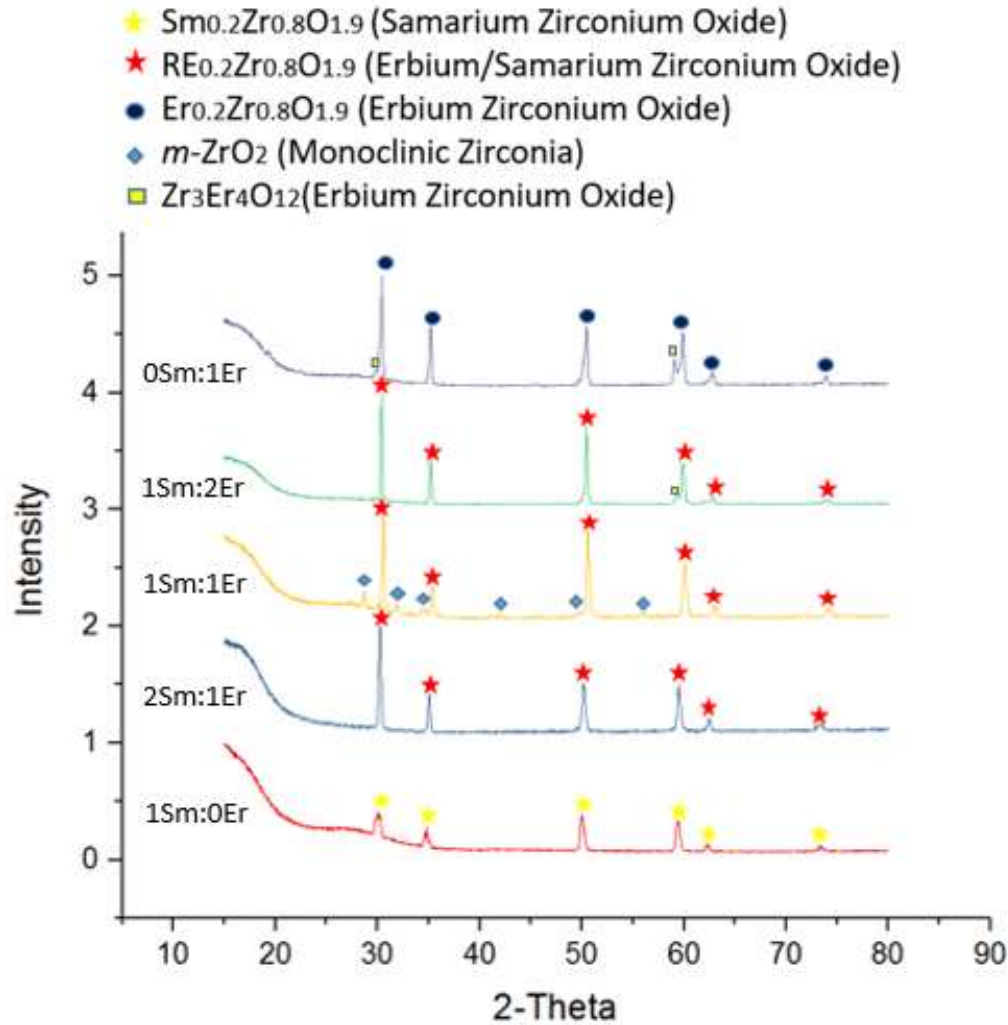


Figure 17. X-ray diffraction patterns of the surface after 300 s ablation cycle. This graph shows that  $c_I$ -(Sm/Er) $_{0.2}$ Zr $_{0.8}$ O $_{1.9}$  was the major phase with minor portions of  $m$ -ZrO $_2$ . The broad hump at lower  $2\theta$  shows the presence of the amorphous phase covering the surface.

A typical EDS line-scan of a sample ablated for 300 s is shown in Figure 18. For the 2Sm:1Er sample shown, the Sm and Er dopant concentration is much higher at the ablated surface ( $x=0\ \mu\text{m}$ ) than in deeper regions of the billet. The average Sm and Er concentration between  $x=0$ -75 $\mu\text{m}$  (within the oxide scale), as shown in Figure 18, is ~30 wt.% for Sm and ~20 wt.% for Er. The  $c_I$ -Sm $_{0.2}$ Zr $_{0.8}$ O $_{1.9}$  phase requires ~23 wt.% Sm to form, whereas the  $c_I$ -Er $_{0.2}$ Zr $_{0.8}$ O $_{1.9}$  phase requires ~20 wt.% Er to form. As the distance from the ablated surface is further increased, the average combined Sm and Er concentration between  $x=75$ -250  $\mu\text{m}$ , as shown in Figure 18, is ~16

wt.%. It is worth noting that the concentration difference between Sm and Er decreases as the distance from the ablated surface is increased. On the contrary, the Zr concentration is much lower at the ablated surface than in deeper regions of the billet. The average Zr concentration between  $x = 0 - 75 \mu\text{m}$  (within the oxide scale), as shown in Figure 18, is  $\sim 45$  wt.%. As the distance from the ablated surface is further increased, the average Zr concentration between  $x = 75 - 250 \mu\text{m}$  is  $\sim 75$  wt.%. Based on the EDS line-scan from Figure 18, it can be concluded that as the distance from the ablated surface is increased, the amount of the  $c_1\text{-(Sm/Er)}_{0.2}\text{Zr}_{0.8}\text{O}_{1.9}$  phase decreases, while the amount of the  $m\text{-ZrO}_2$  phase increases.

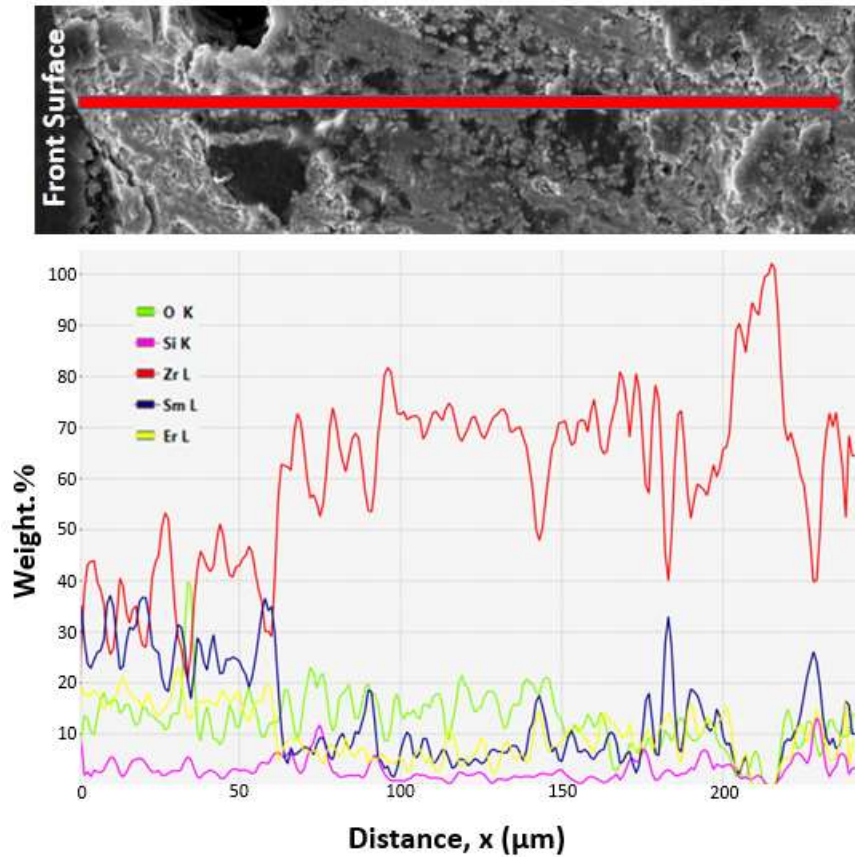


Figure 18. EDS line-scan for the 2Sm:1Er sample after 300 s ablation cycle and the wt.% concentration of major elements across the ablated billet thickness. It is shown that as the distance from the ablated surface is increased, the amount of the  $c_1\text{-(Sm/Er)}_{0.2}\text{Zr}_{0.8}\text{O}_{1.9}$  phase decreases, while the amount of the  $m\text{-ZrO}_2$  phase increases.

## 3.2 Discussion

### 3.2.1 First observation: The beneficial samarium/erbium zirconium oxide scale noted after ablation for 60 s and 300 s is formed by a convection cells mechanism

This study investigates the ablation properties of the oxide scales formed during ablation, when emittance modifiers of Sm and Er are added. The crystalline and amorphous phases observed in Figure 14 are being formed by a convection cell mechanism. These convection cells were noted by Karlsdottir et al.<sup>27</sup> for ZrB<sub>2</sub>/SiC coatings during oxidation at 1550 °C as a flower-like microstructure. The study describes the “islands” (center regions of the flower-like structure) to be *m*-ZrO<sub>2</sub>, the “petals” to be B<sub>2</sub>O<sub>3</sub> glass, and the “lagoon” regions to be SiO<sub>2</sub> glass.<sup>27</sup> The formation of the flower-like structure is caused by the viscous fingering phenomenon, which is the displacement of a less viscous liquid.<sup>25,27</sup> Due to the instability of the moving interface, the less viscous B<sub>2</sub>O<sub>3</sub> liquid displaces a more viscous SiO<sub>2</sub> liquid.<sup>25–27</sup> The rising B<sub>2</sub>O<sub>3</sub> rich liquid contains dissolved ZrO<sub>2</sub>, which deposits in the center of the flower-like structure when the B<sub>2</sub>O<sub>3</sub> evaporates. The liquid boria-rich oxidation product is transported through the overlying layer of SiO<sub>2</sub> liquid by convection, forming convection cells aligned like the petals of a flower.<sup>25–28</sup>

Brenner et al.<sup>24</sup> also noticed these convection cells during the oxidation of Sm-doped ZrB<sub>2</sub>/SiC coatings at ~1700 °C. Even though the convection cells mechanism during the ablation process in the present study was very similar to both Brenner et al.<sup>24</sup> and Karlsdottir et al.<sup>25,27,34</sup> studies, the final ablation product is different. The addition of Sm dopant to the ZrB<sub>2</sub>/SiC coatings in Brenner et al.<sup>24</sup> study formed a Sm-stabilized *t*-ZrO<sub>2</sub> phase after ablation, whereas the final product of Karlsdottir et al.<sup>25,27,34</sup> was *m*-ZrO<sub>2</sub>. Studies have shown that the B<sub>2</sub>O<sub>3</sub> glass present on the surface of a Sm-doped ZrB<sub>2</sub>/SiC coating after heating to 900 °C contains Sm<sup>3+</sup> atoms.<sup>9</sup> It was expected that the B<sub>2</sub>O<sub>3</sub> glass formed in the present study would not only contain Sm<sup>3+</sup> atoms but also Er<sup>3+</sup> atoms. This was confirmed by the SEM-EDS image shown in Figure 19a, where 31.0,

59.1, and 47.4 wt.% of Sm were detected in zones A-C, respectively, while Figure 19b shows that 71.0 and 51.0 wt.% of Er were detected in zones A-B, respectively. Because of the  $\text{Sm}^{3+}$  and  $\text{Er}^{3+}$  atoms being present in the rising  $\text{B}_2\text{O}_3$ -rich liquid containing dissolved  $\text{ZrO}_2$ , the final oxide scale product formed during the ablation testing will be different. This was confirmed by the XRD results of Figures 15 and 17, and the SEM-EDS of Figure 19a where the center region of the “flower-like” structure is composed of the crystalline  $cI\text{-Sm}_{0.2}\text{Zr}_{0.8}\text{O}_{1.9}$ , instead of the  $m\text{-ZrO}_2$  reported in the Karlsdottir et al.<sup>25,27,34</sup> studies or the Sm-stabilized  $t\text{-ZrO}_2$  phase in Brenner et al.<sup>24</sup> study.

The evaporation of  $\text{B}_2\text{O}_3$  glass would be expected as the maximum front surface temperatures were  $1690 \pm 20^\circ\text{C}$  and  $1717 \pm 21^\circ\text{C}$  during the 60s ablation tests for the 1Sm:0Er and 0Sm:1Er billets, respectively. Based on these surface temperatures it is also expected that much of the  $\text{SiO}_2$  glass would be evaporated, consistent with the small amounts of Si detected in the EDS results presented in Figure 19a-b.

Even though the powder preparation and the ablation test parameters used in the present study were the same than the ones used in the Brenner et al.<sup>35</sup> study, the resulted final oxide scale was different. This difference occurred because the alumina substrates in the Brenner et al.<sup>24</sup> study became part of the system by forming a blister after the ablation for 60s due to a local eutectic reaction occurring between  $\text{Sm}_2\text{O}_3$ ,  $\text{ZrO}_2$ , and  $\text{Al}_2\text{O}_3$ , and therefore, inhibited the formation of the  $cI\text{-Sm}_{0.2}\text{Zr}_{0.8}\text{O}_{1.9}$  reported for the 1Sm:0Er sample in the present study. If the problem of the alumina substrate becoming part of the system in the Brenner et al.<sup>24</sup> study is avoided, the  $cI\text{-Sm}_{0.2}\text{Zr}_{0.8}\text{O}_{1.9}$  oxide phase will be formed, consistent with Tan et al.<sup>4,9</sup> studies and the present study.



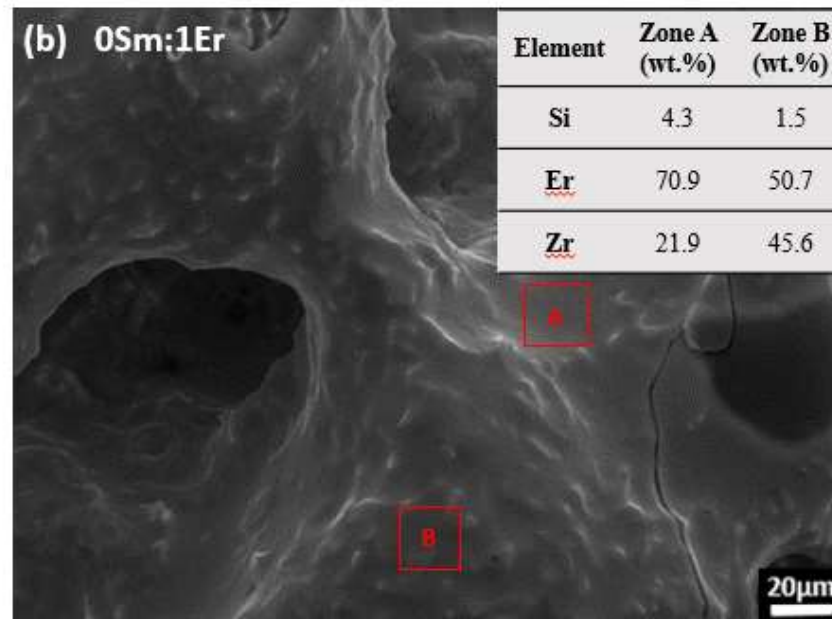
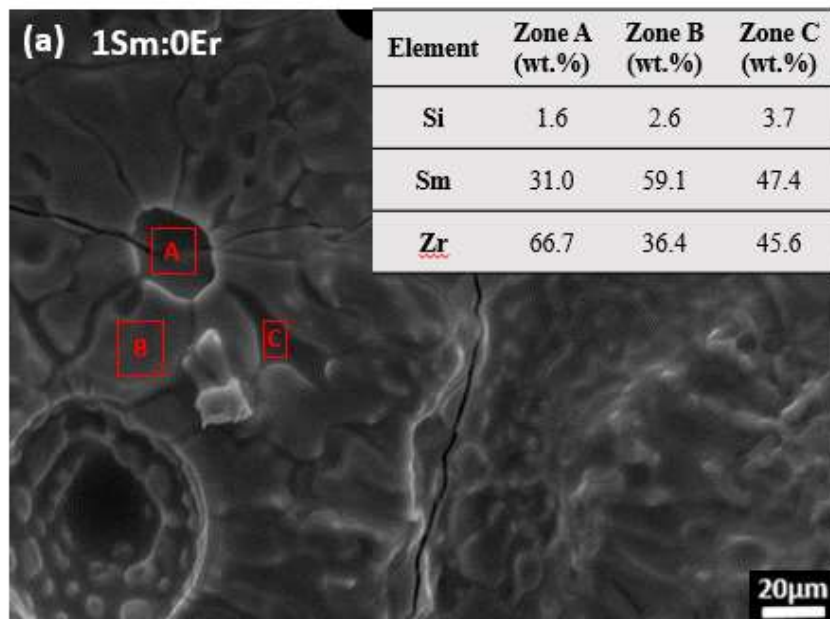


Figure 19. SEM-EDS for: a) micrograph of the flower-like microstructure on the 1Sm:0Er billet after the 60 s ablation cycle, b) micrograph of the 0Sm:1Er billet after the 60 s ablation cycle. This figure shows the presence of both Sm and Er in the surface of the samples ablated for 60 s.

The only difference in the XRD results between the samples ablated for 60 s and 300 s is the evidence of more glassy phase after longer ablation times, as observed by larger amorphous humps at lower values of  $2\theta$  for each of the Sm:Er billets investigated. The glassy phase seemed to be more evident as Er concentration increased. The increase in the amount of the glassy phase makes sense with the assertions in previous studies,<sup>9,25,36</sup> where the addition of rare-earth dopants to ZrB<sub>2</sub>/SiC billets modifies the tetrahedron structure of B<sub>2</sub>O<sub>3</sub> and SiO<sub>2</sub> resulting in the reduction of the viscosity of the glass and melting temperature. As the theoretical density of samarium oxide (7.62 g/cm<sup>3</sup>) is lower than erbium oxide (8.64 g/cm<sup>3</sup>), the viscosity should be reduced even more as the Sm concentration increases. This relationship between reduction of viscosity and increase of glassy phase is evident for the ablated billets after 300 s of this study. The increased glassy phase formed as the ablation time is increased from 60 s to 300 s is preventing conduction of heat away from the surface, resulting in an increase of the front surface temperature. Therefore, it is expected that this glassy phase might affect the emittance.

With increased time at high temperature, the glassy phase submerges the convection cells and they essentially disappear. Even though we cannot see the convection cells in the final microstructure after ablation, their effect on the final microstructure can be noted by the presence of  $c1\text{-(Sm/Er)}_{0.2}\text{Zr}_{0.8}\text{O}_{1.9}$  crystalline islands surrounded by a glassy phase. Occasionally remnants of the convection cells can be observed in the final microstructure. For example, a “flower-like” structure is noted in Figure 14a for the 1Sm:0Er sample. After ablation for 300 s, the  $c1\text{-(Sm/Er)}_{0.2}\text{Zr}_{0.8}\text{O}_{1.9}$  islands grow, coalesce, and inhibit the formation of petals by forming the crystalline grains shown in Figures 14g-i.<sup>25</sup>

Overall, the convection cell mechanism occurring in the present study is similar to both Karlsdottir et al.<sup>25,27,34</sup> and Brenner et al.<sup>24</sup> studies. However, significant differences are shown due

to the rare-earth dopants used in the present study, which cause the formation of different oxide scales during ablation testing. As the main purpose of doping the ZBS systems with emittance modifiers like Sm and Er is to form a  $c1\text{-(Sm/Er)}_{0.2}\text{Zr}_{0.8}\text{O}_{1.9}$  phase, the Sm-stabilized  $t\text{-ZrO}_2$  in the Brenner et al.<sup>24</sup> study and the  $m\text{-ZrO}_2$  in the Karlsdottir et al.<sup>25,27,34</sup> studies do not offer any improvement in modifying the emittance, and the  $\text{Sm}^{3+}$  ions role in the final microstructure is limited. The ability to increase the emittance by forming the  $c1\text{-Sm}_{0.2}\text{Zr}_{0.8}\text{O}_{1.9}$  instead of  $m\text{-ZrO}_2$  was confirmed in the Tan et al.<sup>9</sup> study by increasing the emittance up to 0.9 at 1600 °C for a coating constituted of 5 mol.% Sm with a balance of  $\text{ZrB}_2/\text{SiC}$ . Hence, it can be concluded that a similar  $c1\text{-(Sm/Er)}_{0.2}\text{Zr}_{0.8}\text{O}_{1.9}$  with different Sm:Er ratios will produce differences in the emittance. As a result, the  $c1\text{-(Sm/Er)}_{0.2}\text{Zr}_{0.8}\text{O}_{1.9}$  is a more desirable oxide product because it produces a potential tailorable emittance oxide scale, while forming a more stable and ablation resistance oxide scale than both the  $m\text{-ZrO}_2$  formed on Karlsdottir et al.<sup>25,27</sup> studies, and the Sm-stabilized  $t\text{-ZrO}_2$  on Brenner et al.<sup>24</sup> study. Furthermore, the  $c1\text{-Sm}_{0.2}\text{Zr}_{0.8}\text{O}_{1.9}$  has a melting point of 2700 °C for 3 mol.% of Sm dopant which is similar to the one of  $m\text{-ZrO}_2$ .<sup>9</sup>

Finally, the fact that the beneficial  $c1\text{-(Sm/Er)}_{0.2}\text{Zr}_{0.8}\text{O}_{1.9}$  provides a more dense oxide scale than the  $m\text{-ZrO}_2$  typically formed in ZBS systems, could help to address one of the most damaging factors to ZBS systems caused by the porous  $m\text{-ZrO}_2$  scale that does not provide any barrier to oxygen transport and tends to detach from the base alloy. Thence, the beneficial  $c1\text{-(Sm/Er)}_{0.2}\text{Zr}_{0.8}\text{O}_{1.9}$  oxide scale formed in the surface will reduce the amount of oxygen transported to deeper parts of the billet where the concentration of  $m\text{-ZrO}_2$  is higher, as showed by the EDS line-scan on Figure 18. This statement was also reported by Tan et al.<sup>9</sup> who showed that the  $c1\text{-Sm}_{0.2}\text{Zr}_{0.8}\text{O}_{1.9}$  oxide scale formed for ZBS coatings doped with 3 mol.% of Sm is more dense than  $m\text{-ZrO}_2$  formed for ZBS coatings.

### 3.2.2 Second observation: *Changes in the surface Sm and Er dopant concentration affects surface temperature measured.*

Despite the similarities of the convection cell mechanism in the billets prepared with five different Sm:Er molar ratios, the heating rates vary as can be observed by the difference in the inflection points in Figures 12 and 16. For example, Figure 12 shows that the inflection point temperature was the highest for the 0Sm:1Er sample at  $1600 \pm 19$  °C after ablation for 12 s, and the lowest for the 2Sm:1Er sample  $1300 \pm 16$  °C after ablation for 9 s. These differences in the inflection points can be explained by the different compositions of  $\text{Sm}^{3+}$  and  $\text{Er}^{3+}$  atoms in the billets, which change the emittance and the spectral absorptance of the oxide scales formed during ablation.

Changes in the emittance caused by using  $\text{Sm}^{3+}$  dopant have been shown in previous studies, which demonstrated that the emittance of  $\text{ZrO}_2$  can be increased via doping with rare-earths oxides that intentionally introduce defects into a pure material.<sup>9,32</sup> By comparing the ionic conductivity of the  $c1\text{-(Sm/Er)}_{0.2}\text{Zr}_{0.8}\text{O}_{1.9}$  phase formed in the present study with the  $m\text{-ZrO}_2$ , it is important to note that the ionic conductivity will increase for the  $c1\text{-(Sm/Er)}_{0.2}\text{Zr}_{0.8}\text{O}_{1.9}$  as the incorporated  $\text{Sm}^{3+}$  and  $\text{Er}^{3+}$  ions creates oxygen vacancies.<sup>9,32</sup> These oxygen vacancies provide transitions within the material band gap which modify the emittance.<sup>9,32</sup> Figure 18 shows that the amount of  $m\text{-ZrO}_2$  increases as the distance from the ablated surface is further increased. Based on that, the ionic conductivity should be higher in the ablated surface than in deeper regions of the billets.

Samarium oxide has demonstrated high emittance from visible to near IR wavelengths.<sup>13</sup> It is expected that the emittance will generally increase as the  $\text{Sm}^{3+}$  concentration is raised. Hence, increases in the heating rate may result from changes in emittance upon heating of such rare earth doped coatings. Previous evaluation of Sm-doped  $\text{ZrB}_2/\text{SiC}$  coatings<sup>9</sup> demonstrate that the  $\text{Sm}^{3+}$  atoms concentration is much higher at the ablated surface in comparison with  $\text{Sm}^{3+}$  atoms

concentration in the bulk. Figure 18 shows the rare-earth dopant concentration is much higher in the ablated surface than in the bulk. Therefore, it is expected that the concentration dependent emittance in the 2Sm:1Er billet will be higher than in the 1Sm:2Er sample. Thus, ultimate temperature observed is lower for Sm rich coatings and considerable inflection points in temperature are observed for Sm rich coatings in Figure 16.

On the other hand, it is well known that erbium oxide has demonstrated a low emittance in several wavelength ranges.<sup>13</sup> As the emittance for the current work was set to 0.9 on the pyrometer, the temperature would be underestimated if the emittance of the oxidized surface is lower at 1.55 $\mu$ m. Therefore, if the surface is reradiating less efficiently for a given temperature or becoming more absorptive at torch wavelengths, such coatings would heat more rapidly and/or achieve a higher ultimate temperature. After ablation for 60 s, it is shown that as the Er<sup>3+</sup> concentration is increased and the resulting  $C1-(\text{Sm/Er})_{0.2}\text{Zr}_{0.8}\text{O}_{1.9}$  oxide scale is more either absorptive at torch wavelengths and/or reradiating less efficiently, and therefore, achieving a higher surface temperature for Er rich billets. Also, in Figure 12, the maximum temperatures during the ablation cycle were the highest for the 0Sm:1Er and 1Sm:2Er samples; and the lowest for the 2Sm:1Er sample. However, this relation cannot be fully established as the ablation time is further increased from 60 s to 300 s. Figure 16 shows that maximum temperatures during the ablation cycle was the highest for the 1Sm:2Er sample, and lower for the 1Sm:0Er, 2Sm:1Er, 1Sm:1Er, and 0Sm:1Er samples. As can be noted by the results after ablation for 300 s, the maximum temperatures of the 1Sm:0Er, 2Sm:1Er, 1Sm:1Er, and 0Sm:1Er samples were very similar, and therefore, the benefit of being able to control the emittance and absorption properties by varying the Sm<sup>3+</sup> and Er<sup>3+</sup> concentration is not clear. As the only difference in the XRD results after ablation for 60 s and 300 s in Figures 15 and 17 is the evidence of more glassy phase after longer ablation times, as observed

by larger amorphous humps at lower values of  $2\theta$ , it is evident that the increase in glassy phase is inhibiting the beneficial effects of increasing the emittance as the  $\text{Sm}^{3+}$  concentration is increased from 0-2.94 mol%. A possible solution to avoid this problem and maximize the beneficial effects of tailoring the emittance at these higher temperatures shown by Figure 16 is to increase the total dopant(s) concentration incorporated into the sample from 3 mol.% to 5 mol.%, as in Tan et al.<sup>9</sup> study.

### 3.3 Conclusions

Sintered  $\text{ZrB}_2/\text{SiC}$  billets co-doped with Sm and Er atoms in five different ratios were prepared. These samples were evaluated via ablation testing for 60 s and 300 s using an oxyacetylene torch. The phase assemblage and microstructure of the surface were evaluated after each ablation time. ZBS billets co-doped with Sm and Er forms a potential tailorable emittance  $c_{I-}(\text{Sm/Er})_{0.2}\text{Zr}_{0.8}\text{O}_{1.9}$  oxide scale as the major phase, which provides a more stable oxide scale than the  $m\text{-ZrO}_2$  oxide scale formed in ZBS systems. The crystalline oxide scale and amorphous phases form by a convection cells mechanism where the  $c_{I-}(\text{Sm/Er})_{0.2}\text{Zr}_{0.8}\text{O}_{1.9}$  crystalline islands precipitate, grow and coalesce. Changes in the surface Sm and Er dopant concentration affects surface temperature measured, due to changes in spectral emittance upon heating.

#### 4. EVALUATION OF RARE-EARTH ELEMENT DOPANTS (SAMARIUM AND ERBIUM) ON THE EMITTANCE TAILORING OF ZIRCONIUM DIBORIDE/SILICON CARBIDE SINTERED BILLETS

Understanding and modifying the emittance of ultra-high temperature ceramics (UHTCs) is important for a wide range of applications, including hypersonic flight. How rare-earth dopant elements (samarium and erbium) affect the radiation properties of sintered  $\text{ZrB}_2\text{-SiC}$  (ZBS) samples during emittance testing is evaluated in the current work. ZBS billets with five different Sm to Er molar ratios, with a nominal total amount of 3 mol.% dopant incorporated, were prepared by sintering in vacuum to 2000 °C. These samples were subject to laser heating for times up to 80 s in air, with temperatures reaching 2250 °C. ZBS billets co-doped with Sm and Er formed  $m\text{-ZrO}_2$  as the major phase with minor portions of the beneficial  $c1\text{-(Sm/Er)}_{0.2}\text{Zr}_{0.8}\text{O}_{1.9}$  oxide scale during their exposure to the laser heating process. As the  $m\text{-ZrO}_2$  was formed as the major phase instead of the  $c1\text{-(Sm/Er)}_{0.2}\text{Zr}_{0.8}\text{O}_{1.9}$ , the emittance profiles of all the five Sm:Er molar ratios were very similar as function of wavelength and temperature. However, the maximum and minimum emittance peaks differences caused by varying the  $\text{Er}_2\text{O}_3$  molar concentration from 0 to 3.11 mol.%, suggest that the emittance profiles of ZBS sintered billets co-coped with Sm and Er can be potentially tailored due to changes in the spectral absorbance and emittance.

##### 4.1 Data Conversion Process: *Spectral Radiance to Emittance*

Planck's law represents the spectral distribution of blackbody emission ( $L_\lambda$ ) at temperature  $T_b$  as a function of wavelength ( $\lambda$ ), first radiation constant ( $c_1=1.1910439 \times 10^{-16} \text{ W.m}^2$ ), and second radiation constant ( $c_2=0.014388 \text{ m.K}$ ).<sup>37</sup>

$$L_\lambda = \frac{c_1}{\lambda^5 \left[ \exp\left(\frac{c_2}{\lambda T_b}\right) - 1 \right]} \quad (8)$$

There are three main aspects from Plank's distribution equation that should be noted. First, the emitted spectral radiance increases with increasing temperature. Second, at any wavelength the value of the emitted spectral radiance increases with increasing temperature. Third, as defined by the Wien's displacement law, the spectral zone in which the spectral radiance is concentrated will be located at shorter wavelengths as the temperature increases.<sup>38</sup>

To perform surface temperature and emittance calculations, a MATLAB algorithm was developed to average and calibrate a set of blackbody data. This algorithm relates the measured spectral radiance signal from the testing equipment to the blackbody sample temperature, performs a blackbody calibration, and subsequently calculates the actual temperature and emittance data. The calibration function was defined using the Planckian form of the Sakuma-Hatori equation, which is a non-linear regression method.<sup>11,39-46</sup> The advantages of this equation are that it approximates Planck's law integrated over a spectral band and it can be easily inverted to solve for both temperature and emittance. The Planckian form of the Sakuma-Hatori equation for a blackbody temperature is provided by equation 2 as a function of the wavelength over defined temperature ranges, the second radiation constant ( $c_2$ ); and the constants A, B and C.

$$T = \frac{c_2}{A \ln\left(\frac{C}{L\lambda}\right)} - \frac{B}{A} \quad (9)$$

Every wavelength has a unique value of A, B, C,  $L_\lambda$ , and  $\epsilon$ , but the actual temperature is the same across all wavelengths. As a result, for each spectral radiance versus wavelength profile, four unknowns need to be calculated (B, C, T, and  $\epsilon$ ). The coefficients in equation 2 were obtained using the following assumptions: (1) the coefficient A is constrained to be the wavelength ( $\lambda$ ), and (2) the coefficients B and C are not temperature dependent. The coefficients B and C are an offset and a gain, respectively. Moreover, they were obtained from the calibration data, and have been determined according to what calibration is required for the blackbody data to agree with the



theoretical Planckian curves. It must be noted that each calculation requires a set of four Sakuma-Hatorri equations to solve for the B and C coefficient values.

Four blackbody temperatures across the range of interest were calculated to solve for the unknown Sakuma-Hatorri coefficients (B and C) and calibrate the data. To solve for these four unknown blackbody temperatures, a set of four Sakuma-Hatorri equations was used with a constant wavelength  $\lambda_n$  at the four different unknown blackbody temperatures. In other words, for  $n=1, 2, 3 \dots 254$ , a set of four Sakuma-Hatorri equations [ $L_\lambda(\lambda_n, T_{b1})$ ,  $L_\lambda(\lambda_n, T_{b2})$ ,  $L_\lambda(\lambda_n, T_{b3})$  and  $L_\lambda(\lambda_n, T_{b4})$ ] were used to solve the four unknown blackbody temperatures at each wavelength. As the blackbody temperature must be the same across the 1500-5000 nm wavelength range, the four average blackbody temperatures calculated were 1207 °C, 1368 °C, 1501 °C, and 1657 °C.

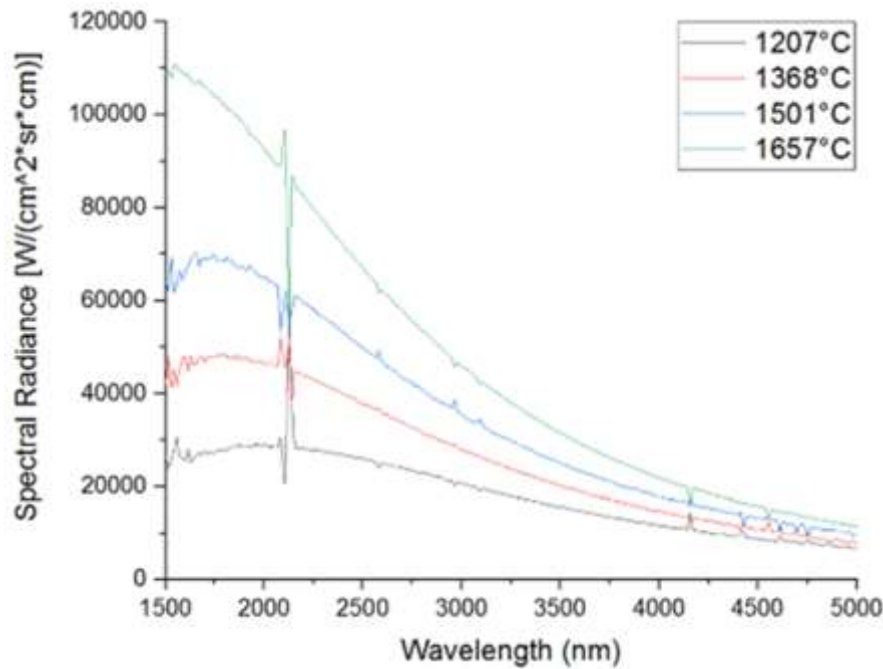


Figure 20. Blackbody calibration at the four chosen temperatures of interest using the Planckian form of the Sakuma-Hatorri equation.

After calculating the four blackbody temperatures that represent the temperature range of interest, there is a curve fitting process using the Sakuma-Hatori relationship to calibrate and approximate the actual spectral radiance signal measured. This is shown in Figure 1, where the four spectral radiance versus wavelength distributions at the calculated blackbody temperatures were calibrated by the Sakuma-Hatori function described by equation (2).

Figure 21 shows that the value of coefficient B keeps mainly constant across the wavelength range 1500-5000 nm. On the other hand, Figure 21 shows that the coefficient C value decrease as the wavelength increases. After calculating the two unknown coefficients (B and C), the real temperature profiles were obtained by multiplying equation 2 by the emittance term ( $\epsilon$ ) powered to -0.25, as shown in equation 3.

$$T = [\epsilon^{-1/4}] * \left[ \frac{c^2}{A * \ln\left(\frac{C}{L\lambda}\right)} - \frac{B}{A} \right] \quad (10)$$

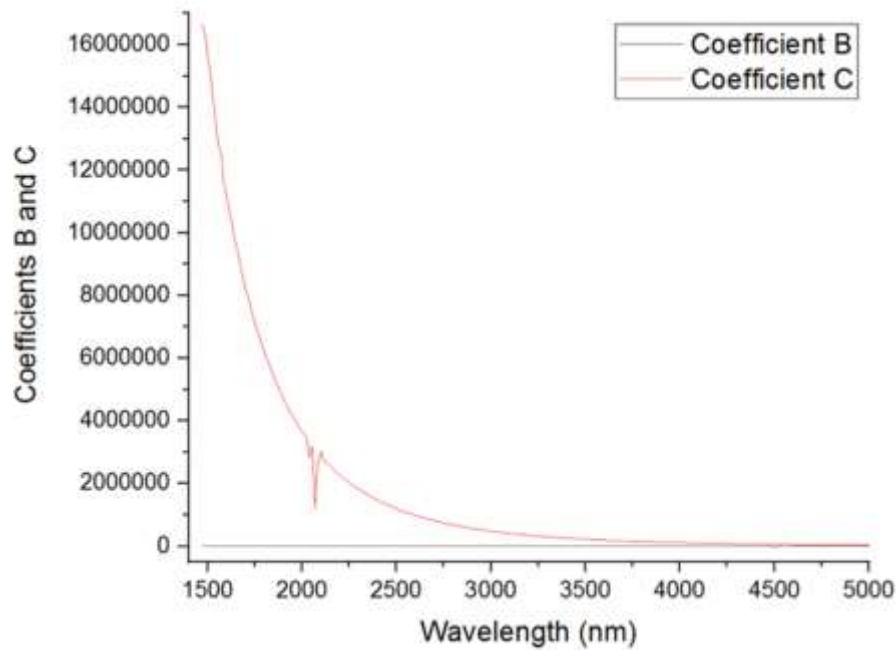


Figure 21. Coefficients B and C versus wavelength from 1500-5000 nm. This graph shows that the coefficient C exponentially decreases by increasing the wavelength, whereas the coefficient B remains constant by increasing the wavelength.

To calculate the real temperatures, an initial emittance value was assumed across a narrow wavelength range where the data is smooth. As the data is smooth in that range, it can be assumed that it behaves as a graybody, and therefore, the emittance is constant and allows calculating the real temperatures. The initial emittance assumption of 0.3 was based on the theoretical data obtained from previous studies for  $m\text{-ZrO}_2$ .<sup>13</sup> After calculating the real temperatures, the equation 3 was solved for the emittance values for wavelength ranges from 1500-5000 nm.

## **4.2 Results**

### **4.2.1 Microstructural and Phase Analysis Results after Laser Heating**

Figures 22a-o compare the back-face surfaces after the 80 s of laser heating. The back-face surface represents the side where the samples were heated by the laser. Each of the Sm:Er billets developed an adherent oxide scale on the laser-side. The oxide scale color changed relative to the amount of Sm and Er dopant from yellow in the 1Sm:0Er sample to pink in the 0Sm:1Er sample. It can be seen in Figure 22 that the amount of glassy phase increases as the laser power is increased due to the higher temperature achieved. Also, Figure 22 shows that cracks were formed in all the samples due to the thermal shock caused by rapid laser heating.

Figures 23a-o compare the front-face surfaces after 80 s of laser heating. The front-face surface represents the side where the spectral radiance data was collected by the spectrometer. Each of the Sm:Er billets developed an adherent oxide scale on the laser-side. As can be noted on Figure 23, the glassy phase amount is much lower than in Figure 22 due to the lower surface temperatures reached.

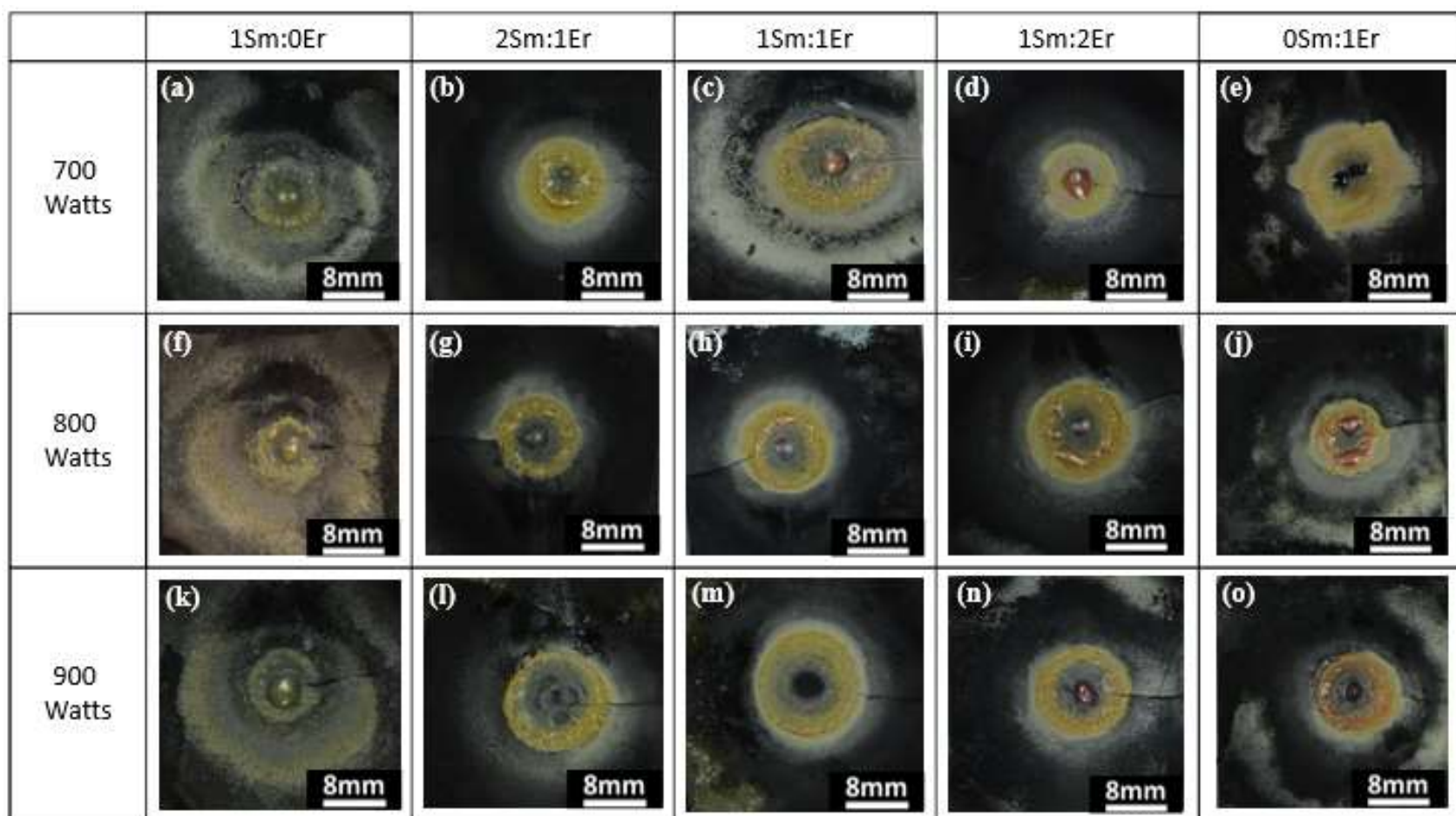


Figure 22. Optical images of the back-side of the billets (laser-side) for the following billets: a) 1Sm:0Er, b) 2Sm:1Er, c) 1Sm:1Er, d) 1Sm:2Er, and e) 0Sm:1Er at 700 Watts; f) 1Sm:0Er, g) 2Sm:1Er, h) 1Sm:1Er, i) 1Sm:2Er, and j) 0Sm:1Er at 800 Watts; and k) 1Sm:0Er, l) 2Sm:1Er, m) 1Sm:1Er, n) 1Sm:2Er, and o) 0Sm:1Er at 900 Watts. This figure shows the presence of a glassy phase in the center of the samples and cracks caused by thermal shock.

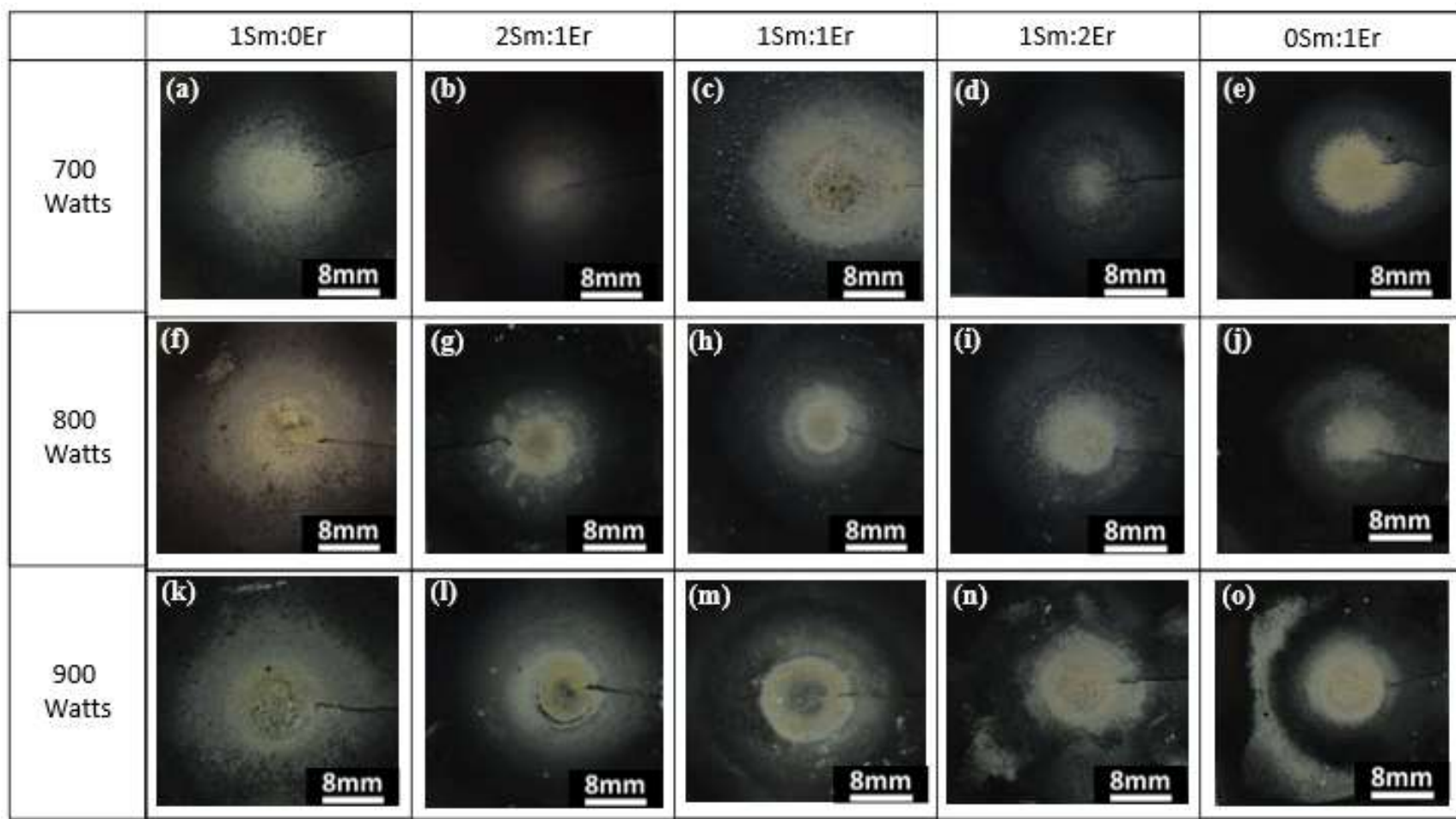


Figure 23. Optical images of the front side of the billets (spectrometer-side where the data was collected) for the following billets: a) 1Sm:0Er, b) 2Sm:1Er, c) 1Sm:1Er, d) 1Sm:2Er, and e) 0Sm:1Er at 700 Watts; f) 1Sm:0Er, g) 2Sm:1Er, h) 1Sm:1Er, i) 1Sm:2Er, and j) 0Sm:1Er at 800 Watts; and k) 1Sm:0Er, l) 2Sm:1Er, m) 1Sm:1Er, n) 1Sm:2Er, and o) 0Sm:1Er at 900 Watts. This figure shows that the spectrometer-side reached a lower temperature than the laser-side.

The XRD results on the spectrometer measurement side after the laser heating test for the 1Sm:0Er samples, presented in Figure 24, show that the major phase formed was monoclinic zirconia ( $m\text{-ZrO}_2$ , JCPDS-00-37-1484) with small portions of the cubic samarium zirconium oxide scale ( $c_1\text{-Sm}_{0.2}\text{Zr}_{0.8}\text{O}_{1.9}$ , JCPDS-01-78-1302),  $\text{Sm}_2\text{O}_3$  and  $\text{ZrB}_2$ . For the 2Sm:1Er, 1Sm:1Er, and 1Sm:2Er billet samples, the XRD results also show a similar  $m\text{-ZrO}_2$  as the major phase with small amounts of a similar cubic structure ( $c_1\text{-(Sm/Er)}_{0.2}\text{Zr}_{0.8}\text{O}_{1.9}$ ),  $\text{SiO}_2$ ,  $(\text{Sm/Er})_2\text{O}_3$  and  $\text{ZrB}_2$ . The  $c_1\text{-(Sm/Er)}_{0.2}\text{Zr}_{0.8}\text{O}_{1.9}$  and the  $(\text{Sm/Er})_2\text{O}_3$  phases are formed due to the Sm and Er atoms exchanging positions because of their similar ionic size (242 pm for Sm and 236 pm for Er). The primary peaks were shifted to larger  $2\theta$  due to the smaller interplanar spacing caused by the slightly smaller erbium atoms. It is shown that as the Er mol.% concentration is increased, the peak intensity for the  $c_1\text{-(Sm/Er)}_{0.2}\text{Zr}_{0.8}\text{O}_{1.9}$  phase increases, suggesting that the Er dopant is having a bigger effect in the final oxide scale than the Sm dopant. It is evident in the 0Sm:1Er sample, where the major oxide phase was the cubic erbium zirconium oxide ( $c_1\text{-Er}_{0.2}\text{Zr}_{0.8}\text{O}_{1.9}$ ) with small amounts of  $m\text{-ZrO}_2$ ,  $\text{SiO}_2$ ,  $\text{Er}_2\text{O}_3$  and  $\text{ZrB}_2$ .

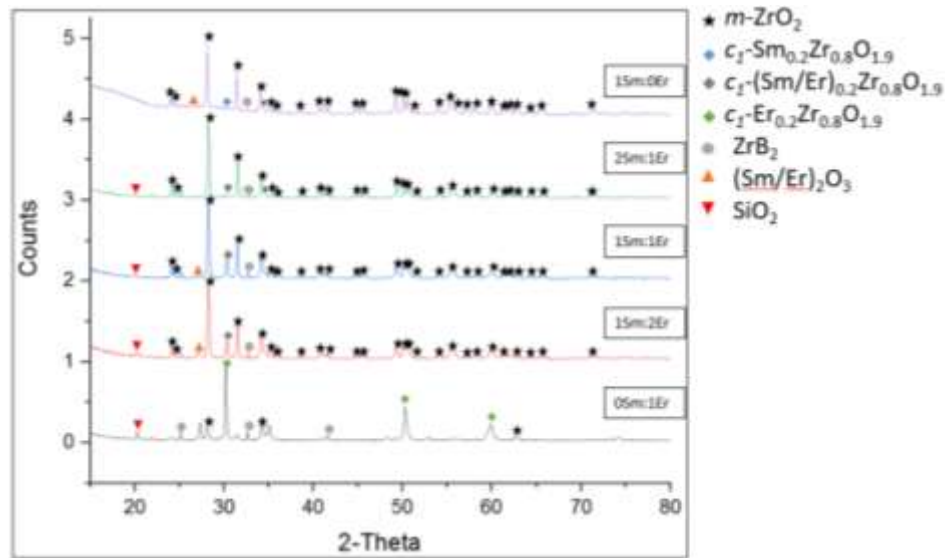


Figure 24. XRD patterns of the surface on the spectrometer side. This graph shows that  $m\text{-ZrO}_2$  was the major phase in most of the samples with small portions of  $c_1\text{-(Sm/Er)}_{0.2}\text{Zr}_{0.8}\text{O}_{1.9}$ ,  $\text{SiO}_2$ ,  $\text{ZrB}_2$ , and  $(\text{Sm/Er})_2\text{O}_3$ .

Figures 25a-o compare SEM micrographs of the spectrometer-side surface after laser heating for 80 s. For all five Sm:Er molar ratios exposed to a laser heating power of 700 W, Figure 25a-e, the surface appears to have clusters of crystalline islands surrounded by an amorphous phase. Figures 25k-o show that as the power is further increased to 900 W, the amount of glassy phase decreases whereas the porosity increases. The increase in the final porosity of the samples is caused by the evaporation of CO, CO<sub>2</sub>, and the glassy B<sub>2</sub>O<sub>3</sub> and SiO<sub>2</sub> oxide products.<sup>4,25,34</sup>



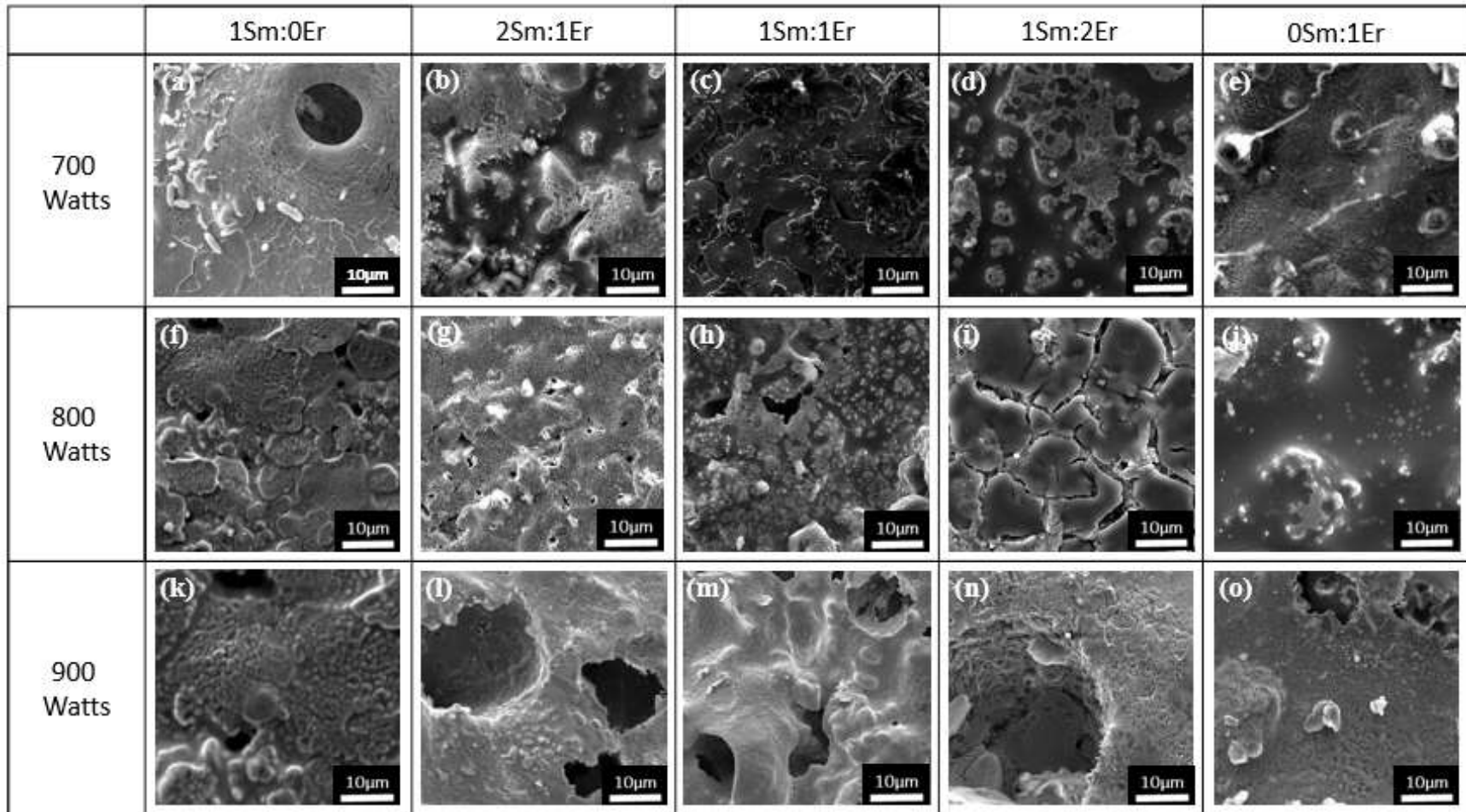


Figure 25. SEM micrographs after the laser heating for 120 s for the following billets: a) 1Sm:0Er, b) 2Sm:1Er, c) 1Sm:1Er, d) 1Sm:2Er, and e) 0Sm:1Er at 700 W; f) 1Sm:0Er, g) 2Sm:1Er, h) 1Sm:1Er, i) 1Sm:2Er, and j) 0Sm:1Er at 800 W; and k) 1Sm:0Er, l) 2Sm:1Er, m) 1Sm:1Er, n) 1Sm:2Er, and o) 0Sm:1Er at 900 W. This figure shows that as the power is increased, the glassy phase decreases, and therefore, the amount of porosity increases.



An EDS line-scan for the 2Sm:1Er, 1Sm:1Er and 0Sm:1Er samples after laser heating for 80 s is shown in Figures 26a-c. The thickness of the oxide scale for the three samples is  $\sim 60\ \mu\text{m}$ . Additionally, the oxygen content is higher within this scale ( $x=0\text{-}60\ \mu\text{m}$ ) reaching values up to 50 wt.%, than compared with deeper regions of the billets ( $x=60\text{-}240\ \mu\text{m}$ ). It makes sense that the oxygen content is higher within the oxide scale as the spectrometer-side is exposed to the air. Despite the temperature was higher in deeper regions of the billets ( $x=60\text{-}240\ \mu\text{m}$ ), this area was not oxidized to  $m\text{-ZrO}_2$  due to the lower oxygen content caused by the longer diffusion path. A possible explanation is that the glass flow acted as a barrier which prevented further oxidation in the unreacted deeper parts of the billets, as shown by the evidence of Si in all the three samples in Figures 26a-c. The Si content within the oxide scale ( $x=0\text{-}60\ \mu\text{m}$ ) is higher as the Er mol.% increases, evidenced by the  $\sim 4$  wt.%,  $\sim 19$  wt.% and  $\sim 33$  wt.% of Si in the 2Sm:1Er, 1Sm:1Er and 0Sm:1Er samples respectively.

Furthermore, Figures 26a-c show that the Sm and Er concentrations are lower within the oxide scale ( $x=0\text{-}30\ \mu\text{m}$ ) than in deeper regions of the billets ( $x=60\text{-}240\ \mu\text{m}$ ) for the three samples. The average combined Sm and Er concentration within the oxide scale ( $x=0\text{-}30\ \mu\text{m}$ ) is  $\sim 18$  wt.% for the 2Sm:1Er sample, and  $\sim 14$  wt.% for the 1Sm:1Er sample. The  $c1\text{-Sm}_{0.2}\text{Zr}_{0.8}\text{O}_{1.9}$  phase requires  $\sim 23$  wt.% Sm to be formed, whereas the  $c1\text{-Er}_{0.2}\text{Zr}_{0.8}\text{O}_{1.9}$  phase requires  $\sim 20$  wt.% Er. As a result, just small portions of the beneficial  $c1\text{-(Sm/Er)}_{0.2}\text{Zr}_{0.8}\text{O}_{1.9}$  were formed, whereas  $m\text{-ZrO}_2$  was the major phase as shown in the XRD results shown in Figure 24. On the contrary, the average Er concentration within the oxide scale ( $x=0\text{-}30\ \mu\text{m}$ ) for the 0Sm:1Er sample was  $\sim 20$  wt.%, and the  $c1\text{-Er}_{0.2}\text{Zr}_{0.8}\text{O}_{1.9}$  was formed as the major oxide scale. The EDS line-scan on Figure 26 allows to conclude that the Sm and Er concentration rises as the distance from the spectrometer-side surface ( $x=0\ \mu\text{m}$ ) is increased. Therefore,  $m\text{-ZrO}_2$  is formed as the major phase with small portions

of the  $c_1\text{-(Sm/Er)}_{0.2}\text{Zr}_{0.8}\text{O}_{1.9}$  phase for the 2Sm:1Er and 1Sm:1Er samples. However, as the Er mol.% is increased, the amount of the  $c_1\text{-(Sm/Er)}_{0.2}\text{Zr}_{0.8}\text{O}_{1.9}$  phase also increases until it becomes the major oxide phase as it is shown by the 0Sm:1Er sample.

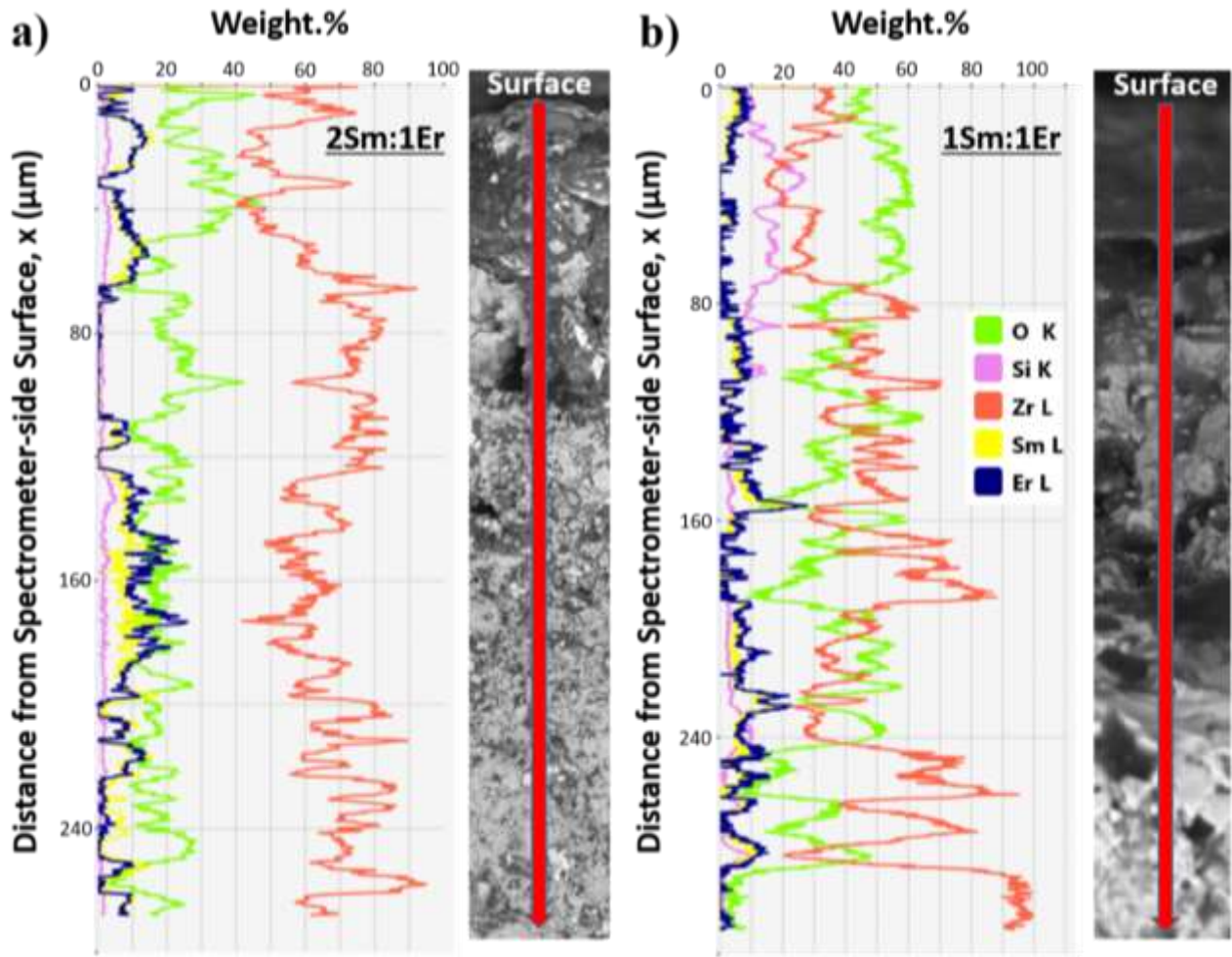
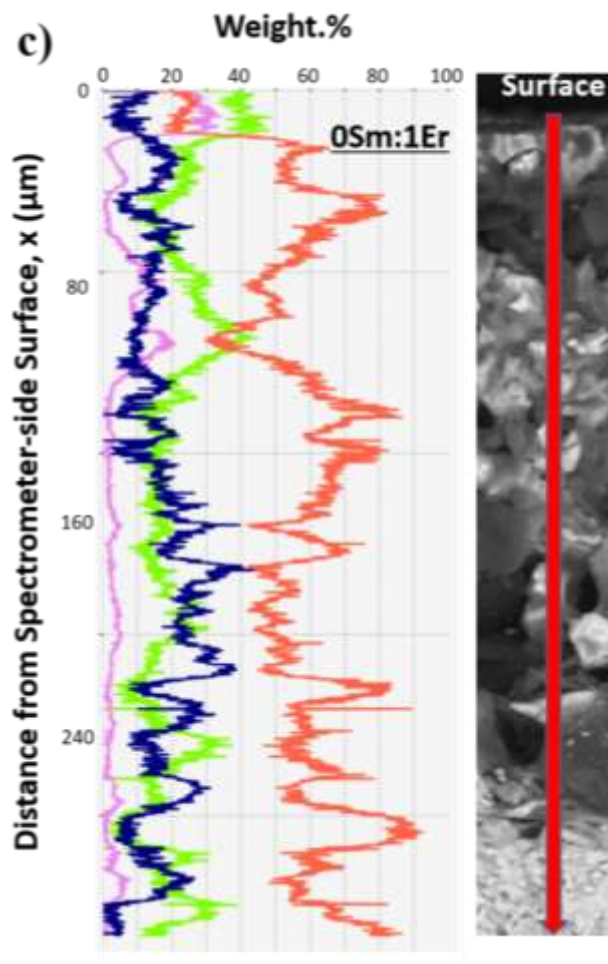


Figure 26. EDS line-scan after 80 s of laser heating at 800 Watts for the following billets: (a) 2Sm:1Er, (b) 1Sm:1Er, and (c) 0Sm:1Er. This figure shows that the Sm and Er concentration rises as the distance from the spectrometer-side surface ( $x=0\text{ }\mu\text{m}$ ) is increased. Therefore,  $m\text{-ZrO}_2$  is formed as the major phase with small portions of the  $c_1\text{-(Sm/Er)}_{0.2}\text{Zr}_{0.8}\text{O}_{1.9}$  phase.

Figure 26 continued



#### 4.3 4.2.2 Emittance Profiles after Laser Heating

Figure 27 shows the spectrometer-side temperature versus time comparison for the five different Sm:Er molar ratios tested at 800 W during the 80 s emittance testing. All of them displayed a continuous temperature increase through the 80 s of laser heating with a rapid increase in temperature for the first ~20 s until a maximum value was reached, followed by a very slow decrease in temperature for the next ~40 s, and lastly, a rapid decrease in temperature for the final ~20 s after the applied power is turned off. The 1Sm:2Er sample showed the highest temperature. The 1Sm:0Er sample showed the lowest temperature from ~20-32 s, whereas the 0Sm:1Er sample

showed the lowest temperature from 33-60 s. For this temperature versus time graph, an initial emittance assumption of 0.3 was used over the 3500-3900 nm range. The accuracy of the initial emittance assumption of 0.3 on the spectrometer-side temperature was evaluated by calculating the percent of difference and the standard error if the emittance varies by  $\pm 0.1$  and  $\pm 0.2$  from the 0.3 value initially assumed. The average percent of difference in the spectrometer-side temperatures calculated over a time range of 120 s were  $8.85 \pm 0.06$  if the emittance varies by  $\pm 0.1$ , and  $16.35 \pm 0.12$  if the emittance varies by  $\pm 0.2$ . In other words, the average temperature difference is  $136 \pm 5$  °C if the emittance varies by  $\pm 0.1$ , and  $235 \pm 9$  °C if the emittance varies by  $\pm 0.2$ . The average percent of difference and the average temperature difference were calculated under their 95% confidence interval.

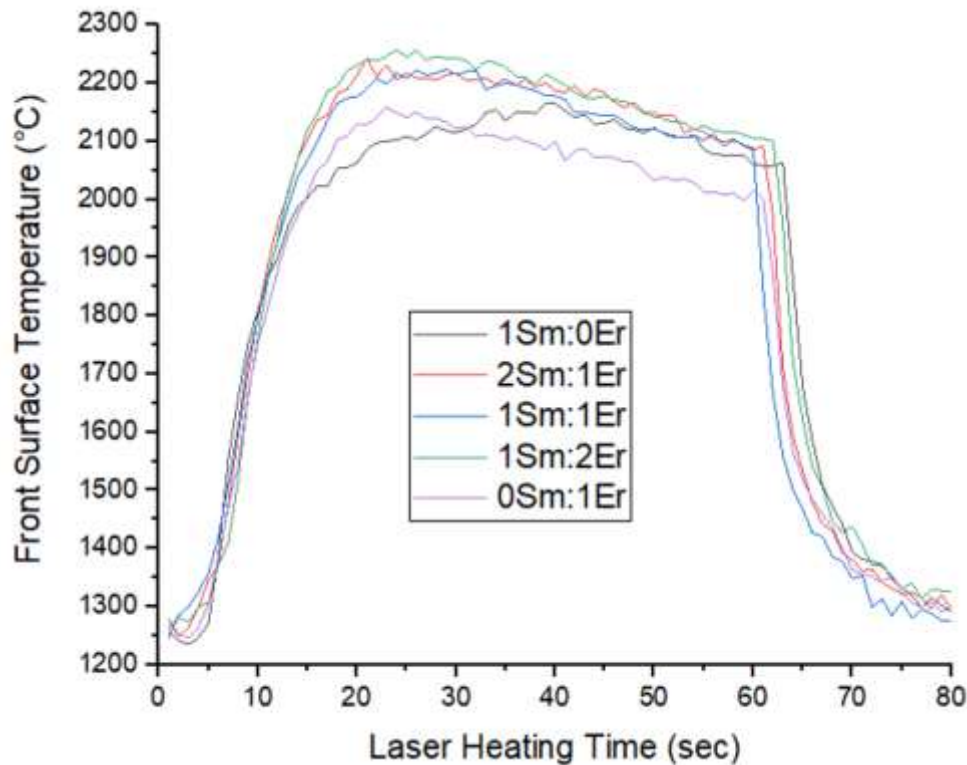


Figure 27. Temperature versus time comparison for the five different Sm:Er ratios tested at 800 W for 80 s. This figure shows that the Sm and Er concentration produces changes in the front surface temperatures.

Figures 28a-b show the emittance versus wavelength profiles for the 1Sm:0Er and 0Sm:1Er samples from 1500-3000 nm for the following temperatures: 1600 °C, 1700 °C, 1800 °C, 1900 °C, 2000 °C, and 2100 °C. For the 1Sm:0Er and 0Sm:1Er samples, the emittance profile at 2200 °C is not presented because these two samples did not reach that temperature. The emittance profiles for both the 1Sm:0Er and 0Sm:1Er samples as a function of temperature are basically equivalent. For the 1Sm:0Er sample, Figure 28a shows that the only emittance differences greater than 0.10 as a function of temperature (1600-2100 °C) occurred at the following wavelength bands: 1501 nm by 0.15, 1515 nm by 0.10, 2069 nm by 0.25, and 2112 nm by 0.10 (Points A-D); whereas Figure 28b shows that for the 0Sm:1Er sample it occurred at: 1501 nm by 0.14, 1529 nm by 0.14, 2069 nm by 0.26, and 2112 nm by 0.10 (Points E-H). In general, Figures 28a-b show that the emittance slightly decreases by increasing temperature from 1600 °C to 2100 °C at shorter wavelengths, but as the wavelength is further increased, the emittance remains mainly constant.

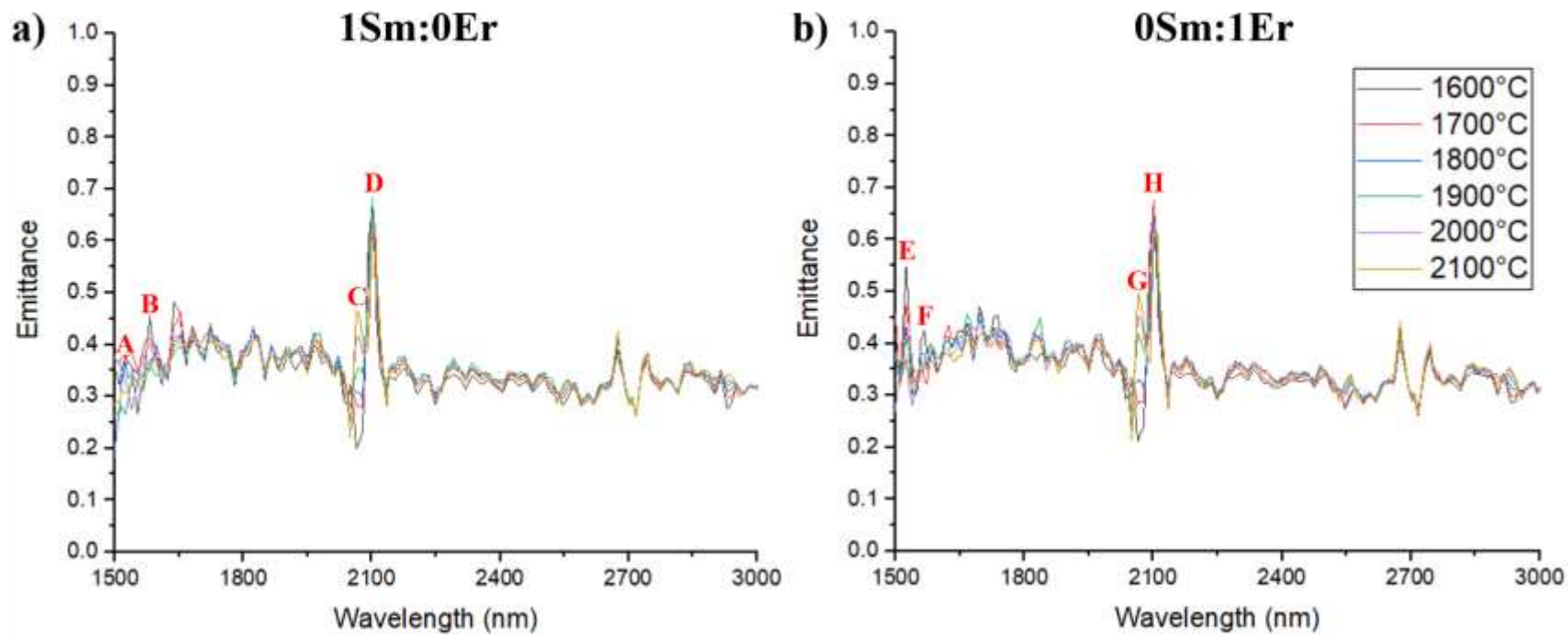


Figure 28. Emittance versus wavelength profiles at 1600 °C, 1700 °C and 1800 °C, 1900 °C, 2000 °C, and 2100 °C from 1500-3000 nm for the following billets: (a) 1Sm:0Er, and (b) 0Sm:1Er. These two graphs show the presence of maximum emittance peaks (Points A-H). The emittance profiles for both samples is similar and remain constant as the temperature increases.

Figures 29a-c show the emittance versus wavelength profiles from 1500-3000 nm as a function of temperature for the 2Sm:1Er, 1Sm:1Er, and 1Sm:2Er samples. The temperatures used to measure the emittance profiles were: 1600 °C, 1700 °C, 1800 °C, 1900 °C, 2000 °C, 2100 °C and 2200 °C. For the 2Sm:1Er sample, it is shown that the emittance slightly decreases as the temperature increases from 1600 °C to 2100 °C at shorter wavelengths, but as the wavelength increases the emittance slightly increases by increasing the temperature. Also, Figure 29a shows that for the 2Sm:1Er billet the only emittance differences higher than 0.10 as a function of temperature (1600-2200 °C) occurred at the following wavelength bands: 1501 nm by 0.17, 1515 nm by 0.17, 1529 nm by 0.25 (Point A), 1544 nm by 0.24 (Point B), 1558 nm by 0.17, 1572 nm by 0.15, 1586 nm by 0.11, 1657 nm by 0.10 (Point C), 2069 nm by 0.28 (Point D), and 2112 nm by 0.14 (Point E). In addition, for the 2Sm:1Er sample, at the emittance peaks located at 1529 nm, 1544 nm and 1657 nm, the emittance decreases as the temperature increases; whereas for the emittance peaks located at 2069 nm and 2112 nm (Points D and E) the emittance increases by increasing the temperature. Like the 2Sm:1Er sample, Figure 29b shows that for the 1Sm:1Er billet the emittance slightly decreases as the temperature increases from 1600 °C to 2100 °C at shorter wavelengths, but as the wavelength increases the emittance slightly increases by increasing the temperature. Figure 29b shows that for the 1Sm:1Er billet, the only emittance differences higher than 0.10 as a function of temperature (1600-2200 °C) occurred at the following wavelength bands: 1501 nm by 0.15, 1515 nm by 0.10, 1529 nm by 0.13, 1544 nm by 0.12, 1558 nm by 0.11, 2069 nm by 0.36 (Point F), and 2112 nm by 0.12 (Point G). Also, for the 1Sm:1Er sample, at the emittance peaks located at 2069 nm and 2112 nm (Points F and G) the emittance increases by increasing the temperature. Finally, for the 1Sm:2Er sample, Figure 29c shows a higher emittance decrease than the 2Sm:1Er and 1Sm:1Er samples as the temperature increases from 1600 °C to

2100 °C at shorter wavelengths. As the wavelength increases the emittance increases by increasing the temperature. Contrary to the 2Sm:1Er and 1Sm:1Er samples, Figure 29c shows that for the 2Sm:1Er billet the emittance differences higher than 0.10 as a function of temperature (1600-2200 °C) occurred in a lot of wavelengths bands as can be noted at the wavelength range from 1501-1714 nm by 0.10-0.44, at 2069 nm by 0.40, at 2112 nm by 0.16, and at 2935 nm by 0.11. Also, for the 1Sm:2Er sample, at the emittance peaks located at 1529 nm (Point H), 1544 nm and (Point I), the emittance decreases as the temperature increases; whereas for the emittance peaks located at 2069 nm and 2112 nm (Points L and M) the emittance increases by increasing the temperature.

Figures 29a-c clearly show that as the incorporated Er concentration is increased, from 1.23 mol.% in the 2Sm:1Er sample to 2.33 mol.% in the 1Sm:2Er sample, the emittance increases at the shorter wavelength range (1500-1800 nm). Also, the emittance variation with temperature from 1500-1800 nm increases as the Er mol.% increases. It can be noted in the initial wavelength band at 1501 nm and 2100 °C where the emittance values are: 0.35 for the 2Sm:1Er sample, 0.34 for the 1Sm:1Er sample, and 0.52 for the 1Sm:2Er sample. As the temperature is decreased to 1600 °C, however, the Figures 8a-c show higher emittance values at 1501 nm: 0.51 for the 2Sm:1Er sample, 0.45 for the 1Sm:1Er sample, and 0.86 for the 1Sm:2Er sample.

Figures 30a-b show the emittance versus wavelength profiles for the 1Sm:0Er and 0Sm:1Er samples from 3000-4500 nm at the following temperatures: 1600 °C, 1700 °C, 1800 °C, 1900 °C, 2000 °C, and 2100 °C. The emittance profiles for the 1Sm:0Er and 0Sm:1Er samples at all the temperatures are essentially equivalent. The only significant change in both samples occurs at the maximum emittance peak located at ~4341 nm (Points A-B).



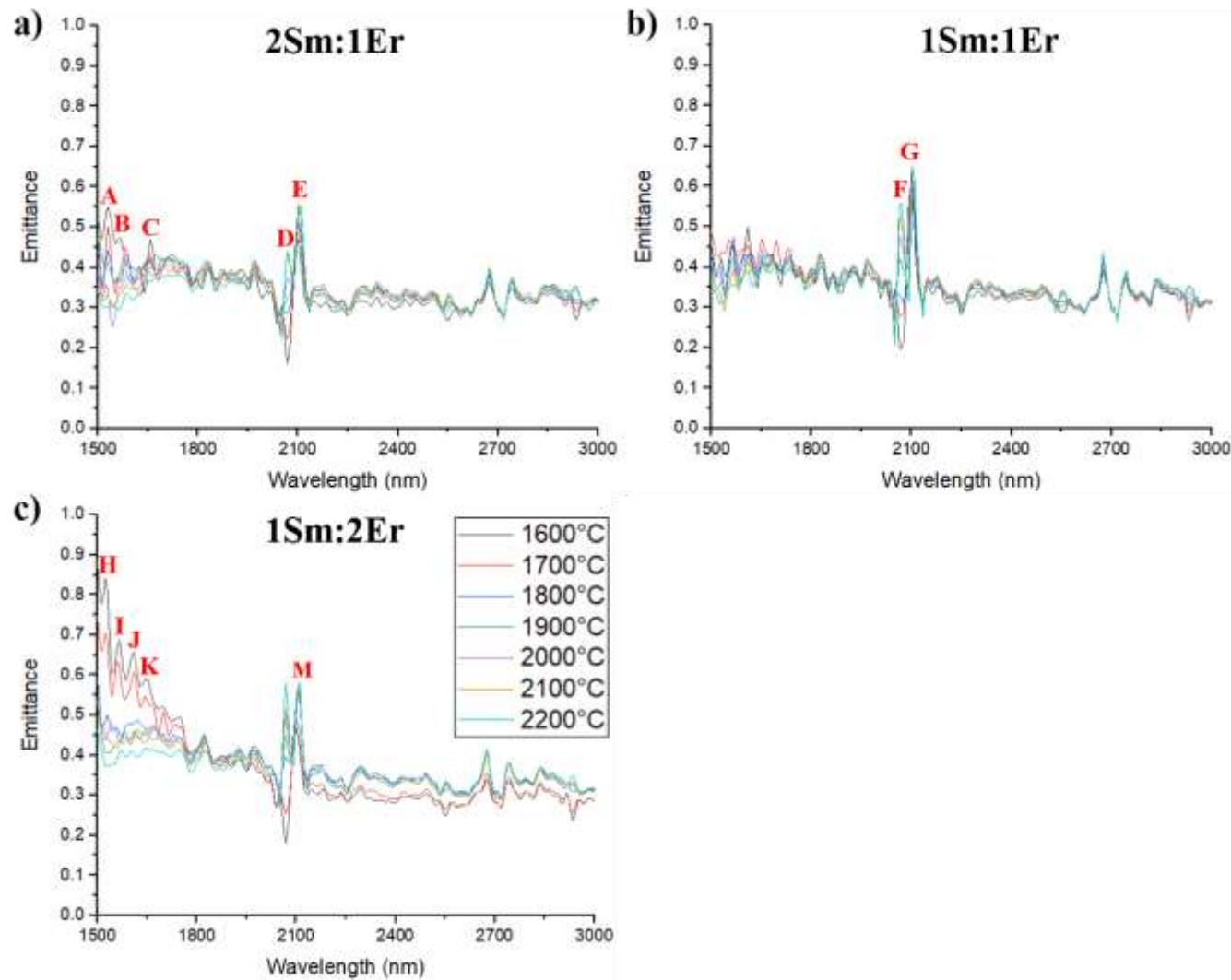


Figure 29. Emittance versus wavelength profiles at 1600 °C, 1700 °C and 1800 °C, 1900 °C, 2000 °C, and 2100 °C from 1500-3000 nm for the following billets: a) 2Sm:1Er, b) 1Sm:1Er, and c) 1Sm:2Er. This figure shows the presence of maximum emittance peaks (Points A-M) in the three samples. The emittance increases from 1500-1800 nm as the Er mol.% is increased. The emittance decreases by increasing the temperature from 1500-1800 nm, which is evident in the 1Sm:2Er sample.

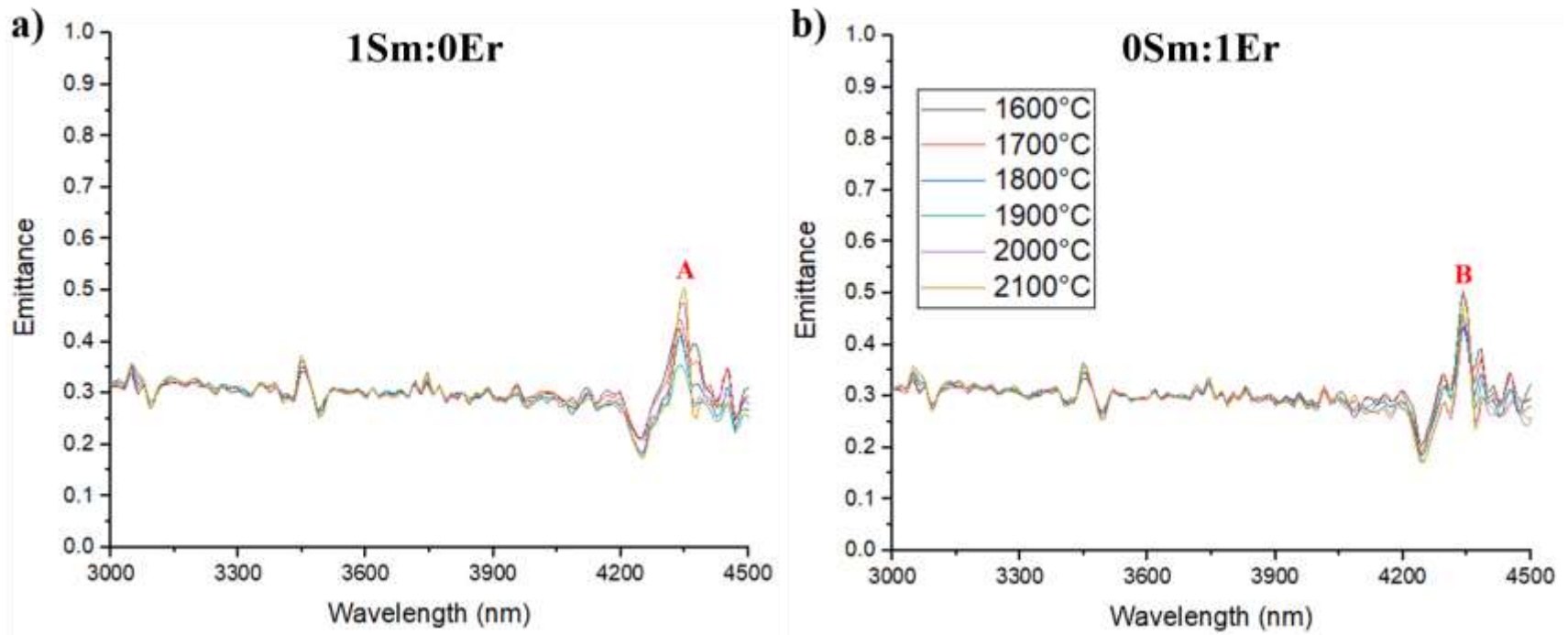


Figure 30. Emittance versus wavelength profiles at 1600 °C, 1700 °C and 1800 °C, 1900 °C, 2000 °C and 2100 °C from 3000-4500 nm for the following billets: (a) 1Sm:0Er, and (b) 0Sm:1Er. This figure shows that the emittance profiles are very similar for both samples and remain constant by increasing the temperature. The only significant change occurs at the maximum emittance peak located at 4341 nm (Points A-B).

Figures 31a-c show the emittance versus wavelength profiles from 3000-4500 nm at 1600 °C, 1700 °C, 1800 °C, 1900 °C, 2000 °C, 2100 °C and 2200 °C for the 2Sm:1Er, 1Sm:1Er, and 1Sm:2Er samples. The emittance profiles for the 2Sm:1Er, 1Sm:1Er and 1Sm:2Er samples as a function of temperature is basically the same. The only significant change on all of them occurred at the maximum emittance peak located at ~4355 nm (Points A-C) where the emittance of the 2Sm:1Er and 1Sm:2Er samples increases by increasing the temperature, whereas the emittance of the 1Sm:1Er sample decreases by increasing the temperature.

Figures 32a-e show the emittance versus laser heating time profiles as a function of wavelength for all the five different Sm:Er molar ratios during 50 s from the total 80 s of heating. The four wavelength bands used were: 1800 nm, 1900 nm, 2000 nm, and 2100 nm. For all the Sm:Er molar ratios, Figures 32a-e show that the emittance remains mainly constant as a function of laser time and temperature at the four wavelength bands measured. The emittance values slightly vary from ~0.35-0.40.

Figures 33a-g show the emittance versus wavelength profiles for all five different Sm:Er molar ratios at the following constant temperatures: 1600 °C, 1700 °C, 1800 °C, 1900 °C, 2000 °C, 2100 °C, and 2200 °C. Figures 33a-f show that the emittance values from 1500-1800 nm were the highest for the 1Sm:2Er sample. At the shorter wavelength range from 1500-1800 nm, the emittance for the 1Sm:2Er sample is the highest at 1600 °C but as the temperature is increased to 2200 °C the emittance decreases. Also, Figures 33a-g evidence that the emittance variation is more significant at shorter wavelengths (1500-1800 nm). On the contrary, as the wavelength range increase (1800-4500 nm), the emittance remains mainly constant with values between 0.30-0.40 in most of the wavelength bands. In addition, Figures 33a-g show several maximum and minimum emittance peaks can be seen for all five Sm:Er molar ratios.

The accuracy of the initial emittance assumption of 0.3 on the spectrometer-side emittance was evaluated by calculating the average emittance difference and the standard error if the emittance varies by  $\pm 0.1$  and  $\pm 0.2$  from the 0.3 value initially assumed. The average emittance difference in the spectrometer-side emittance calculated over a wavelength range from 1500-4500 nm at 1700 °C were  $0.12 \pm 0.004$  if the emittance varies by  $\pm 0.10$ , and  $0.19 \pm 0.010$  if the emittance varies by  $\pm 0.2$ . For a temperature of 1800 °C, the average emittance difference in the spectrometer-side were  $0.09 \pm 0.005$  if the emittance varies by  $\pm 0.20$ , and  $0.19 \pm 0.007$  if the emittance varies by  $\pm 0.2$ . For a temperature of 1900 °C, the average emittance difference in the spectrometer-side were  $0.10 \pm 0.003$  if the emittance varies by  $\pm 0.20$ , and  $0.21 \pm 0.007$  if the emittance varies by  $\pm 0.2$ . For a temperature of 2000 °C, the average emittance difference in the spectrometer-side were  $0.10 \pm 0.004$  if the emittance varies by  $\pm 0.10$ , and  $0.21 \pm 0.007$  if the emittance varies by  $\pm 0.20$ . The average emittance difference was calculated under their 95% confidence interval.

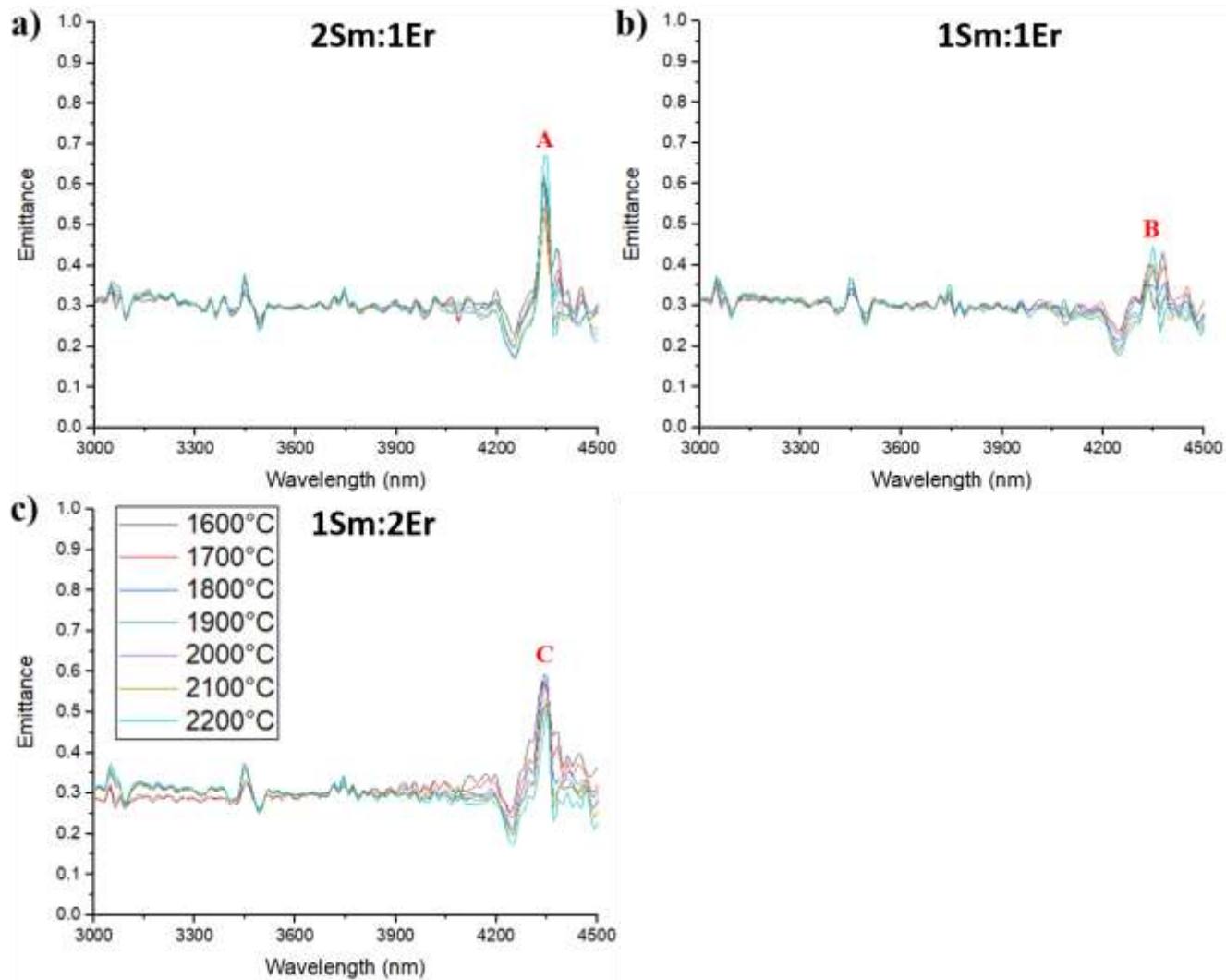


Figure 31. Emittance versus wavelength profiles at 1600 °C, 1700 °C and 1800 °C, 1900 °C, 2000 °C, 2100 °C and 2200°C from 3000-4500 nm for the following billets: a) 2Sm:1Er, b) 1Sm:1Er, and c) 1Sm:2Er. This figure shows that the emittance profiles are very similar for the three samples and remain constant by increasing the temperature. The only significant change occurs at the maximum emittance peak located at 4341 nm (Points A-C).

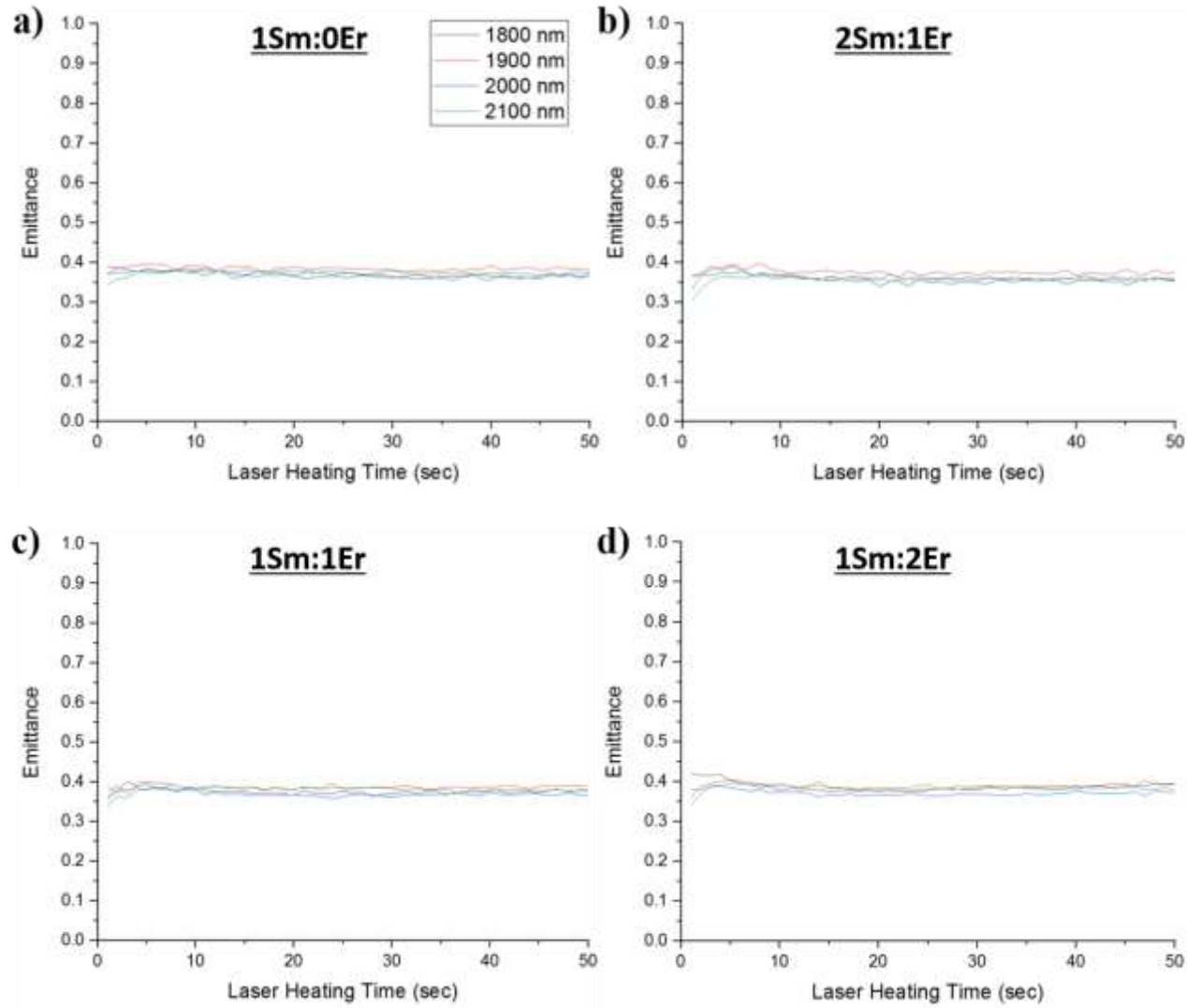
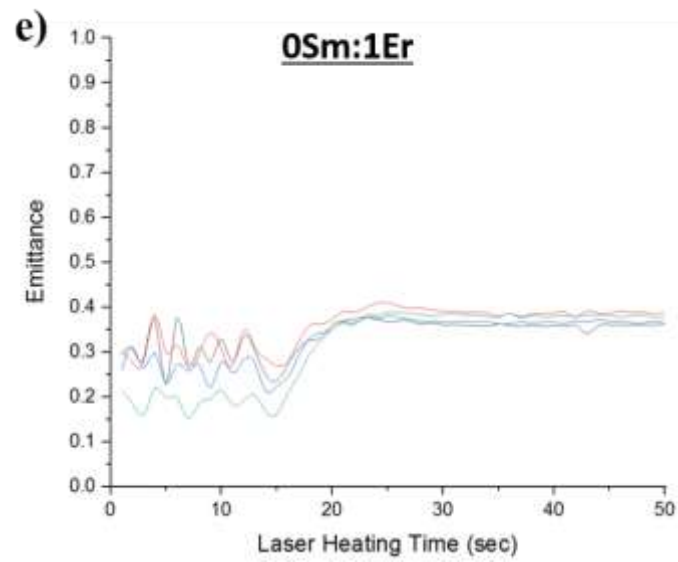


Figure 32. Emittance versus laser heating time profiles as a function of wavelength for the following billets: a) 1Sm:0Er, b) 2Sm:1Er, and c) 1Sm:1Er, d) 1Sm:2Er, and e) 0Sm:1Er. This figure shows that the emittance remains mainly constant with values between 0.30-0.40 in most of the wavelength bands.

Figure 32 continued



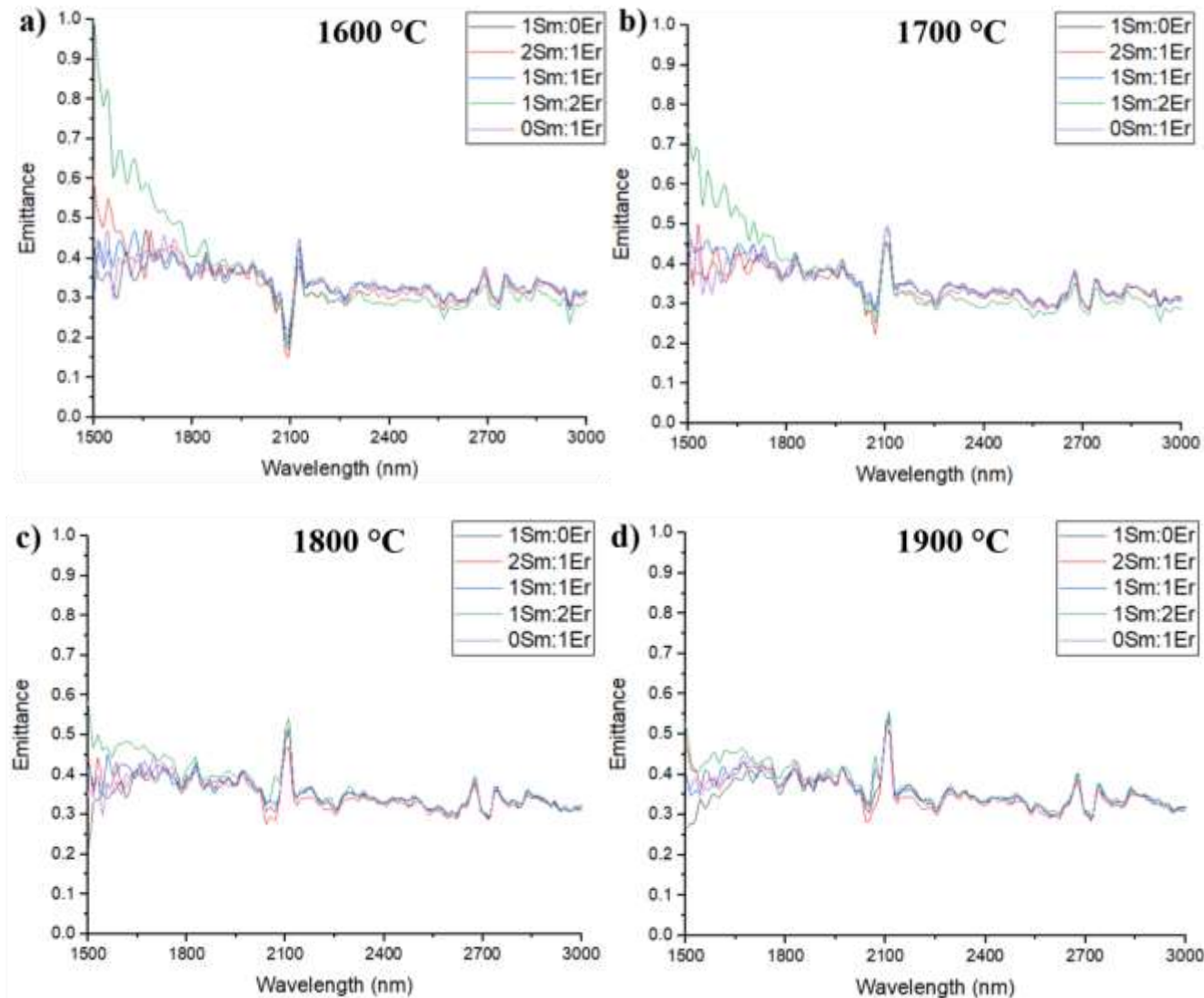
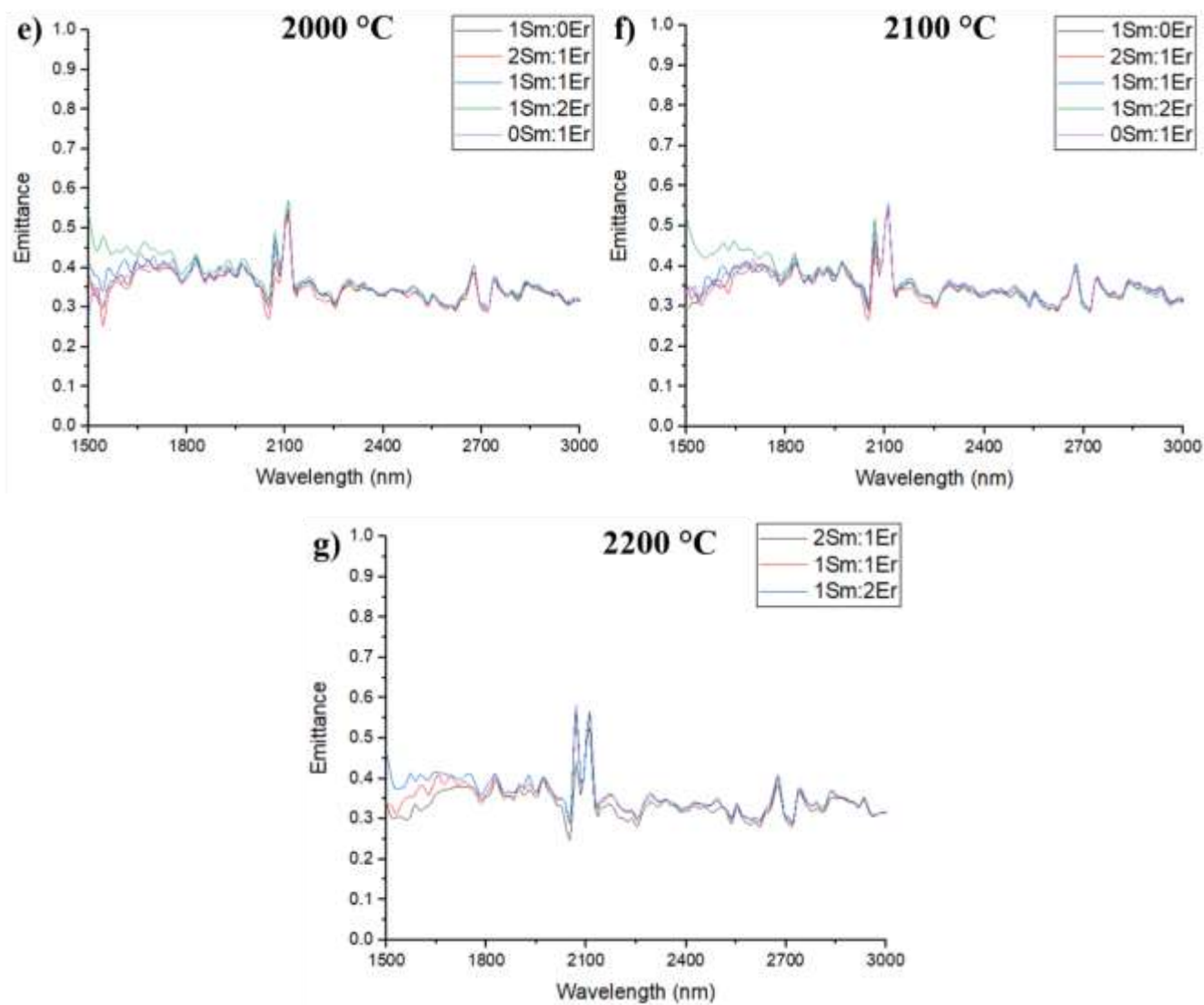


Figure 33. Emittance versus wavelength profiles as a function of dopant molar ratios at the following temperatures: (a) 1600 °C, (b) 1700 °C, (c) 1800 °C, (d) 1900 °C, (e) 2000 °C, (f) 2100 °C, and (g) 2200 °C. This figure shows that the 2Sm:1Er samples showed the highest emittance values from 1500-1800 nm (Figures 33a-f). Also, the emittance decreases by increasing the temperature.



Figure 33 continued



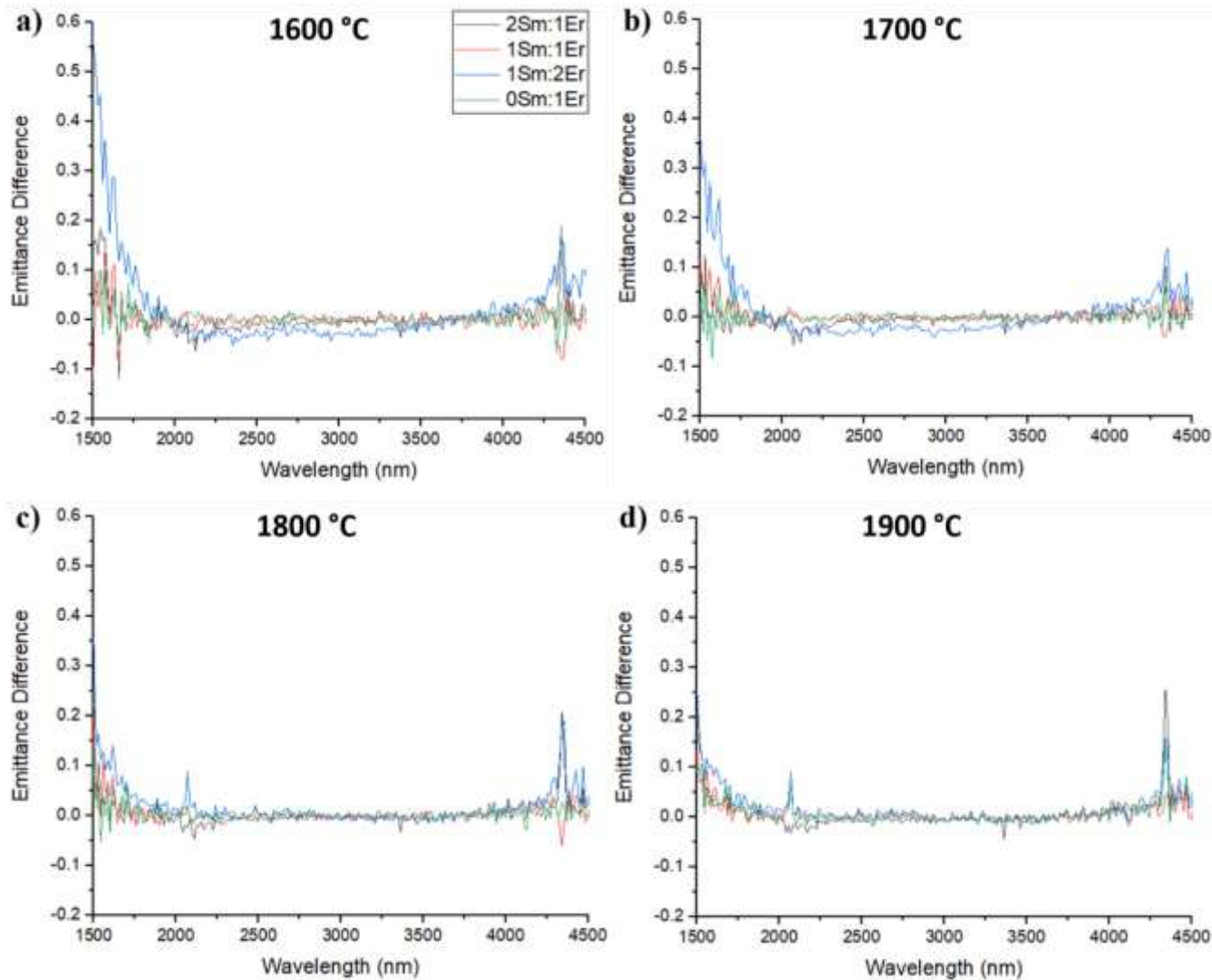
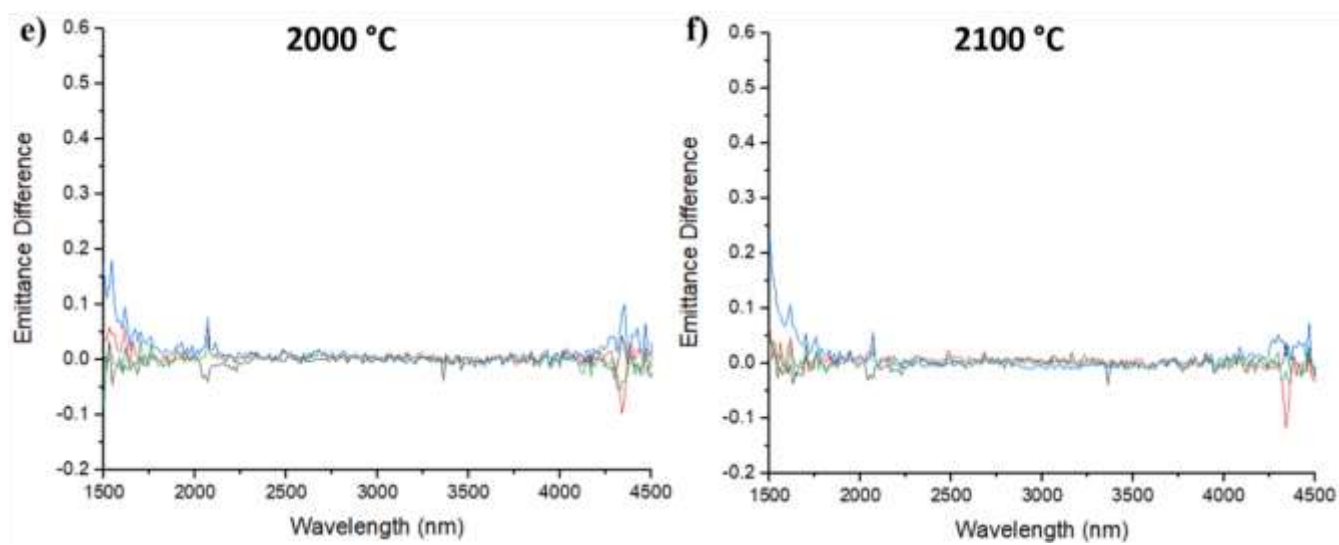


Figure 34 Emittance difference from 1500-4500 nm for the 2Sm:1Er, 1Sm:1Er, 1Sm:2Er, and 0Sm:1Er samples in comparison with the 1Sm:0Er sample. The emittance difference versus wavelength profiles as a function of dopant molar ratios is presented at the following temperatures: (a) 1600 °C, (b) 1700 °C, (c) 1800 °C, (d) 1900 °C, (e) 2000 °C, (f) 2100 °C.

Figure 34 continued



Figures 34a-f show the emittance difference from 1500-4500 nm for the 2Sm:1Er, 1Sm:1Er, 1Sm:2Er, and 0Sm:1Er samples in comparison with the 1Sm:0Er sample. In other words, how much the emittance is going to change when compared to the emittance profile of the 1Sm:0Er sample. The emittance difference data is presented at the following temperatures: 1600 °C, 1700 °C, 1800 °C, 1900 °C, 2000 °C, and 2100 °C. Again, Figures 34a-f evidence that the emittance variation is more significant at shorter wavelengths (1500-1800 nm). Also, Figures 34a-f show that the emittance difference values from 1500-1800 nm were the highest for the 1Sm:2Er sample. From 1500-1800 nm the emittance difference shows values up to ~0.55 at 1600 °C, ~0.30 at 1700 °C, ~0.20 at 1800 °C, ~0.20 at 1900 °C, 0.18 at 2000 °C, and 0.22 at 2200 °C. On the contrary, as the wavelength range increase (1800-4500 nm), the emittance difference remains mainly constant with values between  $\pm 0.05$  in most of the wavelength bands.

## **4.4 Discussion**

### **4.4.1 Factors Influencing the Emittance**

The thermally emitted spectral radiance from a surface obtained during the laser heating depends on two main aspects: (1) the surface temperature, which results from the equilibrium thermodynamic state caused by the heat transfer energy balance between the surface of the sample and its environment; and (2) the emittance, which depends on the material composition, temperature, wavelength, surface roughness, and sample thickness. The present analysis will be focused on the emittance.

The surfaces of all the samples were prepared the same way to minimize the surface effects as can be noted by the surface roughness value which was held constant at ~100 nm. In addition, the thickness of all the samples in the present study were maintained constant at ~2 mm to minimize its effect on the emittance. Furthermore, the thickness of ~2 mm is higher than the critical

thickness where the emittance starts to behave mainly constant with further increases in thickness.<sup>31,47</sup> As a result, all the changes in emittance can be related to the following factors: (1) Sm and Er dopant concentration effect, and (2) temperature and wavelength effect.

#### 4.4.2 Sm and Er Dopant Concentration Effect on the Emittance of ZBS Systems

The first factor affecting the emittance is the material composition. As the main oxide scale formed after the laser heating was *m*-ZrO<sub>2</sub>, the factors affecting its emittance values should be analyzed. Avdoshenko *et al.*<sup>31</sup> studied the high-temperature emittance of *m*-ZrO<sub>2</sub> by using density functional theory simulations to compare the emittance behavior under two different conditions: defect-free, and oxygen vacancies.<sup>31</sup> The results from systems with oxygen vacancies showed that for a thickness of 100  $\mu\text{m}$  at 1727 °C, oxygen vacancies contribute significantly to the high emittance of *m*-ZrO<sub>2</sub> by increasing its value from 0.63 for a defect-free system to 0.78 for a system with oxygen vacancies. The defects introduced in ZrO<sub>2</sub> cause a mid-gap state with the donor essence, which enables an excitation that influences significantly the emittance spectra and increases its value to 0.78 at 1727 °C.<sup>31</sup> However, this study by Avdoshenko *et al.*<sup>31</sup> was performed at a wavelength range from 200-1000 nm, which is lower than the wavelength range studies in the present study (1500-4500 nm). The emittance profiles from 1500-4500 nm obtained for the five different Sm:Er molar ratios from 1600-2200 °C, varies from 0.25-0.50 in the majority of the wavelength range with the exception of some minimum and maximum emittance peaks. These emittance values from 0.30-0.50 makes sense with the theoretical emittance values from 1500-4500 nm of ~0.3 at 1360 °C calculated by Eldridge *et al.*<sup>48</sup> The variance was likely caused by the addition of Sm and Er atoms and the higher temperatures achieved in the present study.

Previous studies have demonstrated that the emittance of ZrO<sub>2</sub> can be increased via doping with rare-earths oxides, which intentionally introduce defects into a pure material.<sup>3,9,31,49</sup> As the

dopant concentration is increased, the absorption raises in the wavelength range studied in this paper (1500-4500 nm).<sup>47</sup> Although the total RE incorporated in the samples of the present study is constant at ~3 mol%, the actual Sm incorporated varies within 0-2.94 mol%, whereas the actual Er incorporated varies within 0-3.11 mol%. As both  $\text{Sm}^{3+}$  and  $\text{Er}^{3+}$  have a different electronic structure ( $[\text{Xe}] 4f^6 6s^2$  for Sm and  $[\text{Xe}] 4f^{12} 6s^2$  for Er), the absorption spectra depend on the actual amount of each RE ion being incorporated. Based on that, it is worth to analyze the effect of dopant concentration  $\text{Sm}^{3+}$  or  $\text{Er}^{3+}$  on the electronic structure of  $\text{ZrO}_2$ .

For  $\text{Sm}_2\text{O}_3$ , the increase in emittance is produced by localized additional electronic states within the material band gap, which are caused by point defects such as oxygen vacancies, which create localized *f*-electron states.<sup>31,50</sup> These localized electronic states lead to added transitions that increase the overall dielectric response, and therefore, can modify the emittance.<sup>31</sup> As the Er atoms are very similar in size compared to the Sm atoms (242 pm for Sm and 236 pm for Er),  $\text{Er}_2\text{O}_3$  should also produce these localized electronic states by causing oxygen vacancies and localized *f*-electron states. It can be seen in the XRD plots of the post laser-heated samples in Figure 24, where a small amount of the beneficial  $c_I\text{-(Sm/Er)}_{0.2}\text{Zr}_{0.8}\text{O}_{1.9}$  was formed due to the Sm and Er atoms exchanging positions. Despite these apparent similarities, the difference in the number of *f*-shell electrons on their electronic structure ( $4f^6$  for Sm and  $4f^{12}$  for Er) should cause differences in the emittance.<sup>9,32</sup>

Unfortunately, the beneficial  $c_I\text{-(Sm/Er)}_{0.2}\text{Zr}_{0.8}\text{O}_{1.9}$  formed in previous studies<sup>9,23</sup> was not the major oxide phase formed in the front surface (spectrometer side) of the 1Sm:0Er, 2Sm:1Er, 1Sm:1Er and 1Sm:2Er samples. Therefore, the effect of producing these localized additional electronic states within the material band gap are not evident in the emittance profiles of the present study. It is speculated that the test assembly and the lack of partial oxygen pressure compared with

past studies<sup>9,23</sup> affected the XRD results. Because the samples were heated on the back side (laser side), the latter reached higher temperatures than the spectrometer side, and therefore, the majority of the Sm and Er atoms were diffused to the back side of the sample due to a flow of glass by a convection cell mechanism.<sup>23,24,25,27,34,51</sup> As a result of the minimal amount of Sm and Er atoms available in the spectrometer side, just a minimal amount of the beneficial  $c1-(\text{Sm/Er})_{0.2}\text{Zr}_{0.8}\text{O}_{1.9}$  was able to form on the spectrometer side. It represents a huge difference as the emittance profiles of  $m\text{-ZrO}_2$  and  $c1-(\text{Sm/Er})_{0.2}\text{Zr}_{0.8}\text{O}_{1.9}$  are totally different, which can be noticed by the difference in the theoretical emittance values from 1500-4500 nm of:  $\sim 0.30$  for  $m\text{-ZrO}_2$  at 1550 °C,  $\sim 0.70$ - $0.75$  for  $\text{Sm}_2\text{O}_3$  at 1550 °C, and  $0.23$ - $0.28$  for  $\text{Er}_2\text{O}_3$  at 1600 °C.<sup>13</sup> In the case of  $\text{Er}_2\text{O}_3$ , theoretical data shows that the emittance increase from  $0.18$  at  $1500$  nm to  $0.25$  at  $4500$  nm ( $1470$  °C), and from  $0.23$  at  $1500$  nm to  $0.28$  at  $4500$  nm ( $1600$  °C).<sup>13</sup> Therefore, it is worth to analyze the electronic changes induced by the oxygen vacancies to understand these differences.

As can be noted in Figures 28-33, the emittance values in most of the wavelength range for the present study are closer to the theoretical values of  $m\text{-ZrO}_2$  and  $\text{Er}_2\text{O}_3$  than  $\text{Sm}_2\text{O}_3$ . A possible way to solve this issue for sintered billets and form the  $c1-(\text{Sm/Er})_{0.2}\text{Zr}_{0.8}\text{O}_{1.9}$  could be to increase the total amount of rare-earth incorporated from 3 mol.% to 5 mol.%. Consequently, by forming the  $c1-(\text{Sm/Er})_{0.2}\text{Zr}_{0.8}\text{O}_{1.9}$  oxide phase there is an opportunity to tailor the emittance for hypersonic applications.

Finally, in the case of amorphous silica, it is known that it has a low emittance at high temperatures and the existence of point defects does not increase its value significantly.<sup>31</sup> Therefore, it is speculated that the minimum amount of the amorphous silica that was observed in the XRD results of Figure 24, slightly decrease the emittance values observed in Figures 28-33.

#### 4.4.3 Temperature and Wavelength Effect on the Emittance of ZBS Systems

As mentioned in the previous section, an increase of the RE ions concentration of either  $\text{Sm}^{3+}$  and  $\text{Er}^{3+}$  raises the number of free electrons, and therefore, more electrons are available to absorb more radiation by moving from a low to an empty high energy level.<sup>47</sup> It is well known from Kirchhoff's law that, in equilibrium, the amount of electromagnetic energy absorbed by a body at a specific wavelength is emitted at the same wavelength. Therefore, the emittance is high for wavelengths around the absorption range. However, the amount of electromagnetic energy being absorbed will directly depend on two factors: (1) the wavelength band and (2) the temperature.

The first factor affecting the emittance values of UTHC is the wavelength range being analyzed. Avdoshenko *et al.*<sup>31</sup> study shows that from a wavelength range of 200-100 nm at 1727 °C, the emittance value for *m*-ZrO<sub>2</sub> is ~0.78. Also, Wilson *et al.*<sup>52</sup> study shows that from a wavelength range of 420-740 nm the emittance values for *m*-ZrO<sub>2</sub> varies from 0.90-0.93. However, as the wavelength range is further increased to 1500-4500 nm, Eldridge *et al.*<sup>48</sup> shows that the emittance is decreased to ~0.3 at 1360 °C. For the present study, the emittance profiles from 1500-4500 nm obtained for the five different Sm:Er molar ratios from 1600-2200 °C (Figures 28-33), varies from 0.25-0.50 in the majority of the wavelength range with the exception of some minimum and maximum emittance peaks. These emittance values from 0.30-0.50 makes sense with the theoretical emittance value of ~0.3 at 1360 °C calculated by Eldridge *et al.*<sup>48</sup> The small variance between Eldridge *et al.*<sup>48</sup> and the present study was likely caused by the addition of Sm and Er atoms and the higher temperatures achieved in the present study. Based on these results, it can be seen that at the wavelength range from 200-1000 nm studied in previous studies<sup>32,52</sup>, the emittance of *m*-ZrO<sub>2</sub> reach very high values varying from 0.73-0.93 depending on the temperature, whereas as the wavelength range is further increased to 1500-4500 nm the emittance values decrease to



values fluctuating from 0.30-0.50 as shown in the present study. This difference in emittance by varying the wavelength range is caused because at wavelength bands smaller than 1000 nm the electron magnetic energy being absorbed is very high, whereas at wavelength ranges from 1500-4500 nm the electron magnetic energy being absorbed decreases causing the lower emittance values.

The second factor affecting the emittance values of UTHC is the temperature. An increase in temperature increases the thermal movement of atoms in the lattice. The thermal movement of atoms influences the electronic and optical response of the  $\text{Sm}_2\text{O}_3$  and  $\text{Er}_2\text{O}_3$  oxides.<sup>31</sup> Therefore, it is expected that an increase in temperature will affect the emittance of the  $m\text{-ZrO}_2$  and the  $c1\text{-(Sm/Er)}_{0.2}\text{Zr}_{0.8}\text{O}_{1.9}$  formed during the laser heating test, as shown by the XRD results on Figure 24. Also, Figures 28-33 show that the effect on emittance by increasing the temperature is directly related to the wavelength.

Figures 29a-c shows that at shorter wavelength ranges (1500-1800 nm), the emittance increases at lower temperatures as the Er concentration is increased from 1.23 mol.% in the 2Sm:1Er sample to 2.33 mol.% in the 1Sm:2Er sample. The increase in emittance variation at shorter wavelengths ranges from 1500-1800 nm can be explained by the Wien's displacement law which shows that the maximum spectral emissive power is displaced to shorter wavelengths with increasing temperature.<sup>10,37</sup> Hence, it is expected that the emittance versus wavelength profile will be more sensitive at shorter wavelengths. Based on the results shown in Figures 29a-c, it is evident that the Er concentration is having a bigger effect on the ZBS sintered billets than the Sm concentration. This is also confirmed by the XRD results shown in Figure 24, whereas the Er concentration is increased the amount of the  $c1\text{-(Sm/Er)}_{0.2}\text{Zr}_{0.8}\text{O}_{1.9}$  phase also increases until it reaches a point in which this phase becomes the major oxide scale as in the 0Sm:1Er sample.

Figures 28-33 show that several maximum and minimum emittance peaks are obtained because of doping the ZBS billets with rare-earth oxides. The three maximum emittance peaks were at ~2069 nm, ~2112 nm and ~4355 nm, whereas the minimum emittance peaks were at ~2055 nm, 3361 nm and 4313 nm. By looking at both  $\text{Sm}_2\text{O}_3$  and  $\text{Er}_2\text{O}_3$  emittance profiles, it is speculated that the maximum and minimum emittance peaks were caused by the  $\text{Er}_2\text{O}_3$ , as its maximum and minimum emittance peaks are similar to the ones observed in Figures 28-33.

Based on the results, it is evident that the erbium oxide is modifying the emittance profile as can be seen by the maximum and minimum emittance peaks. The effect of varying the Sm:Er molar ratios, though, is not clear as the emittance profile of all samples is similar. It is speculated that if the total dopant concentration incorporated is augmented from 3 mol.% to 5 mol.%, the beneficial  $\text{c}_1\text{-(Sm/Er)}_{0.2}\text{Zr}_{0.9}\text{O}_{1.8}$  could be formed, producing a large difference.

#### 4.5 Conclusions

The emittance of sintered billets with five different Sm:Er molar ratios were evaluated for temperature ranges from 1600 °C to 2200 °C. The maximum emittance peaks for all the Sm:Er molar ratios were 2069 nm, 2112 nm, and 2680 nm, whereas the minimum emittance peaks were 2055 nm and 3091 nm. XRD results show that *m*- $\text{ZrO}_2$  was the major phase with minor portions of  $\text{c}_1\text{-(Sm/Er)}_{0.2}\text{Zr}_{0.9}\text{O}_{1.8}$ . Emittance profiles for both 1Sm:0Er and 0Sm:1Er samples were very similar in 1500-3000 nm. Emittance increases from 1500-1800 nm by increasing the Er mol.% in the samples containing both Sm and Er. The theoretical emittance peak for  $\text{Er}_2\text{O}_3$  at ~1.5  $\mu\text{m}$  could be causing the  $\epsilon$  to be higher as the Er mol.% increases. Emittance profiles remain constant by increasing the temperature from 3000-4500 nm for all the Sm:Er ratios. Based on the results, it is evident that the erbium oxide is influencing the emittance profile, as can be noted by the maximum and minimum emittance peaks. However, the effect of varying the Sm:Er molar ratios is not clear

as the emittance profile of all samples is similar. It is speculated that if the total dopant concentration incorporated is increased from 3 mol.% to 5 mol.%, the beneficial c1-(Sm/Er)<sub>0.2</sub>Zr<sub>0.9</sub>O<sub>1.8</sub> could be formed, causing a big difference. This study represents the first generation of UHTC for hypersonic vehicles by doping ZBS systems with both Sm and Er elements.

## 5. BENEFICIAL CUBIC SAMARIUM/ERBIUM ZIRCONIUM OXIDE SCALE DEVELOPMENT

### 5.1 Beneficial $c1\text{-(Sm/Er)}_{0.2}\text{Zr}_{0.8}\text{O}_{1.9}$ Scale Preparation Using an Oxygen Furnace

The results obtained in the ablation study presented in chapter 3 showed that ZBS billets co-doped with Sm and Er to form a beneficial  $c1\text{-(Sm/Er)}_{0.2}\text{Zr}_{0.8}\text{O}_{1.9}$  oxide scale as the major phase. This oxide phase is desirable due to its ability to increase the overall emittance of the ZBS billets co-doped with Sm and Er, while maintaining excellent ablation properties up to temperatures above 2200 °C. However, the results presented in chapter 4 showed that the beneficial  $c1\text{-(Sm/Er)}_{0.2}\text{Zr}_{0.8}\text{O}_{1.9}$  phase was not formed during the emittance testing. The low partial oxygen pressure and the test assembly where the samples were heated on the back-side inhibited the  $c1\text{-(Sm/Er)}_{0.2}\text{Zr}_{0.8}\text{O}_{1.9}$  phase to be formed. As both the partial oxygen pressure and the test assembly are to conditions that cannot be modified during the emittance testing at the Air Force Research Lab facilities, it is worth to find a solution to being able to measure the emittance profile of the beneficial  $c1\text{-(Sm/Er)}_{0.2}\text{Zr}_{0.8}\text{O}_{1.9}$  phase.

Based on that problem, the overall purpose of this study is to form the beneficial  $c1\text{-(Sm/Er)}_{0.2}\text{Zr}_{0.8}\text{O}_{1.9}$  oxide scale directly from the manufacturing process instead of forming the oxide phase by exposing the samples to the oxyacetylene torch or during the laser heating testing. To achieve this, the samples were prepared using an oxygen furnace up to 1600 °C instead of the sintering process to 2000 °C in vacuum used for the studies presented in chapters 3 and 4. The XRD results shown in Figure 34 demonstrate that the beneficial  $c1\text{-(Sm/Er)}_{0.2}\text{Zr}_{0.8}\text{O}_{1.9}$  oxide scale was successfully formed by preparing the samples using the oxygen furnace.

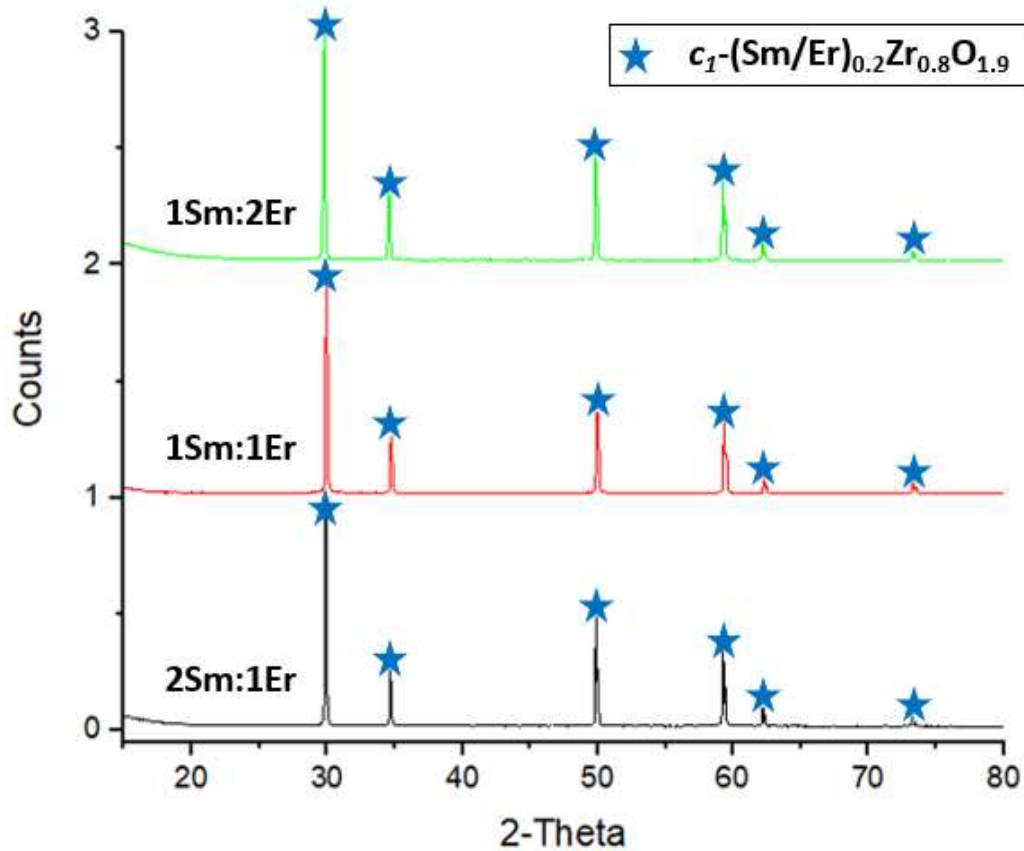


Figure 35. XRD patterns of the surface after the preparation in the oxygen furnace for the 2Sm:1Er, 1Sm:1Er, and 1Sm:2Er samples. This figure shows that the beneficial  $c_1-(\text{Sm/Er})_{0.2}\text{Zr}_{0.8}\text{O}_{1.9}$  oxide scale was formed directly from the oxygen oven.

Figure 35 shows the optical images of the surface after the preparation in the oxygen furnace for the 2Sm:1Er, 1Sm:1Er, and 1Sm:2Er samples. On the other hand, Figure 36 shows the SEM micrographs of the surface after the preparation in the oxygen furnace for the 2Sm:1Er, 1Sm:1Er, and 1Sm:2Er samples.



Figure 36. Optical images of the surface after the preparation in the oxygen furnace for the 2Sm:1Er, 1Sm:1Er, and 1Sm:2Er samples.

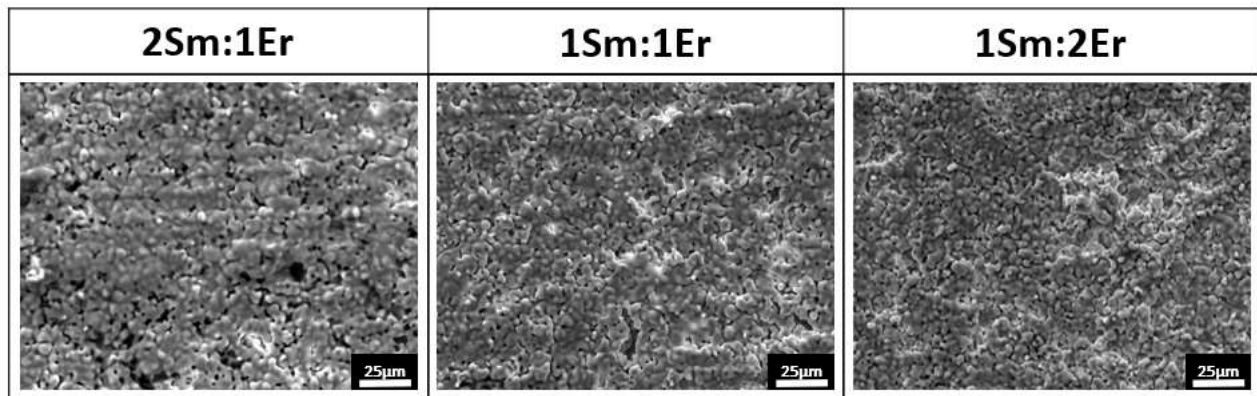


Figure 37. SEM micrographs of the surface after the preparation in the oxygen furnace for the 2Sm:1Er, 1Sm:1Er, and 1Sm:2Er samples. The three Sm:Er molar ratios showed a similar microstructure.

Future work should be focused on producing the beneficial  $c1-(\text{Sm/Er})_{0.2}\text{Zr}_{0.9}\text{O}_{1.8}$  phase directly from the manufacturing process, and therefore, maximize the effect of varying the Sm:Er molar ratios to tailor the emittance. Nonetheless, this study represents the first generation and reported emittance data of UHTC doping ZBS systems with both Sm and Er elements.

## APPENDIX A: POWDER CALCULATIONS FOR CHEMICAL DOPANT CONCENTRATION

The following calculations were made to calculate the mass quantity of dopants needed for both Sm and Er dopant concentrations for each of the five Sm:Er molar ratios. The baseline 80 vol.% ZrB<sub>2</sub> – 20 vol.% SiC spray dried powder contains:

$$2 \text{ cm}^3 \times 3.21 \text{ g/cm}^3 = 6.42 \text{ g SiC}$$

$$8 \text{ cm}^3 \times 6.09 \text{ g/cm}^3 = 48.68 \text{ g ZrB}_2$$

$$6.42 \text{ g} \times 1 \text{ mol}/40.1 \text{ g} = 0.16 \text{ mol SiC}$$

$$48.68 \text{ g} \times 1 \text{ mol}/112.8 \text{ g} = 0.43 \text{ mol ZrB}_2$$

Material	Vol. %	Density, g/cm <sup>3</sup>	Mass, g	Moles
SiC	20	3.21	6.42	0.16
ZrB <sub>2</sub>	80	6.09	48.68	0.43

### For the 1Sm:0Er Molar Ratio:

The baseline ZrB<sub>2</sub>/20vol.% SiC spray dried powder was doped with 10 mol.% of Sm(NO<sub>3</sub>)<sub>3</sub>·6H<sub>2</sub>O.

$$\frac{x}{x + 0.16 + 0.4313} = 0.1$$

$$x = 0.07$$

$$0.0657x \frac{1 \text{ mol Sm(NO}_3)_3 \cdot 6\text{H}_2\text{O}}{444.4 \text{ g}} = 29.2 \text{ g Sm(NO}_3)_3 \cdot 6\text{H}_2\text{O}$$

Material	Mass, g	Weight %	Moles	Mol. %
SiC	6.42	7.6	0.16	24.4
ZrB <sub>2</sub>	48.68	57.8	0.43	65.6
Sm(NO <sub>3</sub> ) <sub>3</sub> ·6H <sub>2</sub> O	29.2	34.6	0.07	10

**For the 2Sm:1Er Molar Ratio:**

The baseline ZrB<sub>2</sub>/20vol.% SiC spray dried powder was doped with 6.6 mol.% of Sm(NO<sub>3</sub>)<sub>3</sub>·6H<sub>2</sub>O.

$$\frac{x}{x + 0.16 + 0.4313} = 0.067$$

$$x = 0.04 \text{ mol Sm ion}$$

$$0.04246 x \frac{1 \text{ mol Sm(NO}_3)_3 \cdot 6\text{H}_2\text{O}}{444.4 \text{ g}} = 18.9 \text{ g Sm(NO}_3)_3 \cdot 6\text{H}_2\text{O}$$

Also, the baseline ZrB<sub>2</sub>/20vol.% SiC spray dried powder was doped with 3.3 mol.% of Er(NO<sub>3</sub>)<sub>3</sub>·6H<sub>2</sub>O.

$$\frac{x}{x + 0.16 + 0.4313} = 0.033$$

$$x = 0.02 \text{ mol Er ion}$$

$$0.02018 x \frac{1 \text{ mol Er(NO}_3)_3 \cdot 6\text{H}_2\text{O}}{461.3 \text{ g}} = 9.3 \text{ g Er(NO}_3)_3 \cdot 6\text{H}_2\text{O}$$

$$\frac{6.5 \text{ mol. \% Sm(NO}_3)_3 \cdot 6\text{H}_2\text{O}}{3.1 \text{ mol. \% Er(NO}_3)_3 \cdot 6\text{H}_2\text{O}} = \frac{2 \text{ Sm(NO}_3)_3 \cdot 6\text{H}_2\text{O}}{1 \text{ Er(NO}_3)_3 \cdot 6\text{H}_2\text{O}}$$



Material	Mass, g	Weight %	Moles	Mol. %
SiC	6.42	7.7	0.16	24.5
ZrB <sub>2</sub>	48.68	58.4	0.43	66.0
Sm(NO <sub>3</sub> ) <sub>3</sub> *6H <sub>2</sub> O	18.9	22.7	0.04	6.5
Er(NO <sub>3</sub> ) <sub>3</sub> *6H <sub>2</sub> O	9.3	11.2	0.02	3.1

**For the 1Sm:1Er Molar Ratio:**

The baseline ZrB<sub>2</sub>/20vol.% SiC spray dried powder was doped with 5.0 mol.% of Sm(NO<sub>3</sub>)<sub>3</sub>·6H<sub>2</sub>O.

$$\frac{x}{x + 0.16 + 0.4313} = 0.05$$

$$x = 0.03112 \text{ mol Sm ion}$$

$$0.03112 x \frac{1 \text{ mol Sm(NO}_3)_3 * 6\text{H}_2\text{O}}{444.4\text{g}} = 13.8 \text{ g Sm(NO}_3)_3 * 6\text{H}_2\text{O}$$

Also, the baseline ZrB<sub>2</sub>/20vol.% SiC spray dried powder was doped with 5.0 mol.% of Er(NO<sub>3</sub>)<sub>3</sub>·6H<sub>2</sub>O.

$$\frac{x}{x + 0.16 + 0.4313} = 0.05$$

$$x = 0.03 \text{ mol Er ion}$$

$$0.03112x \frac{1 \text{ mol Er(NO}_3)_3 * 6\text{H}_2\text{O}}{461.3\text{g}} = 14.4 \text{ g Er(NO}_3)_3 * 6\text{H}_2\text{O}$$

$$\frac{5.0 \text{ mol. \% Sm(NO}_3)_3 * 6\text{H}_2\text{O}}{5.0 \text{ mol. \% Er(NO}_3)_3 * 6\text{H}_2\text{O}} = \frac{1 \text{ Sm(NO}_3)_3 * 6\text{H}_2\text{O}}{1 \text{ Er(NO}_3)_3 * 6\text{H}_2\text{O}}$$

Material	Mass, g	Weight %	Moles	Mol. %
SiC	6.42	7.7	0.16	24.5
ZrB <sub>2</sub>	48.68	58.4	0.43	66.0
Sm(NO <sub>3</sub> ) <sub>3</sub> *6H <sub>2</sub> O	13.8	16.6	0.03	5.0
Er(NO <sub>3</sub> ) <sub>3</sub> *6H <sub>2</sub> O	14.4	17.3	0.03	5.0

**For the 1Sm:2Er Molar Ratio:**

The baseline ZrB<sub>2</sub>/20vol.% SiC spray dried powder was doped with 3.3 mol.% of Sm(NO<sub>3</sub>)<sub>3</sub>·6H<sub>2</sub>O.

$$\frac{x}{x + 0.16 + 0.4313} = 0.033$$

$$x = 0.0201788 \text{ mol Sm ion}$$

$$0.0201788 x \frac{1 \text{ mol Sm(NO}_3)_3 \cdot 6\text{H}_2\text{O}}{444.4\text{g}} = 9.0 \text{ g Sm(NO}_3)_3 \cdot 6\text{H}_2\text{O}$$

Also, the baseline ZrB<sub>2</sub>/20vol.% SiC spray dried powder was doped with 6.6 mol.% of Er(NO<sub>3</sub>)<sub>3</sub>·6H<sub>2</sub>O.

$$\frac{x}{x + 0.16 + 0.4313} = 0.067$$

$$x = 0.04246206 \text{ mol Er ion}$$

$$0.04246206 x \frac{1 \text{ mol Er(NO}_3)_3 \cdot 6\text{H}_2\text{O}}{461.3\text{g}} = 19.6 \text{ g Er(NO}_3)_3 \cdot 6\text{H}_2\text{O}$$

$$\frac{3.1 \text{ mol. \% Sm(NO}_3)_3 \cdot 6\text{H}_2\text{O}}{6.5 \text{ mol. \% Er(NO}_3)_3 \cdot 6\text{H}_2\text{O}} = \frac{1 \text{ Sm(NO}_3)_3 \cdot 6\text{H}_2\text{O}}{2 \text{ Er(NO}_3)_3 \cdot 6\text{H}_2\text{O}}$$

Material	Mass, g	Weight %	Moles	Mol. %
SiC	6.42	7.7	0.16	24.5
ZrB <sub>2</sub>	48.68	58.2	0.4313	66.0
Sm(NO <sub>3</sub> ) <sub>3</sub> *6H <sub>2</sub> O	9.0	10.8	0.0218	3.1
Er(NO <sub>3</sub> ) <sub>3</sub> *6H <sub>2</sub> O	19.6	23.4	0.04246	6.5

**For the 0Sm:1Er Molar Ratio:**

The baseline ZrB<sub>2</sub>/20vol.% SiC spray dried powder was doped with 10 mol.% of Er(NO<sub>3</sub>)<sub>3</sub>·6H<sub>2</sub>O.

$$\frac{x}{x + 0.16 + 0.4313} = 0.1$$

$$x = 0.07$$

$$0.0657x \frac{1 \text{ mol Er(NO}_3)_3 \cdot 6\text{H}_2\text{O}}{461.3\text{g}} = 30.3 \text{ g Er(NO}_3)_3 \cdot 6\text{H}_2\text{O}$$

Material	Mass, g	Weight %	Moles	Mol. %
SiC	6.42	7.5	0.16	24.4
ZrB <sub>2</sub>	48.68	57.0	0.43	65.6
Er(NO <sub>3</sub> ) <sub>3</sub> *6H <sub>2</sub> O	30.3	35.5	0.07	10

## APPENDIX B: MATLAB ALGORITHM TO CONVERT SPECTRAL RADIANCE TO EMITTANCE

### Part 1: MATLAB Algorithm for the Calibration Data for the Spectral Radiance

```
function [header, ccddata, acquiredata, wldata, intime, status, reldat, data]=readsdf(filename)

% Opening the file

errormessage=[];

[fid errormessage]=fopen(filename);

if ~isempty(errormessage)

disp(errormessage);

return

end

% HEADERDATA

%filename 64bytes type:char

header.firstline=strcat(fread(fid,[1, 64],'*char'));

%no 2bytes type:int

header.no=fread(fid,1,'int');

%time 4bytes type:long

header.time=fread(fid,1,'long');

%opticalblank type:float

header.opticalBlank=fread(fid,1,'float');

% CCDDATA

ccddata.totalColPixels=fread(fid,1,'ushort');

ccddata.totalRowPixels=fread(fid,1,'ushort');
```

```
ccddata.startBlankPixel=fread(fid,1,'ushort');
ccddata.totalBlankPixels=fread(fid,1,'ushort');
ccddata.startEffectivePixel=fread(fid,1,'ushort');
ccddata.totalEffectivePixels=fread(fid,1,'ushort');
ccddata.conversionBit=fread(fid,1,'ushort');
ccddata.unitType=fread(fid,1,'ushort');
ccddata.deviceNo=fread(fid,1,'ushort');
ccddata.channelNo=fread(fid,1,'ushort');
ccddata.boardType=fread(fid,1,'ushort');
ccddata.gain=fread(fid,1,'ushort');
ccddata.adress=fread(fid,1,'int');
ccddata.fft=fread(fid,1,'int');
ccddata.cal1=fread(fid,1,'float');
ccddata.cal2=fread(fid,1,'float');
ccddata.cal3=fread(fid,1,'float');
ccddata.cal4=fread(fid,1,'float');
ccddata.cal5=fread(fid,1,'float');
ccddata.rcal1=fread(fid,1,'float');
ccddata.rcal2=fread(fid,1,'float');
ccddata.rcal3=fread(fid,1,'float');
ccddata.rcal4=fread(fid,1,'float');
ccddata.rcal5=fread(fid,1,'float');
ccddata.temp=fread(fid,1,'float');
```

```
% ACQUIREDATA
```

```
acquiredata.startWavelength=fread(fid,1,'ushort');
```

```
acquiredata.endWavelength=fread(fid,1,'ushort');
```

```
acquiredata.timeAverage=fread(fid,1,'ushort');
```

```
acquiredata.binningAverage=fread(fid,1,'ushort');
```

```
acquiredata.fftMax=fread(fid,1,'int');
```

```
acquiredata.temp2=fread(fid,1,'uint');
```

```
% WLDATA
```

```
wldata.minXP=fread(fid,1,'uint');;
```

```
wldata.maxXP=fread(fid,1,'uint');
```

```
wldata.minYP=fread(fid,1,'uint');
```

```
wldata.maxYP=fread(fid,1,'uint');
```

```
wldata.minWL=fread(fid,1,'float');
```

```
wldata.maxWL=fread(fid,1,'float');
```

```
wldata.wavelengthInterval=fread(fid,1,'float');
```

```
wldata.minT=fread(fid,1,'float');
```

```
wldata.maxT=fread(fid,1,'float');
```

```
wldata.minA=fread(fid,1,'float');
```

```
wldata.maxA=fread(fid,1,'float');
```

```
wldata.minI=fread(fid,1,'float');
```

```
wldata.maxI=fread(fid,1,'float');
```

```
wldata.res=fread(fid,1,'float');
```

```
% INTTIME
```

```

intime.intTime=fread(fid,1,'double');

intime.intTimeMin=fread(fid,1,'double');

intime.intTimeMax=fread(fid,1,'double');

% STATUS

status.dataStart=fread(fid,1,'ubit1=>ushort');

status.dataOneStep=fread(fid,1,'ubit1=>ushort');

status.dataPending=fread(fid,1,'ubit1=>ushort');

status.drawStart=fread(fid,1,'ubit1=>ushort');

status.drawPending=fread(fid,1,'ubit1=>ushort');

status.darkScan=fread(fid,1,'ubit2=>ushort');

status.darkApply=fread(fid,1,'ubit1=>ushort');

status.darkOpticalBlank=fread(fid,1,'ubit1=>ushort');

status.fftApply=fread(fid,1,'ubit1=>ushort');

status.refScan=fread(fid,1,'ubit2=>ushort');

status.refApply=fread(fid,1,'ubit1=>ushort');

status.scanMode=fread(fid,1,'ubit3=>ushort');

status.graphUnit=fread(fid,1,'ubit2=>ushort');

status.scanOrFile=fread(fid,1,'ubit1=>ushort');

status.pixelOrWL=fread(fid,1,'ubit1=>ushort');

status.direction=fread(fid,1,'ubit1=>ushort');

status.irradiance=fread(fid,1,'ubit1=>ushort');

status.baseLine=fread(fid,1,'ubit1=>ushort');

status.timeLine=fread(fid,1,'ubit1=>ushort');

```

```

status.onlyFileMode=fread(fid,1,'ubit1=>ushort');

status.trigger=fread(fid,1,'ubit1=>ushort');

status.dataDisplay=fread(fid,1,'ubit1=>ushort');

status.refDisplay=fread(fid,1,'ubit1=>ushort');

status.pixelFlip=fread(fid,1,'ubit1=>ushort');

status.isDarkSubtract=fread(fid,1,'ubit1=>ushort');

status.stroonStop=fread(fid,1,'ubit1=>ushort');

status.subtractDark=fread(fid,1,'ubit1=>ushort');

% The following data is for future release of software

% status.triiggerChange=fread(fid,1,'ubit1=>ushort');

% status.triggerMode=fread(fid,1,'ubit=>ushort');

% REFDAT

datsize=ccddata.totalEffectivePixels;

refdat.darkArray=fread(fid,[1, datsize],'float');

refdat.darkOpticalBlank=fread(fid,1,'float');

refdat.refArray=fread(fid,[1, datsize],'float');

refdat.refOpticalBlank=fread(fid,1,'float');

% DATA

ii=1;

data(ii).scanParentName=strcat(fread(fid,[1, 64],'*char'));

while ~isempty(data(ii).scanParentName)

data(ii).scanChildName=strcat(fread(fid,[1, 64],'*char'));

data(ii).scanTime=strcat(fread(fid,[1, 64],'*char'));

```



```

data(ii).pixelData=fread(fid,[1, datsize],'long');
data(ii).opticalBlank=fread(fid,1,'float');
ii=ii+1;
data(ii).scanParentName=strcat(fread(fid,[1, 64],'*char'));
end
end

```

## **Part 2: MATLAB Algorithm to Convert Spectral Radiance to Emittance**

```

% This script file averages and calibrates a set of blackbody data and subsequently fits the
% Sakuma-Hattori coefficients A, B, and C (assuming a Planckian form) as functions of
% wavelength over defined temperature ranges (note, each calculation requires at least two
% temperatures to solve for B and C; values of A are assumed).

```

```
clear
```

```
clc
```

```
% Define physical constants
```

```
c2 = 14387.752; % Radiation constant (um*K)
```

```

% The gain and offset calculations are contained in p(:,1) and p(:,2), respectively, and these have
% been determined according to what calibration is required for the blackbody data to agree with
% the theoretical (Planckian) curves.

```

```
addpath('D:\2018-09-14 _Analysis\caldata');
```

```
load 'G&O.mat'
```

```
% The data contained in data1 through data6 constitute the raw measurements
```

```
% performed at any of the given temperatures
```

```

[header, ccddata, acquiredata, wldata, intime, status, refdat,
data1]=readsdf(strcat('1111p36','.sdf'));

[header, ccddata, acquiredata, wldata, intime, status, refdat,
data2]=readsdf(strcat('1207p46','.sdf'));

[header, ccddata, acquiredata, wldata, intime, status, refdat,
data3]=readsdf(strcat('1367p96','.sdf'));

[header, ccddata, acquiredata, wldata, intime, status, refdat,
data4]=readsdf(strcat('1501p49','.sdf'));

[header, ccddata, acquiredata, wldata, intime, status, refdat,
data5]=readsdf(strcat('1657p12','.sdf'));

[header, ccddata, acquiredata, wldata, intime, status, refdat,
data6]=readsdf(strcat('1803p97','.sdf'));

WL = [wldata.minWL:wldata.wavelengthInterval:wldata.maxWL]';

data_ave = zeros(size(WL,1),6);

data_cal  = zeros(size(WL,1),6);

temp = zeros(size(WL,1),6);

% The last 2 entries into data1.pixelData are empty, so they are skipped

N_meas = size(data1,2) - 2;

for i = 1:1:N_meas;

% The first 2 pixels in any pixelData array are presumed to be bad and are therefore skipped

temp(:,1) = temp(:,1) + data1 (1,i).pixelData(3:end)';

temp(:,2) = temp(:,2) + data2 (1,i).pixelData(3:end)';

temp(:,3) = temp(:,3) + data3 (1,i).pixelData(3:end)';

```

```

temp(:,4) = temp(:,4) + data4 (1,i).pixelData(3:end)';
temp(:,5) = temp(:,5) + data5 (1,i).pixelData(3:end)';
temp(:,6) = temp(:,6) + data6 (1,i).pixelData(3:end)';
end

% Calculate the average measurement by dividing the sum of the data (namely, temp(:,i)) by the
number of entries.

data_ave(:,i) = temp (:,i)/N_meas;

% After calculating the average, the data are calibrated according to the gain and offset given in
p(:,1) and p(:,2), respectively.

data_cal(:,1) = data_ave (:,1).*p(:,1) + p(:,2);
data_cal(:,2) = data_ave (:,2).*p(:,1) + p(:,2);
data_cal(:,3) = data_ave (:,3).*p(:,1) + p(:,2);
data_cal(:,4) = data_ave (:,4).*p(:,1) + p(:,2);
data_cal(:,5) = data_ave (:,5).*p(:,1) + p(:,2);
data_cal(:,6) = data_ave (:,6).*p(:,1) + p(:,2);

figure; plot(WL,data_cal(:,2:5));

title('Averaged and calibrated data');

legend('1207.46^oC','1367.96^oC','1501.49^oC','1657.12^oC');

xlabel('Wavelength (nm)'); ylabel('Radiance (W/(cm^2*sr*cm))');

% The temperatures of the calibration tests correspond to those given for each column in the data
matrices (temp, data_ave, and data_cal), and here it has been converted from deg C to Kelvin.

T = [1111.36 1207.46 1367.96 1501.49 1657.12 1803.97] + 273.15; % K

% Sakuma-Hattori relationship assuming Planckian (L as a function of A*T))

```

```

% ft = fitype( 'c/(2.7183^(14387.752/(x + b)))', 'independent', 'x', 'dependent', 'y' );

% Alternate Sakuma-Hattori relationship assuming Planckian (note the -1)
ft = fitype( 'c/((2.7183^(14387.752/(x + b)))-1)', 'independent', 'x', 'dependent', 'y' );

% Sakuma-Hattori relationship assuming Planckian (A*T as a function of L))
% ft = fitype( '-(14387.752/(log(x/c)) + b)', 'independent', 'x', 'dependent', 'y' );

% Fit model to data, using temperature ranges indicated by T (k_lo,k_hi).

% The outer loop (indexed with j) runs through the entire spectrum, and the inner loop
incorporates the temperature data from at least two sets.

k_lo = [2];

k_hi = [5];

b_init = 5.0;

b_lim = [-1e3 1e3];

c_init = 1e6;

c_lim = [0.0 1e8];

% Initialize the Sakuma-Hattori coefficients B and C

B = 1.0*ones(size(k_hi,2),size(WL,1)); % offset (um*K)

C = 1.0*ones(size(k_hi,2),size(WL,1)); % gain (unitless)

opts = fitoptions( 'Method', 'NonlinearLeastSquares' );

opts.Display = 'Off';

for j = 1:1:(size(WL,1));

for i = 1:1:size(k_hi,2);

opts.StartPoint = [b_init c_init];

opts.Lower = [b_lim(1) c_lim(1)];

```

```

opts.Upper = [b_lim(2) c_lim(2)];

% For L as a function of A*T, use the following definitions:

xData = T (k_lo(i):1:(k_hi(i)))'*(1e-3)*WL(j);

yData = data_cal (j,k_lo(i):1:(k_hi(i)))';

% For A*T as a function of L, use the following definitions:

% xData = data_cal (j,k_lo(i):1:(k_hi(i)))';

% yData = T (k_lo(i):1:(k_hi(i)))'*(1e-3)*WL(j);

[fitresult, gof] = fit( xData, yData, ft, opts );

B(i,j) = fitresult.b;

C(i,j) = fitresult.c;

end

end

% Plot C as a function of B, given that  $C = L \cdot \exp(c_2/(A \cdot T + B))$ ; this is
% useful for approximating the orders of magnitude that are appropriate for
% B and C, if the system of equations is going to be solved (given L
% (xData) and A and T (yData)

xTemp = T (4)'*(1e-3)*WL(147);

yTemp = data_cal (147,4)';

figure; semilogy([(-1e6):(100):(1e6)],yTemp*2.718.^(14387.752./(xTemp+([(-
1e6):(100):(1e6)])))))

title({'Sakuma-Hattori Coefficient Coupling:', 'B as a Function of C for A = 3.5 \mum and T =
1501.49^oC'});

xlabel('B'); ylabel('C');

```

```

axis([-5e4 1e6 10e1 10e7]);

% Plot the Sakuma-Hattori coefficients A, B, and C as functions of wavelength for each of the
four evaluated temperatures.

figure; h = plot(WL,B');

h (1).Marker = '.'; h (1).LineStyle = 'none';

title('Sakuma-Hattori Coefficients as a Function of Wavelength');

xlabel('Wavelength (nm)'); ylabel('B');

axis([2500 4500 -20 80]);

figure; h = semilogy(WL,C');

h (1).Marker = '.'; h (1).LineStyle = 'none';

title('Sakuma-Hattori Coefficients as a Function of Wavelength');

xlabel('Wavelength (nm)'); ylabel('C');

axis([2500 4500 1e4 1e7]);

figure; semilogy(WL,[abs (B)',(1e-3)*WL,C']);

legend('A','B','C');

title('Sakuma-Hattori Coefficients as a Function of Wavelength');

xlabel('Wavelength (nm)'); ylabel('A; abs(B); C');

% Plot fit with data.

f=figure( 'Name', 'fit','Color',[1, 1, 1]);

h = plot( fitresult, xData, yData );

addpath('D:\2018-09-14_Moro _SH _Analysis');

file='2018032915';

[header, ccddata, acquiredata, wldata, intime, status, refdat, data]=readsdf(strcat(file,'.sdf'));

```

```

caltdata=readtable(strcat(file,'.txt'));

% remove bad pixels

wl=wldata.minWL:wldata.wavelengthInterval:wldata.maxWL;

wl=wl(4:end)'; wl(45)=[]; wl(213)=[];   wl(186)=[]; wl(end)=[]; wl(end)=[];

WL=WL(4:end); WL(45)=[]; WL(213)=[];   WL(186)=[];

B =B(:,4:end); B(:,45)=[]; B(:,213)=[];   B(:,186)=[];

C =C(:,4:end); C(:,45)=[]; C(:,213)=[];   C(:,186)=[];

temp_data=table2array(caltdata(1:end,2:(end-2)));

wl_lo = 3500;

wl_up = 3900;

wl_lo _i = find(wl>wl_lo, 1, 'first');

wl_up _i = find(wl>wl_up, 1, 'first');

epsilon_guess = 0.5;

for i = 1:1:size(temp_data,1);

T_SH(i,:) = (epsilon_guess^(-1/4))*(1./((1e-3)*WL')).*(14387.752./(log(C./temp_data(i,:)+1)) -

B);

T_est(i) = sum (T_SH(i,wl_lo _i:wl_up _i))/(wl_up _i - wl_lo _i + 1);

epsilon_calc(i,:) = (((1./((1e-3)*WL')).*(14387.752./(log(C./temp_data(i,:)+1))

B))/T_est(i)).^(4);

end

pp=figure('Color',[1 1 1]);

h=plot(wl,temp_data(1,:));

Ymin=min(min(temp_data));

```

```

Ymax= max(max(temp_data));

ylim([Ymin Ymax]);

title('Calibrated Spectrometer Data');

xlabel('Wavelength (nm)');

ylabel('Radiance [W/(cm^2 sr)]');

writerObj=VideoWriter(file);

writerObj.FrameRate=1;

open(writerObj);

% hold on

for mm=2:size(caltdata,1)

% plot(wl,temp(mm,:));

set(h,'yData',temp_data(mm,:));

drawnow;

frame=getframe(pp);

writeVideo(writerObj,frame);

end

% hold off

close(writerObj);

figure;

plot(wl,temp_data(1:2:end,:));

title(['Calibrated Spectrometer Data: ',strcat(file,'.txt')]);

xlabel('Wavelength (nm)');

ylabel('Spectral Radiance [W/(cm^2 sr cm)]');

```



```

set(gca, 'xlim', [1450 5050]);

print('-f3', '-djpeg', strcat(file,'_rad'));

figure;

plot(wl(wl_lo _i:wl_up _i),temp_data(1:2:end,wl_lo _i:wl_up _i));

title(['Calibrated Spectrometer Data: ',strcat(file,'.txt')]);

xlabel('Wavelength (nm)');

ylabel('Temperature (K)');

set(gca, 'xlim', [wl_lo wl_up]);

print('-f3', '-djpeg', strcat(file,'_rad _window'));

figure;

plot(wl(wl_lo _i:wl_up _i),T_SH(1:2:end,wl_lo _i:wl_up _i));

title(['Calculated Temperature: ',strcat(file,'.txt')]);

xlabel('Wavelength (nm)');

ylabel('Temperature (K)');

axis([wl_lo wl_up 800 2200]);

print('-f3', '-djpeg', strcat(file,'_SH _temp'))

figure;

plot(wl(35:(end-60)),epsilon_calc(1:2:end,35:(end-60)));

title(['Calculated Emissivity: ',strcat(file,'.txt')]);

xlabel('Wavelength (nm)');

ylabel('Emittance');

% axis([wl_lo wl_up 800 2200]);

print('-f3', '-djpeg', strcat(file,'_SH _emiss'))

```

## REFERENCES

1. Squire T, Marschall J. Material property requirements for analysis and design of UHTC components in hypersonic applications. *Journal of the European Ceramic Society*. 2010;30(11):2239-2251.
2. Mack A. Aerothermodynamic behavior of a generic nose cap model including thermomechanical structural effects. *Aerospace Science and Technology*. 2007;11(5):386-395.
3. Tan W, Adducci M, Trice R. Evaluation of Rare-Earth Modified ZrB<sub>2</sub>-SiC Ablation Resistance Using an Oxyacetylene Torch. *Journal of the American Ceramic Society*. 2014;97(8):2639-2645.
4. Tan W, Petorak C, Trice R. Rare-earth modified zirconium diboride high emissivity coatings for hypersonic applications. *Journal of the European Ceramic Society*. 2014;34(1):1-11.
5. Monteverde F. The thermal stability in air of hot-pressed diboride matrix composites for uses at ultra-high temperatures. *Corrosion Science*. 2005;47(8):2020-2033.
6. Monteverde F, Savino R. Stability of ultra-high-temperature ZrB<sub>2</sub>-SiC ceramics under simulated atmospheric re-entry conditions. *Journal of the European Ceramic Society*. 2007;27(16):4797-4805.
7. Tului M, Marino G, Valente T. Plasma spray deposition of ultra-high temperature ceramics. *Surface and Coatings Technology*. 2006;201(5):2103-2108.
8. Li H, Yao X, Zhang Y, Li K, Guo L, Liu L. Effect of heat flux on ablation behaviour and mechanism of C/C-ZrB<sub>2</sub>-SiC composite under oxyacetylene torch flame. *Corrosion Science*. 2013; 74:265-270.
9. Tan W, Adducci M, Petorak C, Thompson B, Brenner A, Trice R. Effect of rare-earth dopant (Sm) concentration on total hemispherical emissivity and ablation resistance of ZrB<sub>2</sub>/SiC coatings. *Journal of the European Ceramic Society*. 2016;36(16):3833-3841.
10. Ilic O, Bermel P, Chen G, Joannopoulos J, Celanovic I, Soljačić M. Tailoring high-temperature radiation and the resurrection of the incandescent source. *Nature Nanotechnology*. 2016;11(4):320-324.

11. Lin S, Moreno J, Fleming J. Three-dimensional photonic-crystal emitter for thermal photovoltaic power generation. *Applied Physics Letters*. 2003;83(2):380-382.
12. Lenert A, Bierman D, Nam Y, Chan W, Celanović I, Soljačić M et al. A nanophotonic solar thermophotovoltaic device. *Nature Nanotechnology*. 2014;9(2):126-130.
13. Guazzoni G. High-Temperature Spectral Emittance of Oxides of Erbium, Samarium, Neodymium and Ytterbium. *Applied Spectroscopy*. 1972;26(1):60-65.
14. Li N, Hu P, Zhang X, Liu Y, Han W. Effects of oxygen partial pressure and atomic oxygen on the microstructure of oxide scale of ZrB<sub>2</sub>-SiC composites at 1500°C. *Corrosion Science*. 2013; 73:44-53.
15. Mohammadiun H, Mohammadiun M. Numerical Modeling of Charring Material Ablation with Considering Chemical-Reaction Effects, Mass Transfer and Surface Heat Transfer. *Arabian Journal for Science and Engineering*. 2012;38(9):2533-2543.
16. Miller-Oana M, Neff P, Valdez M, Powell A, Packard M, Walker L et al. Oxidation Behavior of Aerospace Materials in High Enthalpy Flows Using an Oxyacetylene Torch Facility. *Journal of the American Ceramic Society*. 2015;98(4):1300-1307.
17. Wang Y, Xiong X, Zhao X, Li G, Chen Z, Sun W. Structural evolution and ablation mechanism of a hafnium carbide coating on a C/C composite in an oxyacetylene torch environment. *Corrosion Science*. 2012; 61:156-161.
18. Neuman E, Hilmas G, Fahrenholtz W. Strength of Zirconium Diboride to 2300°C. *Journal of the American Ceramic Society*. 2012;96(1):47-50.
19. Tan W. Design of High Emissivity Coatings for Hypersonic Applications Using Plasma Spray [Ph.D.]. Purdue University; 2019.
20. Walker P. Gas reactions of carbon. *Carbon*. 1975;13(6):543.
21. Bahramian A. Effect of external heat flux on the thermal diffusivity and ablation performance of carbon fiber reinforced novolac resin composite. *Iranian Polymer Journal*. 2013;22(8):579-589.
22. Tang S, Deng J, Wang S, Liu W, Yang K. Ablation behaviors of ultra-high temperature ceramic composites. *Materials Science and Engineering: A*. 2007;465(1-2):1-7.
23. Peña A, Vernon J, Trice R. Evaluation of rare- earth element dopants (Sm and Er) on ablation resistance of ZrB<sub>2</sub>/SiC- sintered billets. *Journal of the American Ceramic Society*. 2019.

24. Brenner A, Peña A, Phuah X, Petorak C, Thompson B, Trice R. Cyclic ablation of high-emissivity Sm-doped ZrB<sub>2</sub>/SiC coatings on alumina substrates. *Journal of the European Ceramic Society*. 2018;38(4):1136-1142.
25. Karlsdottir S, Halloran J. Formation of Oxide Films on ZrB<sub>2</sub>-15 vol% SiC Composites During Oxidation: Evolution with Time and Temperature. *Journal of the American Ceramic Society*. 2009;92(6):1328-1332.
26. Zhou H, Feng Q, Kan Y, Gao L, Dong S. ZrB<sub>2</sub>-SiC Coatings Prepared by Vapor and Liquid Silicon Infiltration Methods: Microstructure and Oxidation Resistance Property. *Journal of Inorganic Materials*. 2013.
27. Karlsdottir S, Halloran J, Henderson C. Convection Patterns in Liquid Oxide Films on ZrB<sub>2</sub>-SiC Composites Oxidized at a High Temperature. *Journal of the American Ceramic Society*. 2007;90(9):2863-2867.
28. Padovano E, Badini C, Celasco E, Biamino S, Pavese M, Fino P. Oxidation behavior of ZrB<sub>2</sub>/SiC laminates: Effect of composition on microstructure and mechanical strength. *Journal of the European Ceramic Society*. 2015;35(6):1699-1714.
29. Wang J, Duan X, Yang Z, Jia D, Zhou Y. Ablation mechanism and properties of SiCf/SiBCN ceramic composites under an oxyacetylene torch environment. *Corrosion Science*. 2014; 82:101-107.
30. Bertin J, Cummings R. Fifty years of hypersonics: where we've been, where we're going. *Progress in Aerospace Sciences*. 2003;39(6-7):511-536.
31. Avdoshenko S, Strachan A. High-temperature emissivity of silica, zirconia and samaria from ab initio simulations: role of defects and disorder. *Modelling and Simulation in Materials Science and Engineering*. 2014;22(7):075004.
32. Benoit M, Ispas S, Jund P, Jullien R. Model of silica glass from combined classical and ab initio molecular-dynamics simulations. *The European Physical Journal B*. 2000;13(4):631-636.
33. Bartuli C, Valente T, Tului M. Plasma spray deposition and high temperature characterization of ZrB<sub>2</sub>-SiC protective coatings. *Surface and Coatings Technology*. 2002;155(2-3):260-273.

34. Karlsdottir S, Halloran J. Oxidation of ZrB<sub>2</sub>-SiC: Influence of SiC Content on Solid and Liquid Oxide Phase Formation. *Journal of the American Ceramic Society*. 2009;92(2):481-486.
35. Gangireddy S, Karlsdottir S, Norton S, Tucker J, Halloran J. In situ microscopy observation of liquid flow, zirconia growth, and CO bubble formation during high temperature oxidation of zirconium diboride–silicon carbide. *Journal of the European Ceramic Society*. 2010;30(11):2365-2374.
36. Opila E, Levine S, Lorincz J. Oxidation of ZrB<sub>2</sub>- and HfB<sub>2</sub>-based ultra-high temperature ceramics: Effect of Ta additions. *Journal of Materials Science*. 2004;39(19):5969-5977.
37. Hollands K. *Thermal radiation fundamentals*. New York: Begell House; 2004.
38. Saunders P, White D. Physical basis of interpolation equations for radiation thermometry. *Metrologia*. 2003;40(4):195-203.
39. Müller B, Renz U. Development of a fast fiber-optic two-color pyrometer for the temperature measurement of surfaces with varying emissivities. *Review of Scientific Instruments*. 2001;72(8):3366-3374.
40. Sani E, Mercatelli L, Sans J, Sciti D. Optical properties of black and white ZrO<sub>2</sub> for solar receiver applications. *Solar Energy Materials and Solar Cells*. 2015; 140:477-482.
41. Kumano T, Hanamura K. Control of spectral emittance using a rare-earth oxide film coated on a ceramic plate. *Heat Transfer-Asian Research*. 2010.
42. Saunders P. Propagation of uncertainty for non-linear calibration equations with an application in radiation thermometry. *Metrologia*. 2003;40(2):93-101.
43. Liang M, Sun B, Sun X, Xie J, Yu C. Rules of Emissivity Sample Choice in Multi-wavelength Pyrometry. *International Journal of Thermophysics*. 2017;38(3).
44. Hernandez D, Sans J, Netchaieff A, Ridoux P, Le Sant V. Experimental validation of a pyroreflectometric method to determine the true temperature on opaque surface without hampering reflections. *Measurement*. 2009;42(6):836-843.
45. Khan M, Allemand C, Eagar T. Noncontact temperature measurement. II. Least squares-based techniques. *Review of Scientific Instruments*. 1991;62(2):403-409.
46. Lowe D, Machin G, Sadli M. Correction of temperature errors due to the unknown effect of window transmission on ratio pyrometers using an in-situ calibration standard. *Measurement*. 2015; 68:16-21.

47. He X, Li Y, Wang L, Sun Y, Zhang S. High emissivity coatings for high temperature application: Progress and prospect. *Thin Solid Films*. 2009;517(17):5120-5129.
48. Eldridge J, Spuckler C, Markham J. Determination of Scattering and Absorption Coefficients for Plasma-Sprayed Yttria-Stabilized Zirconia Thermal Barrier Coatings at Elevated Temperatures. *Journal of the American Ceramic Society*. 2009;92(10):2276-2285.
49. Kenyon A. Recent developments in rare-earth doped materials for optoelectronics. *Progress in Quantum Electronics*. 2002;26(4-5):225-284.
50. Broer L, Gorter C, Hoogschagen J. On the intensities and the multipole character in the spectra of the rare earth ions. *Physica*. 1945;11(4):231-250.
51. Marschall J, Pejakovic D, Fahrenholtz W, Hilmas G, Panerai F, Chazot O. Temperature Jump Phenomenon During Plasmatron Testing of ZrB<sub>2</sub>-SiC Ultrahigh-Temperature Ceramics. *Journal of Thermophysics and Heat Transfer*. 2012;26(4):559-572.
52. Spitzer C, Wilson R. Spectral and integrated emittance of ablation chars and carbon. *AIAA Journal*. 1969;7(11):2140-2142.

## **VITA**

Angel Antonio Peña was born on April 25, 1991. He was raised in Morovis, Puerto Rico. He completed his high school education at the college Sagrada Familia in Corozal, Puerto Rico. Angel graduated from a bachelor's degree in Mechanical Engineering from the University of Puerto Rico at Mayaguez in May 2015. This degree was followed by a Doctor of Philosophy in Materials Science and Engineering from Purdue University in May 2019. As a graduate student, Angel received the Knox Fellowship.

## PUBLICATIONS

1. A. E. Brenner, A. A. Peña, X. L. Phuah, C. Petorak, B. Thompson, R. W. Trice, “Cyclic ablation of high-emissivity Sm-doped ZrB<sub>2</sub>/SiC coatings on alumina substrates”, Journal of the European Ceramic Society. 2018;38(4):1136–42
2. A. A. Peña, J. P. Vernon, R. W. Trice, Vernon, “Evaluation of Rare-earth Co-dopant (Sm and Er) on Ablation Resistance of ZrB<sub>2</sub>/SiC Sintered Billets”, Journal of the American Ceramic Society, (2019). \*Article in Press\*
3. A. A. Peña, J. Pitz, J. P. Vernon, R. W. Trice, “Evaluation of Rare-earth Element Dopants (Sm and Er) on the Emittance Tailoring of ZrB<sub>2</sub>/SiC Sintered Billets”, Journal of the American Ceramic Society. \*Manuscript will be submitted for revision\*